

Alma Mater Studiorum – Università di Bologna

DOTTORATO DI RICERCA IN

Ingegneria Elettronica, Telecomunicazioni e Tecnologie dell'Informazione

Ciclo XXXII

Settore Concorsuale: 09/F1 - Campi elettromagnetici

Settore Scientifico Disciplinare: ING-INF/02

COMPRESSIVE SENSING AND  
IMAGING OF GUIDED ULTRASONIC  
WAVEFIELDS

**Presentata da: Yasamin Keshmiri Esfandabadi**

**Coordinatore Dottorato**  
**Prof.ssa Alessandra Costanzo**

**Supervisore**  
**Prof. Diego Masotti**  
**Co-supervisore**  
**Prof. Luca de Marchi**

**Esame finale anno 2020**



*Dedicated to my parents and sister*

## Acknowledgements

I would like to express my gratitude to all those who gave me the possibility to complete this thesis.

First of all, I would like to thank my extraordinary advisor and mentor, Luca De Marchi, for his continuous support and encouragement, his perfectionism, clarity, great intuitions, openness to ideas, as well as his chill attitude, modesty, and superb sense of humor. I was truly blessed to have Luca as my teacher.

I would also like to show my appreciation to Professor Diego Masotti, Guido Masetti, Alessandro Marzani and Patrice Masson, thanks a lot for letting me be a member of your excellent research team. Working with you was a great honour for me and I have benefited so much from your guidance, skills and the time that you have devoted for managing my research projects. I gratefully acknowledge Maciej Radzienski, Pawel Kudela and Prof. Wieslaw M. Ostachowicz (Institute of Fluid-Flow Machinery, Polish Academy of Science) for providing numerical and experimental data used in the validation of the algorithms discussed in this Thesis.

I would like to acknowledge the opportunity provided for me by the university of Bologna to spend my internship at University of Sherbrooke.

I especially thank Prof. Alessandro Vanelli-Coralli, and Prof. Alessandra Costanzo, Ph.D. board coordinators, for their administrative support and

cooperation. I also want to thank staff and administrators of both the university of Bologna and university of Sherbrooke.

I would like to thank all my friends and colleagues who had wonderful time with me at Bologna and Sherbrooke. They made my life very happy.

I would like to thank my family. They always trusted my decisions and supported me.

## Abstract

Structural health monitoring (SHM) and Nondestructive Evaluation (NDE) technologies can be used to predict the structural remaining useful life through appropriate diagnosis and prognosis methodologies. The main goal is the detection and characterization of defects that may compromise the integrity and the operability of a structure. The use of Lamb waves, which are ultrasonic guided waves (GW), have shown potential for detecting damage in specimens as a part of SHM or NDT systems. These methods can play a significant role in monitoring and tracking the integrity of structures by estimating the presence, location, severity, and type of damage. One of the advantages of GW is their capacity to propagate over large areas with excellent sensitivity to a variety of damage types while guaranteeing a short wavelength, such that the detectability of large structural damages is guaranteed.

The Guided ultrasonic wavefield imaging (GWI) is an advanced technique for Damage localization and identification on a structure. GWI is generally referred to as the analysis of a series of images representing the time evolution of propagating waves and, possibly, their interaction with defects. This technique can provide useful insights into the structural conditions. Nowadays, high-resolution wavefield imaging has been widely studied and applied in damage identification. However, full wavefield imaging techniques have some limitations, including slow data acquisition and lack of accuracy.

The objectives of this dissertation are to develop novel and high resolution Guided Wavefield Imaging techniques able to detect defects in metals

and composite materials while reducing the acquisition time without losing in detection accuracy.

This dissertation will investigate sensing and diagnosis methodologies that provide rapid non-contact inspection of damage and diagnosis of structural health for the safety and reliability of the structure. After an introductory part and the review of the state of the art (Chapters 1-3), the dissertation presents the original contribution, whose description is organized into two major parts:

- In Part I (Chapters 4-5), Compressive Sensing (CS) reconstruction algorithms have been proposed to speed up the acquisition process. such reconstruction can be combined with Super-resolution Convolutional Neural Networks schemes to obtain high-resolution images from low-resolution wavefield images. This dissertation research proposes the combination of CS and CNNs to recover images captured with a Scanning Laser Doppler Vibrometer (SLDV), by training the CNNs with a dataset of ultrasound wave propagation images. Compressive Sensing sub-sampling procedures were used to generate a dataset of simulated low-resolution image acquisitions. The deep learning networks were then trained to recover the original high-resolution images from the low-resolution images obtained after CS sub-sampling. This technique demonstrates the capability of the technique for enhancing image resolution and quality while acquiring just 10% of the original number of scan points.
- Part II (Chapter 6) focuses on damage detection techniques applied to full wavefield data acquired with CS procedures. The aim is to realize an effective tool for damage detection and localization which allows to reduce the acquisition time. One of the developed technique exploits the compressive sensing framework to infer the damage location and the entity from the comparison between the wavefield reconstructions produced by the different representation domains such as those spanning by Wave atoms (WA), Curvelets (CT) and Fourier (FT) exponentials. This technique can be applied in a variety of structural components to reduce acquisition time and achieve high performance in defect detection and localization by

## VIII

removing up to 80% of the Nyquist sampling grid. Moreover, novel alternative methodologies to process recovered wavefield data in the wavenumber/frequency domain are presented. In particular, it is investigated a processing strategy based on the removal of the injected wave from the overall response, to highlight the presence of reflections associated with damage, and on the application of the Laplacian filter to enhance the discontinuities. The results demonstrate enhanced damage visualization, while being compatible with CS, thus reducing the original number of scan points.



# Contents

<b>1</b>	<b>Introduction</b>	<b>1</b>
1.1	Overview of Structural Health Monitoring . . . . .	1
1.2	Guided Waves based SHM . . . . .	4
1.3	Guided wavefield Imaging . . . . .	4
1.4	Motivations and objectives . . . . .	5
1.5	Contribution and Organization . . . . .	6
<b>2</b>	<b>Guided Waves Detection</b>	<b>9</b>
2.1	Fundamentals of Lamb waves . . . . .	9
2.2	Sensing and actuation of guided waves . . . . .	11
2.2.1	Piezoelectric contact transducers . . . . .	12
2.2.2	Air-coupled transducers . . . . .	12
2.2.3	Laser Doppler Vibrometry . . . . .	15
2.2.4	Other sensing methods . . . . .	17
<b>3</b>	<b>Damage imaging</b>	<b>19</b>
3.1	Damage imaging with in situ sensors . . . . .	19
3.1.1	Guided wave array imaging . . . . .	20
3.2	Damage imaging based on wavefield analysis . . . . .	24
3.2.1	Wavefield imaging basics . . . . .	24
3.2.2	Wavefield analysis and Damage Detection techniques	25
<b>4</b>	<b>Compressive Sensing of wavefields</b>	<b>35</b>
4.1	Summary . . . . .	35
4.2	Rapid and Sparse Lamb waves inspection techniques . . . .	35

4.3	Compressive Sensing theory . . . . .	39
4.4	CS Recovery results . . . . .	41
<b>5</b>	<b>CNN for Enhancing Image quality</b>	<b>47</b>
5.1	Summary . . . . .	47
5.2	High resolution Wavefield imaging . . . . .	48
5.3	Materials and methods . . . . .	50
5.3.1	Recovered Wavefield Images . . . . .	51
5.4	Single image super-resolution . . . . .	52
5.4.1	Super-resolution convolutional neural network . . . . .	52
5.4.2	Very-deep super resolution . . . . .	55
5.5	Experimental validation . . . . .	56
5.5.1	Training and testing of SRCNN and VDSR . . . . .	56
5.6	Results and discussion . . . . .	62
5.7	Discussion . . . . .	66
<b>6</b>	<b>CS and Damage Imaging</b>	<b>69</b>
6.1	Summary . . . . .	69
6.2	Materials and methods . . . . .	70
6.2.1	Cumulative kinetic Energy . . . . .	72
6.2.2	Differential CS Recovery for Damage Imaging . . . . .	75
6.2.3	Local Wavenumber estimation . . . . .	84
6.2.4	Laplacian filtering . . . . .	85
6.3	Results and discussion . . . . .	88
<b>7</b>	<b>Conclusions</b>	<b>95</b>
7.1	Conclusion . . . . .	95
7.2	Future work developments . . . . .	97

# List of Figures

1.1	Engineering applications for Structural Health Monitoring. . .	2
1.2	Guided wave testing (GWT) . . . . .	3
1.3	Illustration of incident and scattered waves. . . . .	5
2.1	Dispersion curves of a 1 mm thickness aluminum plate: (a) group velocity dispersion curves, and (b) phase velocity dispersion curves. . . . .	10
2.2	Symmetric and anti-symmetric Lamb wave modes. . . . .	11
2.3	Examples of various transducers: (a) PWAS [1]; (b) Comb transducer [2–9]; (c) MFC [8]; (d) Wedge transducers [10]; (e) FBG [11]; (f) EMAT transducer [12]. . . . .	13
2.4	Composite plate and Air-coupled transducer. . . . .	14
2.5	Scan Laser Doppler Vibrometer (SLDV) . . . . .	16
3.1	Snapshots of wavefields at 60 $\mu$ s, 81 $\mu$ s, and 110 $\mu$ s in an aluminum plate. . . . .	26
3.2	Wavefield propagation imaging plots for 75 kHz excitation: (a) in-plane X direction, (b) in-plane Y direction and (c) out-of-plane Z direction . . . . .	27
3.3	Experimental results of displacements in the z direction: (a) at 150 kHz excitation, (b) 75 kHz excitation, (c) 40 kHz excitation. . . . .	27

3.4	(a) Sketch of a setup constituted by a simple aluminum plate with a clamped mass, (b) Snapshot at $t = 98\mu s$ of the measured ultrasonic wavefield; (c) damage image generated by computing the maximum value of the wavenumber-domain filtered signal, as suggested in [13]. The white dot circle represents the actual position of the clamped mass. . . . .	28
4.1	Jittered sampling of the measurement region: the black dots represent the scan points obtained by regularly subsampling the $x_1 - x_2$ space; their position is then randomly perturbed (red circles) to define the new scan points with coordinates $x_{u1}$ and $x_{u2}$ . . . . .	42
4.2	(a) Jitter masks used to undersample the acquisitions for an area of $80\text{ mm} \times 80\text{ mm}$ of the aluminum plate test case: (a) 50%, (b) 33% and (c) 20% retained scan points. White dots are retained full grid scanpoints and black dots are those discarded. . . . .	42
4.3	Original full wave field on simple composite plate at a given time instant (a), full wave field recovered with FFT 2-D by 33% measurements with respect to the original sampling grid (b). . . . .	45
4.4	Full wave field recovered with FFT 2-D by 50% (a), 33%(b) and 20%(c) measurements with respect to the original sampling grid in the composite plate. . . . .	45
5.1	Experimental setup used to measure ultrasonic guided wavefields. . . . .	50
5.2	Overview of the SRCNN scheme for HR image reconstruction.	51
5.3	Overview of the VDSR scheme for HR image reconstruction.	52
5.4	Examples of guided ultrasonic wavefield images related to Aluminum and CFRP plates setups which were used to train the SRCNN and VDSR. Plate features and mass positions (dotted circles) have been highlighted. . . . .	53

5.5	Wavefield images recovered for the simple CFRP plate using various methodologies; (a) sketch of the setup and original wavefield image; (b) images recovered uniquely with the CS procedure for CRs:50%, 33% and 10%; (c) images recovered with the CS and SRCNN; (c) images recovered with the CS and VDSR. . . . .	57
5.6	Wavefield images recovered for the simple aluminum plate with a clamped mass using various methodologies; (a) The schematic of plate and original wavefield image; (b) images recovered uniquely with the CS procedure for CRs:50%, 33% and 10%; (c) images recovered with the CS and SRCNN; (c) images recovered with the CS and VDSR. . . . .	58
5.7	(a) HR wavefield image acquired in the simple CFRP plate; (b) CS recovery (CR= 50%); (c) recovered image achieved by combining CS and VDSR. . . . .	59
5.8	(a) HR wavefield image acquired in the simple aluminum plate with a clamped mass; (b) CS recovery (CR= 33%); (c) recovered image achieved by combining CS and VDSR. . . . .	59
5.9	Comparison of the SSIM between the training models with WI and NWI datasets and the CS technique for an aluminum plate with CR=10%, 33% and 50%. . . . .	63
5.10	Comparison of the SSIM between the training models with WI and NWI datasets and the CS technique for a CFRP plate with CR=10%, 33% and 50%. . . . .	63
5.11	Training of SRCNN with the wavefield images (WI) dataset for a curved CFRP plate. . . . .	64
5.12	Comparison of the SSIM between the CS, the SRCNN scheme, and the VDSR scheme for all the considered cases in the testing dataset with CR=10%, 33% and 50%. In the boxplot representation, the central mark indicates the median, and the bottom and top edges of the box indicate the 25th and 75th percentiles, respectively. The whiskers extend to the most extreme data points. . . . .	65

5.13	Comparison of the PSNR between the CS, the SRCNN scheme, and the VDSR scheme for all the considered cases in the testing dataset with CR=10%, 33% and 50%. In the boxplot representation, the central mark indicates the median, and the bottom and top edges of the box indicate the 25th and 75th percentiles, respectively. The whiskers extend to the most extreme data points. . . . .	65
6.1	Sketch of the experimental setup using air probe and CNC machine. . . . .	73
6.2	Sketch of the three (numerical and SLDV) setups (a, b, c), the dashed lines are the perimeters of the imaged areas. Snapshots of the full measured wavefield at $t = 66 \mu s$ , $t = 53 \mu s$ and $t = 89 \mu s$ for the aluminum plate with numerical data, GFRP and CFRP plates with experimental data, (d, e, and f), respectively. . . . .	74
6.3	CKED computed on the full wavefield signals acquired on the aluminum (a), GFRP (b) and CFRP (c) plates, respectively. The considered time interval is equal to $512 \mu s$ for the aluminum, $512 \mu s$ for the GFRP plate, and $1024 \mu s$ for the CFRP plate. The time window was selected in order to capture the most energetic portion of the wavefield after actuation. After a certain time, due to dissipation, the energy drops to a negligible level and the wavefield samples can be discarded. . . . .	75
6.4	Wavefield imaging performances in terms of CNR for the aluminum plate for 50% of downsamples. . . . .	79
6.5	CKED damage influence maps based on the simulated wavefield signals (aluminum plate). The results related to different reconstruction bases and different subsampling factors with 90 iterations are presented. on the figures of 2DFT-2DCT and 2DCT-2DWA, artifacts might be caused by a recovery error in the CS procedure. . . . .	80

6.6	CKED damage influence maps based on the wavefield signals acquired with the SLDV on the GFRP plate. The results related to different reconstruction bases and different sub-sampling factors with 90 iterations are presented. . . . .	81
6.7	CKED damage influence maps based on the wavefield signals acquired with the SLDV on the CFRP plate. The results related to different reconstruction bases and different sub-sampling factors with 90 iterations are presented. . . . .	82
6.8	Damage map related to an area which includes edge reflections: GFRP plate (B1= FFT2D, B2=FFT3D, 50% down-sampling). . . . .	84
6.9	Diagram of local wavenumber estimation process. . . . .	85
6.10	Snapshots of the reconstructed wavefields at different times and mass positions (a,b,c), and results of the Laplacian Filtering procedures (d,e and f). The damage images peak in correspondence to the actual mass positions. . . . .	87
6.11	Snapshot of the wavefield acquired in the aluminum plate with air-coupled probe (a), CKED of the signal (b), CKED of the signal after wavenumber-filtering (c), damage map after Laplacian filtering (d) with CR=33% (top row) and CR=10% (bottom row). . . . .	88
6.12	Sketch of the three setups (a, b, c), the dashed lines are the perimeters of the imaged areas. Snapshots of the measured wavefield at $t = 78\mu s$ , $t = 82\mu s$ and $t = 93\mu s$ for the Epoxy glass, CFRP and Honeycomb plates, (d, e, and f), respectively.	90
6.13	The three plates investigated with air couple probes: Epoxy glass, CFRP and Honeycomb plates, respectively. . . . .	90
6.14	Frequency-wavenumber map with the propagation direction for the Epoxy glass (a), Composite (b) and Honeycomb (c) plates. . . . .	91
6.15	CKED (a), Differential CS with 50% of subsamples and 30 iterations by using FFT2D (b), LW (c), Laplacian filter(d) on the epoxy glass. . . . .	92

6.16	CKED (a), Differential CS with 50% of subsamples and 30 iterations by using FFT2D (b), LW (c), Laplacian filter (d) on the CFRP plate. . . . .	92
6.17	CKED (a), Differential CS with 50% of subsamples and 30 iterations by using FFT2D (b), LW (c), Laplacian filter (d) on the aluminum plate. . . . .	92
6.18	SNR performances achieved with the 30 number of iterations of the SPGL1 algorithm for 20%, 33% and 50% of the downsamples for the epoxy glass. . . . .	93
7.1	Comparison of the recovery of a 10% down-sampled image with VDSR, DCSCN and PR. The three deep learning architectures produce very similar results. . . . .	97
7.2	Illustration of pixel recursive super resolution model trained end-to-end on a dataset of wavefield images. The left column shows original wavefield images. The middle and last columns show $8\times 8$ low resolution inputs from the test set and $32\times 32$ high resolution images. . . . .	98



# List of Tables

4.1	Computational time (in minutes) of the CS recovery in case of CR=50% for the aluminum plate. . . . .	44
5.1	Geometrical features of the aluminum (AL) and carbon fiber reinforced polymer (CFRP) structures . . . . .	54
5.2	The results of PSNR using CS and NN methods trained by Non Wavefield Images (NWI) and Wavefield Images (WI), and the results of PSNR using bicubic method trained by Wavefield Images (WI). . . . .	61
5.3	The properties of the unidirectional lamina for the CFRP plate. . . . .	67
6.1	SRNR for wavefields obtained in the aluminum plate (undamaged and damaged regions). . . . .	77
6.2	SRNR for wavefields obtained in the GFRP plate (undamaged and damaged regions). . . . .	77
6.3	SRNR for wavefields obtained in the CFRP plate (undamaged and damaged regions). . . . .	77
6.4	CNR for wavefields obtained in the aluminum plate, ( $CNR_r = 10.93dB$ ). . . . .	78
6.5	CNR for wavefields obtained in the GFRP plate, ( $CNR_r = 2.69dB$ ). . . . .	78
6.6	CNR for wavefields obtained in the CFRP plate, ( $CNR_r = 6.18dB$ ). . . . .	78

6.7	Comparison of the techniques for wavefield obtained in the epoxy glass, CFRP and Honeycomb plates with 50% of downsamples. . . . .	94
-----	--	----

# Chapter 1

## Introduction

### 1.1 Overview of Structural Health Monitoring

Over the last decades, monitoring the performance of an engineering structure has become a subject of increasing concern. Many structural systems, including aircraft, bridge, and pipelines incur high maintenance costs to ensure safety over their many years of operation. Therefore, there is a significant need for approaches to monitor and forecast the remaining service life. In this context, the broad disciplines of nondestructive testing and evaluation (NDT&E) and structural health monitoring (SHM) can be distinguished based on the inspection methodologies adopted: NDT&E monitoring is typically performed when the structure is offline, while SHM is based on permanently installed sensors, suitable for real-time monitoring over the whole structural life-cycle. The aim of both NDT&E and SHM is to improve safety and reduce maintenance costs. [14–17].

An SHM system behaves like the nervous system and appears extremely attractive for a wide number of engineering applications, from the aerospace industry to the chemical and power generation industries, and pipelines. Fig. 1.1 shows some possible engineering applications for SHM. SHM systems can be roughly divided into two groups: passive and active [1]. Passive technologies are based on the acquisition of signals, such as vibrations or

acoustic emissions, generated by the structural loading or by external events such as impacts, while active technologies are based on the interrogation of the structures with controlled inputs.



Figure 1.1: Engineering applications for Structural Health Monitoring.

Damage detection and predicting the remaining service of an aged structure are the most important concerns in the NDT&E and SHM communities [18,19]. By combining several sensing devices and signal processing methods, an efficient monitoring system generally requires [20] to understand the mechanics of damage and its interaction with diagnostics [21] through the computation of local and global structural features. Vibration-based methods are global damage detection techniques that can be applied to structures for detecting changes in characteristics such as natural frequencies, modal shapes, modal damping. These methods have been widely investigated in the literature [22–28]. Local inspection methodologies include

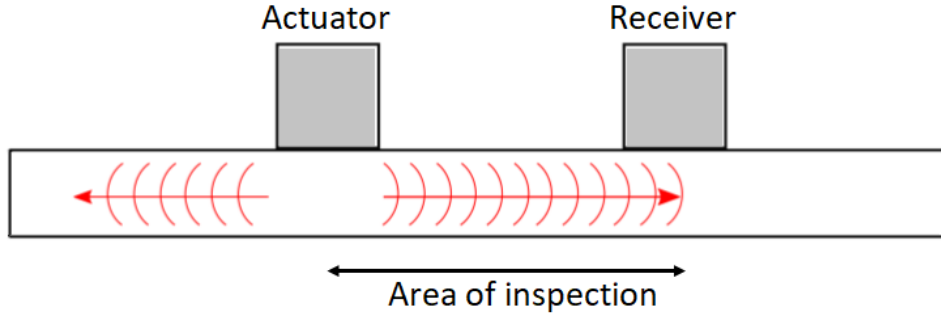


Figure 1.2: Guided wave testing (GWT)

visual inspections, ultrasonic testing, X-ray, eddy current, dye penetrates, magnetic particle, acoustic emission testing [29, 30] and Guided-wave (GW) testing, which has emerged as one of the most prominent among the techniques capable of damage detection, location, and characterization. As will be discussed in the following sections, these methods can play a significant role in monitoring and tracking the integrity of structures to estimate the location, severity, and type of damage. A schematic of the overall concept of Guided Wave Testing is shown in Fig. 1.2. In this schematic, guided waves are generated by the actuator and measured by the receiver.

A GW system consists of transducers for actuation and sensing of elastic waves. The transducers are connected to signal generators or data amplification and acquisition systems for sensing. Data acquired by multiple sensors are usually transferred to a central processing unit to predict and estimate the location and size of defects and consequently, the remaining useful life of the structure. In some embodiment, the generated waves are sensed with non-contact device which allow for the acquisition of the propagating wavefield on large areas.

The goal of this thesis is to investigate guided wave-based techniques to locate, and visualize defects in materials from Guided Wavefield Imaging (GWI).

## 1.2 Guided Waves based SHM

Guided waves are elastic waves whose wavelengths are comparable to or greater than the thickness of the structure they propagate in. More specifically, guided waves are categorized into four main wave types based on various boundary conditions: Lamb, Rayleigh, Love, and Stoneley. Lamb waves exist in thin plates or layers as they propagate along the stress-free boundaries [31], Rayleigh waves [32] which propagate close to the free surface of elastic solids [33], Love waves, Stoneley and Scholte waves that travel at material interfaces [34–37].

One of the advantages of Guided Waves (GW) is the capability to propagate over large areas with reduced attenuation [38,39]. GW are well suited for non-destructive evaluation of a wide variety of structures and assemblies (composites, multi-layer structures, bonded or welded joints, etc.) and can qualitatively (and to some extent quantitatively) reveal the presence of a large variety of existing damages [9,40–42]. For example, Castaings et al. [43] reported that transmission and reflection coefficients measured in the scattering field can be inversely used to size the cracked zones. Thanks to these features, in recent years, countless GW strategies have been proposed for detecting, locating and characterizing damage [44–51].

## 1.3 Guided wavefield Imaging

The wavefield imaging is an advanced technique for Damage identification and localization at the SHM system. Wavefield imaging refers to acquiring wavefield data over an area in order to study the time or frequency evolution of wave reflections, and, in particular, the scattering and wave speed changes that resulted from the presence of damages. Scattered wave directions are shown in Fig. 1.3. Scattered waves that propagate in the same direction as incident waves are referred to as forward scattering while scattering in the opposite direction is generally referred to as backscattering.

The analysis of these signals can provide insights into the properties of the materials and the characteristics of damages and acoustic sources. Wavefields can be actuated and sensed with various techniques, such as

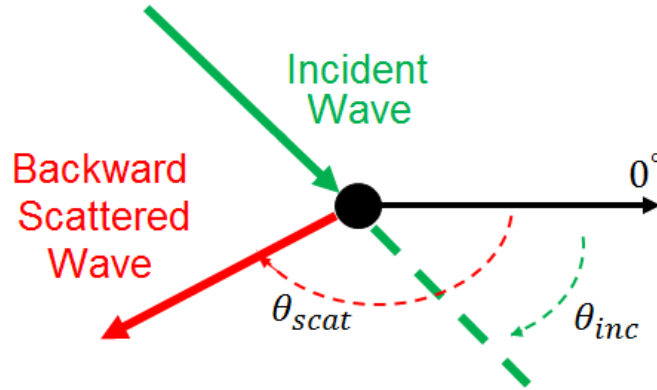


Figure 1.3: Illustration of incident and scattered waves.

those based on air-coupled probes or scanning laser Doppler vibrometers. However, wavefield imaging requires the collection of a large amount of data. Moreover, even in the laboratory environment, measurements should be often repeated and then averaged in order to avoid the effect of acquisition noise. Therefore, there is a recognized need in reducing and compressing a large number of sampled waveforms to reduce the acquisition time.

## 1.4 Motivations and objectives

This thesis will focus on inspection systems, where wavefields are generated by a fixed piezoelectric transducer and measured by scanning laser Doppler vibrometers (SLDV), or air-coupled moving transducers. The use of air-coupled transducers, which have the advantage of lower cost and fast scan speeds when compared with SLDV, have several disadvantages, mainly related to data quality. Conversely, in the case of SLDV, the principal disadvantage is that it needs several hours of automatic measurements, and time-consuming averaging procedures are often necessary to improve the signal-to-noise ratio (SNR) of ultrasonic responses.

Accurate detection of damage in plate like structures is the primary purpose of wavefield imaging procedures. Wavefield imaging may provide

details of guided waves propagation from the source, reflections from specimen boundaries, and scattering from discontinuities within the structure which may be associated to defects. Several imaging algorithms have been implemented for identifying and characterizing damage in the plate-like structures, such methods enable the measurement of structural response with high spatial resolution. However, most of the damage identification techniques require a long scanning time to achieve a high SNR for damage imaging results, e.g. one to six hours can be required to scan a  $10 \times 10 \text{ cm}^2$  square area. Therefore, the need to implement efficient, fast, and reliable wavefield scanning techniques while preserving the accuracy of detection has become increasingly important.

Given the current limitations of Guided Wavefield Imaging techniques, the purpose of this dissertation is to develop novel and rapid GW imaging approaches for plate-like structures. The main goal is to show the effectiveness of the proposed methods, leading to an increase in the speed of inspection, without sacrificing the quality of wavefield images.

## 1.5 Contribution and Organization

The main contributions of this Thesis are:

- It is shown that a consistent reduction in the number of scan points (up to 90% of the Nyquist sampling grid) can be achieved by combining Compressed Sensing (CS) and Super-Resolution (SR) techniques trained with a large dataset for enhancing image resolution in Ultrasonic wavefield while minimizing the acquisition time [52].
- The development (and validation through comparative studies) of novel damage detection techniques usable in various structural components and compatible with the removal of up to 80% of Nyquist sampling scan points.

This document is organized as follows:

- A brief review of Lamb waves based inspections is proposed in Chapters 2 and 3. In particular, technologies for Guided wave excitation



and sensing systems will be reviewed in Chapter 2, while Chapter 3 describes damage imaging methods based on Lamb waves, by distinguishing methods based on in situ sensors from non-contact methodologies based on the scanning of wavefields (Guided Wavefield imaging - GWI).

- Chapter 4 presents the theory of Compressive Sensing (CS) and its application in the context of full wavefield inspections.
- Chapter 5 presents the development of a rapid algorithm for wavefield imaging based on a combination of CS and Convolutional Neural Networks (CNNs). In particular, the main goal of this Chapter is to show the effectiveness of combining CS with deep learning methods. It is shown through dedicated metrics that the combined use of CS and Super-Resolution CNNs can lead to a high-quality recovery of wavefield images in structures with a reduced number of samples. Moreover, this document analyzes how crucial, in the quality of the High Resolution (HR) image recovery, can be the creation of a large and representative training database of wavefield images and the proper tuning of CS parameters. Then, a novel wavefield imaging method, which is subsequent to the acquisition phase, will be investigated in order to locate the existing damage. This work has been published in [52].
- In Chapter 6, the Compressive Sensing acquisition process is evaluated in terms of suitability to compute image features for damage detection. In particular, this thesis will show the results related to the application on the CS wavefield data of multiple analysis algorithms, namely the local Wavenumber Estimation technique [53], the Cumulative Kinetic Energy [54], and the differential CS imaging. The latter technique is based on the recovery of the full wavefield signal by using different sparsity promoting dictionaries and different subsampling strategies. This work has been published in [55]. Moreover, it will be proposed a methodology for damage detection based on Laplacian filtering. Several experiments were performed on aluminum, composite and

epoxy structures to illustrate the pros and cons of the different damage imaging modalities.

- Finally, Chapter 7 draws the conclusion of this dissertation and presents possible future directions and open areas in GWI research.

# Chapter 2

## Guided Waves Detection

### 2.1 Fundamentals of Lamb waves

Lamb wave propagation analysis conveys a rich informative content regarding the subsurface abnormal features of the inspected structures [56]. The characteristics of the propagating waves in a structure are also influenced by variations in environmental and operational conditions [57–59]. Consequently, in Lamb waves inspections, it is necessary to compensate for temperature effects [60–62], and those generated by the applied stress [63–66].

Lamb waves are multimodal (meaning that multiple wave modes may propagate in a given frequency interval), and dispersive, (meaning that the phase velocity is a function of frequency) [67]. Dispersion curves and mode shapes are important features of guided waves, and they are directly related to both the intimate structure and mechanical properties of the medium, in parallel to the edges of plates and through the entire thickness. Dispersive and multi-modal characteristics are significant challenges in Lamb wave analysis [68, 69], and, consequently, the first steps to develop appropriate data analysis algorithms for damage detection are related to the estimation of the wave speed of the propagating guided wave modes [1].

Two types of Lamb waves modes are usually defined in plate structures: symmetric (S) and antisymmetric (A). The interactions of the fundamental Lamb waves with symmetrical and asymmetrical discontinuities have been documented by Benmeddour et al. [70]. A symmetric mode often implies

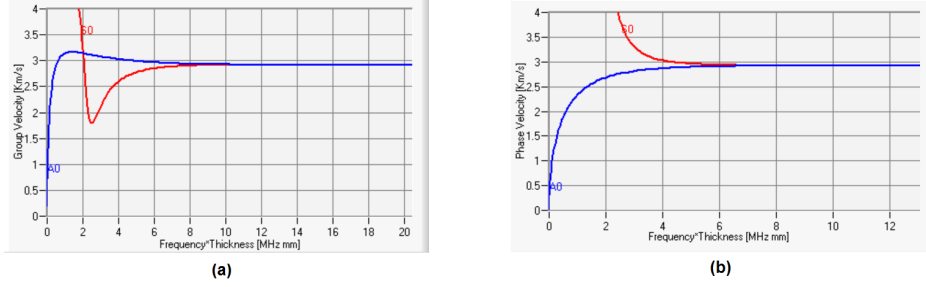


Figure 2.1: Dispersion curves of a 1 mm thickness aluminum plate: (a) group velocity dispersion curves, and (b) phase velocity dispersion curves.

thickness bulging and contracting while an anti-symmetric mode presents constant-thickness bending [71]. Fig. 2.1 shows dispersion curves of a 1 mm thickness in the aluminum plate. The dispersive nature shows the guided wave speed changes with respect to frequency. For damage diagnostics, Lamb waves are usually generated by a surface-mounted or embedded PZT actuator. Depending on the frequency-thickness product, an infinite number of modes may exist in the waves. However, only the first symmetric (S0) and antisymmetric (A0) modes are commonly used by limiting the frequency of the diagnostic wave under a cut-off, above which the higher order modes like A1 and S1 appear. Symmetric modes have more radial in-plane displacement of particles, whereas anti-symmetric features mostly out-of-plane displacement. The distinct particle motion patterns of the two modes create possibilities of using a specific mode to detect a particular type of damage Fig. 2.2.

The analytical description of Lamb waves in a plate is provided by the Rayleigh–Lamb equations. In particular, the wavenumber,  $k$ , of a possible propagating Lamb mode for a given frequency,  $\omega$ , is found as a real solution to the Rayleigh-Lamb characteristic equations:

$$\frac{\tan(qh)}{\tan(ph)} = -\frac{4k^2qp}{(k^2 - q^2)^2}, \text{ S Modes} \quad (2.1)$$

$$\frac{\tan(qh)}{\tan(ph)} = -\frac{(k^2 - q^2)^2}{4k^2qp}, \text{ A Modes} \quad (2.2)$$

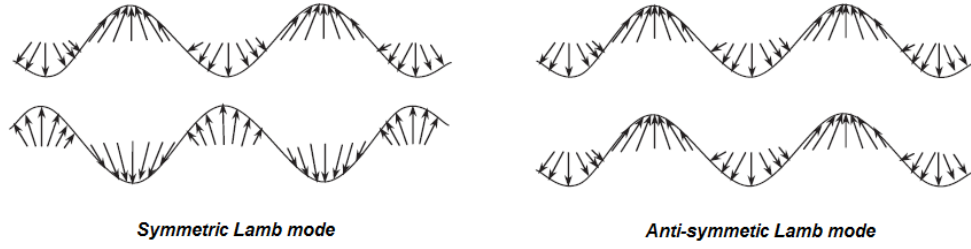


Figure 2.2: Symmetric and anti-symmetric Lamb wave modes.

$$p^2 = \frac{\omega^2}{c_L^2} - k^2, \quad q^2 = \frac{\omega^2}{c_T^2} - k^2, \quad \text{and} \quad k = \frac{\omega}{c_p}$$

where  $h$ ,  $k$ ,  $c_L$ ,  $c_T$ ,  $c_p$ ,  $\omega$  are the half plate thickness, wavenumber, velocities of longitudinal and transverse modes, phase velocity and wave circular frequency, respectively. It was found that (2.1) gives rise to a family of waves whose motion is symmetrical about the midplane of the plate, while (2.2) gives rise to a family of waves whose motion is antisymmetric about the midplane.

Modeling and simulation efforts for guided wave in the context of SHM date back to early 1990. The literature in this area encompasses understanding wave characteristics and dispersion relation, wave-damage interaction, transducer structure coupling, the effect of environmental factors, etc. Modeling methodologies can be numerical, analytical and semi-analytical. Review article on simulation methods for guided wave (such as [72–74]) provides a compilation of such important studies.

## 2.2 Sensing and actuation of guided waves

Guided ultrasonic wave detection can be either based on transducers bonded to the inspected structure or non-contact transducers. The choice of transducers is mostly based on factors such as sensitivity to mechanical responses, compatibility with the geometry of the structures, the efficiency of stress or energy transfer, lower level of interference of transducer dynamics with the wave propagation, frequency of operation, or environmental conditions [75].

Various types of transducers such as piezoelectric, inter-digital, macro-

fibre and microelectro-mechanical systems are utilized for actuation and registration of signals of propagating elastic waves [76, 77]. Air coupled transducer and Laser Doppler Vibrometer (LDV) are tools capable of measuring a wavefield in an area [78].

### 2.2.1 Piezoelectric contact transducers

Guided waves can be excited and sensed by piezoceramic (PZT) based transducers bonded to a specimen [79]. Other alternatives are piezoelectric wafer active sensors (PWAS) (Fig. 2.3 a) [1, 80], comb transducers [81] (Fig. 2.3 b), macro fiber composites (MFC) (Fig. 2.3 c), angled piezoelectric wedge transducers [82–85] (Fig. 2.3 d) which have been used as both actuators and sensors in non-destructive testing systems [67], polyvinylidene fluoride (PVDF) transducers and fiber optic sensors [86–88] (Fig. 2.3 e), and electromagnetic acoustic transducers (Fig. 2.3 f) [89].

PWAS are small, light and suitable for surface-mounting or embedding in structures. Furthermore, PWAS can serve several purposes, such as high bandwidth strain sensors and exciters, resonators, and embedded modal sensors, therefore many researchers investigated the modeling of transducer-structure interaction [90–93], also including the effect of the bonding interface [94–98]. In recent years, many researchers studied how PWAS actuators can achieve more flexibility and directionality [99, 100]. In particular, the PZT guided wave actuation and its mechanisms have been well established [1, 80, 101–104]. It is worth noting that piezoelectric actuators, even when circularly shaped, may generate non-axisymmetric wavefield amplitude distribution [93].

### 2.2.2 Air-coupled transducers

Air-coupled ultrasonic testing (AUT) is based on transducers interacting with a specimen through a thin layer of air [105] (Fig. 2.4). AUT has shown potential for non-contact inspection of built-up structures [106–108]. Air-coupled probes can insonify and detect leaky guided waves from the component by exploiting as coupling agent the pressure field in air actuated by the probe, when the probe is driven as an actuator, or received by the

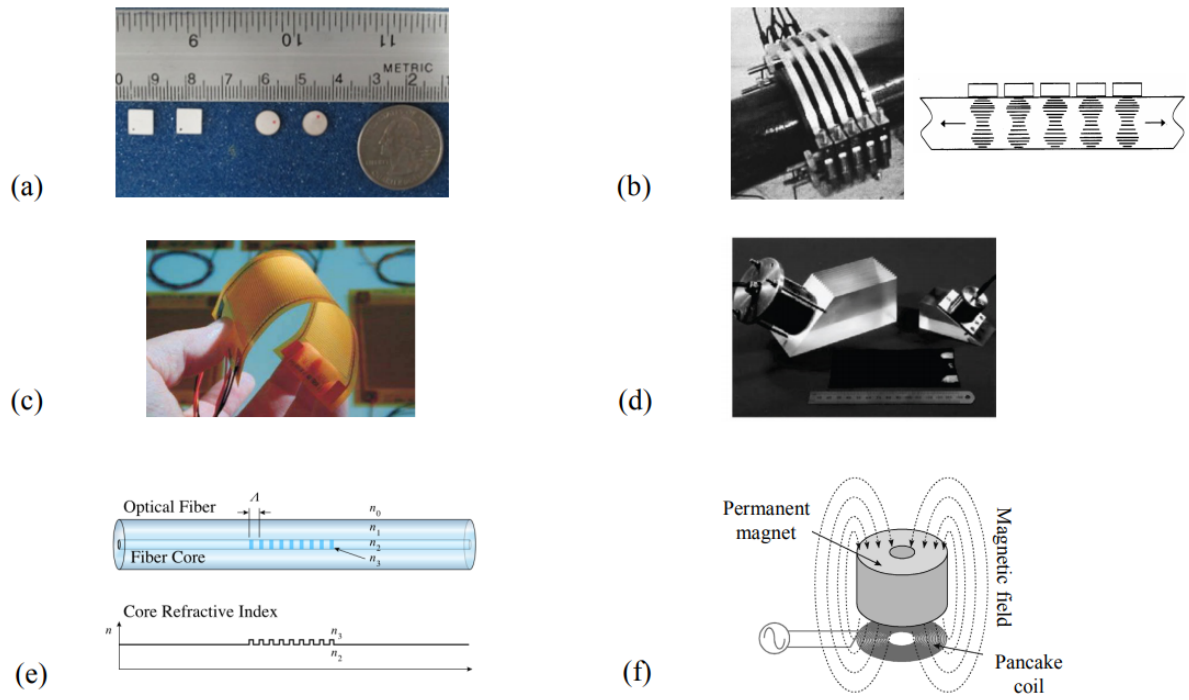


Figure 2.3: Examples of various transducers: (a) PWAS [1]; (b) Comb transducer [2–9]; (c) MFC [8]; (d) Wedge transducers [10]; (e) FBG [11]; (f) EMAT transducer [12].

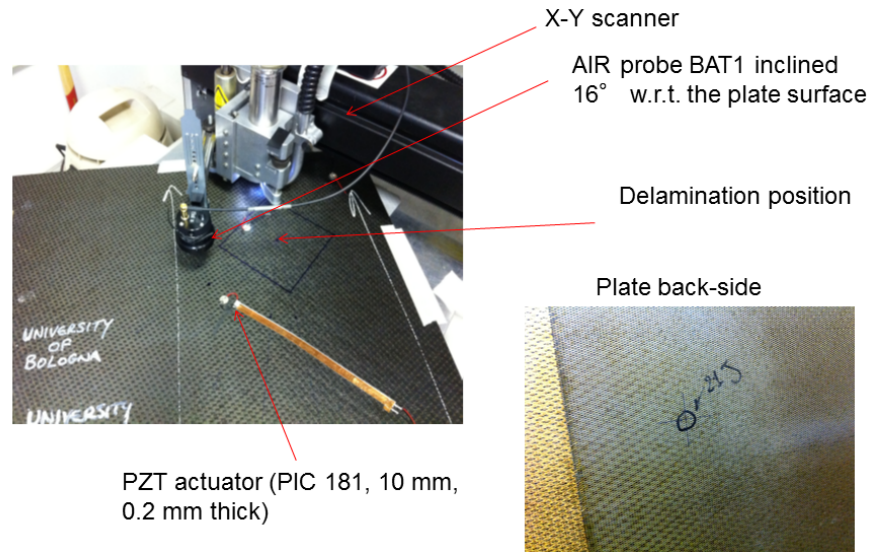


Figure 2.4: Composite plate and Air-coupled transducer.

probe from the component in case of sensing [109]. In addition, air probes can detect over the defect area high-frequency wave components, due to the contact nonlinearity of the defect vibrations [110, 111]. The advantages of AUT include fast scan speeds, low cost, the possibility to excite pure Lamb wave modes [112–114] and to inspect irregular and inaccessible regions under harsh environments. However, AUT has also several disadvantages, mainly related to data quality [115]. Because of the difference of impedance between the air and the specimens, guided waves generated by air-coupled transducer are often of low amplitude [106, 116–120]. In [121], a new system of air-coupled transducer has been designed to generate higher amplitude guided waves in composites. The setups described in [122–126] are examples of hybrid systems in which PZT transducers are used as guided wave actuators and an air-coupled transducer is used to measure the propagating waves.



### 2.2.3 Laser Doppler Vibrometry

A Laser Doppler Vibrometer (LDV) is a device that employs a Laser beam and the Doppler effect to measure the velocity of a moving object [127] Fig. 2.5. Optical Lamb wave measurements started in [128] by using an optical fiber Michelson interferometer, and [129] concentrated on a portable laser vibrometer that was developed for surface vibration measurement [130]. Laser vibrometry sensing provides a series of images that visualize the wave propagation and interaction. The advantage of SLDV is the possibility of automatic measurements over a large number of grid points. To improve the signal-to-noise ratio of full wavefield measurement, signal averaging is performed. One disadvantage of SLDV is it that needs several hours of automatic measurements because the measurements are performed at one point in space for a specified time and then repeated on a very dense grid of points with the same wave excitation. A 1-D SLDV can only measure the motion along the laser beam. When the test structure is placed normal to the laser beam, the 1-D SLDV can measure the out-of-plane wave components which are well-suited for studying anti-symmetric Lamb wave modes. However, 3-D SLDV provides 3-D wave components (X, Y and Z components), which contain rich information to assist the analysis of complicated wave propagations and interactions [131].

The investigation of symmetric and antisymmetric modes of Lamb waves which correspond to a specific distribution of in-plane and out-of-plane displacements using SLDV was presented in [132–134]. Wavefield images with high spatial resolution using SLDV have been explored in [135]. Laser-vibrometers that are used for recording the surface velocities of structural components from delaminations were presented in [136, 137]. Ostachowicz et al. used a 3-D laser scanning vibrometer to measure wavefields of Lamb waves and to understand the interactions between the waves and structural discontinuities such as notch and holes [138]. Swenson et al. compared the 1-D and 3-D SLDV measurements of Lamb waves that were excited by a piezoelectric transducer [133]. They showed that the 3-D SLDV can provide both in- and out-of-plane wave components, which are especially important for the study of both symmetric and antisymmetric wave modes.

Sohn et al. used a 1-D SLDV to visualize the wave interaction with

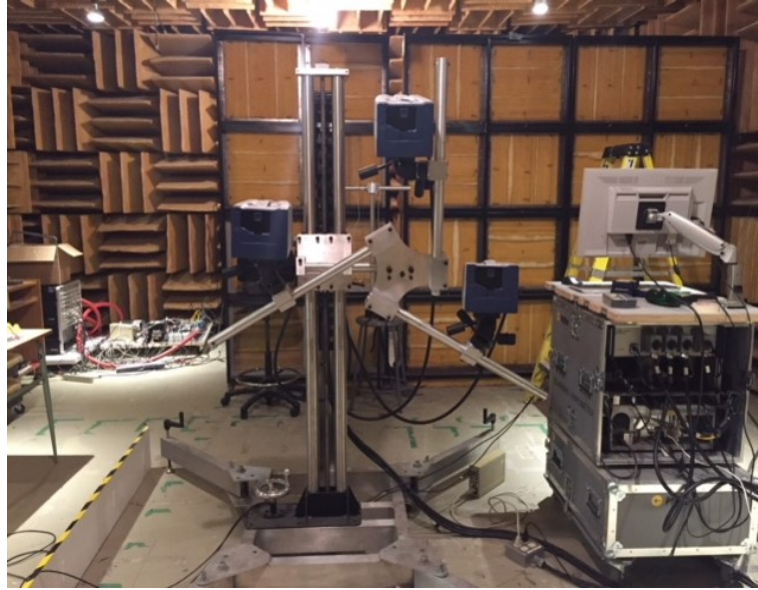


Figure 2.5: Scan Laser Doppler Vibrometer (SLDV)

delamination damage in a composite plate and observed the “standing waves” trapped by delaminations [139]. Ruzzene [140] and Michaels et al. [132,141] measured full wavefield with a 1-D SLDV to detect delamination and crack damage. They also compared the wavefield measured by the 1-D SLDV with the wavefield measured by the traditional scanning air-coupled ultrasonic transducer (SAUT) [141]. The comparison showed that the SAUT measurement has a better SNR, while the SLDV result exhibits less ringing and is more broadband. In [142], both scanning laser Doppler vibrometer and air-coupled transducer were used for crack detection and crack length evaluation.

Laser vibrometers for measuring full wavefield have been used in many other researches [13,143–160]. Such techniques are based on fixed point actuation using conventional piezoelectric transducers or contact probes. Alternatively, wavefields can be generated at scanning locations with a pulse laser and then measured with a piezoelectric transducer [161,162], or with a fixed LDV [163].

However, the most common approach is to generate the wavefield with attached piezoelectric transducers and acquire with SLDV in the spatial and temporal domains to measure the displacements associated with the elastic wave's motion. This is done using either mechanical motion to move the laser head of the LDV over the material's surface [45] or by using systems with precision controlled mechanical mirrors [164].

#### 2.2.4 Other sensing methods

Pulsed Laser [165, 166], is another wavefield imaging modality. Defect visualization using pulsed lasers for excitation has been extensively used [53, 161, 162, 167–172]. In [173–175] the generation of the guided waves at arbitrary locations was performed with pulsed lasers, then the corresponding responses were measured at a single point using a conventional ultrasonic transducer.



# Chapter 3

## Damage imaging

### 3.1 Damage imaging with in situ sensors

Guided wave SHM technologies based on phased arrays of permanently installed piezoelectric transducers have been widely investigated in the literature [6, 176–184]. Sparse arrays concepts [185, 186], time-reversal methods [187–189] and tomography [190, 191] are the ground basis for the implementation of several damage imaging methods. which show a good application potential [6, 185, 187, 192–198].

Unfortunately, the propagation of the guided waves is very complex because it is influenced by different conditions, such as holes and irregular geometries [199], presence of corrosion [200], somehow unpredictable scattering in the defective area characterized by delaminations [201], or various crack orientations [202], reflection of guided modes in the inspected specimen [203], and also the sensor-pair, that may be attached on the two opposite sides of the plate at the same location or in several different arrangements [202, 204, 205]. Moreover, guided wave propagation is characterized by its dispersive and multi-modal nature which further complicates the acquired signal interpretation. Therefore, the analysis of Guided wave requires the use of signal processing techniques such as dispersion compensation [206, 207] and mode filtering [140, 141] or the usage of multiscale representations [208, 209]. For example, in [210], adaptive dispersion compensation was performed to improve imaging of defects on an aluminium

plate using a distributed transducer array.

There exist some techniques to experimentally measure the dispersion relations of a media such as the one presented in [211], which investigated an accurate determination of dispersion curves by applying the matrix pencil method. The authors of this study were able to extract automatically smooth curves of different symmetric (S) and antisymmetric (A) Lamb wave modes from experimentally measured data on an aluminum plate and compared to theoretical values. Regarding the guided wave mode extraction and separation, a time–frequency ridges based method has been proposed by Xu et al [212]. In addition, with the known dispersion curves, the dispersive Radon transform can be used to extract the individual mode component efficiently [213]. Moreover, works in the area of time–frequency representations (TFRs) have been proposed in [214–216]. In order to improve TFRs for guided wave signals, a considerable amount of work has been done, including short-time Fourier transform [217], reassigned spectrogram [218], warped frequency transform [219], and chirplet transform [220] that have been employed to process Lamb wave signals.

The techniques for signal analysis can be very sophisticated when the transducers are used in a purely passive manner for the localization and characterization of acoustic events occurring in the structures (e.g. those Due to impacts). In this application domain, impact localization is based on the time differences of arrival through peak detection techniques and the analysis of the structure geometry [221–223] as well as on the study of impact mechanical model [224, 225].

Most of the scientific literature, however, is dedicated to active methods, i.e. methods in which one or more transducers are used to actively interrogate the structures. Some of these methods are reviewed in the next subsection.

### 3.1.1 Guided wave array imaging

Active guided wave array imaging methods can be categorized into two groups: i) sparse array imaging, in which sensors are sparsely distributed over the structure being inspected [185–189], and ii) phased-array imaging, in which sensors are physically placed close to each other [6, 12, 176–179,

181–184].

In both cases, it is important to minimize the array elements in order to reduce the complexity associated to transducers and to the processing of the large amounts of recorded data. This can be done by optimizing the sensor positioning, as well as by increasing the resolution of the damage localization procedures [226–229]. Diligent et al. [230] measured the evanescent waves generated at a free end of a plate upon reflection of the first symmetrical mode. They found that evanescent modes can be neglected at distances five times the plate’s width.

Guided wave sparse arrays for SHM were proposed by Wang et al. [192]. In their approach, a synthetic time-reversal imaging algorithm was used to process sparse array data to obtain an intensity image for locating and sizing damage. Later, Michaels and Michaels applied time shift averaging algorithms to differential Lamb wave signals filtered at multiple frequencies [231]. A set of images corresponding to each center frequency is then generated and combined to form an image for locating the damage. They used time shift averaging to process the differential signals filtered at multiple frequencies, resulting in multiple images of the component being inspected. Later, Michaels et al. presented an in-situ sparse array for damage detection, localization and characterization in plates by using differential signals between diagnostic signals and baselines, and the delay-and-sum algorithm to construct intensity images [185].

Hall and Michaels proposed a weighting coefficient to the traditional DAS method to decrease the noise and artifacts by using the so-called minimum variance distortionless response method [232]. The time-reversal, delay-and-sum and MVDR methods all rely upon baseline subtraction to separate scattered signals from direct arrivals and geometrical reflections. However, in real applications, baseline data may not be available, or the baseline data may have been recorded under mismatched environmental or operational conditions. Lee et al. developed a baseline-free imaging method which was based upon estimating the source waveform and then adaptively removing the direct arrival from each received signal [184].

A multiparameter approach was presented in [233] using the reconstruction algorithm which enhanced the damage localization of single detection framework by extracting different features from the propagating wave.

Sparse arrays have been used for various applications. For example, a baseline subtraction method has been implemented for a numerical study on guided wave based damage detection in the corrugated steel door of a commercial shipping container [186]. Cho and Lissenden used a sparse array on a multi-fastener joint for fatigue crack growth monitoring [234]. Yu and Leckey used Lamb-wave based sparse arrays by a frequency-wavenumber domain analysis using 2-D Fourier transform for crack detection in an aluminum plate [154]. Su et al. utilized the time of flight (TOF) between the incipient fundamental symmetric Lamb waves and delamination-induced fundamental shear horizontal mode to triangulate the delaminations in composite laminates [193].

Chen et al. have developed a load differential method that evaluated the crack detection with the load dependence of the crack openings. The delay-and-sum imaging algorithm was used to visualize the opening effects on the cracks due to the increasing tensile loads [235].

Guided wave phased arrays with closely spaced sensors have been studied intensively and show some advantages such as efficient and flexible control of the beam direction, reinforced wave energy in the beam, large area inspection with a small sensing area, improved signal-to-noise-ratio, and promising damage detection results [6, 12, 176–179, 181, 182, 236–243].

An embedded-ultrasonic structural radar (EUSR) with 1D linear phased arrays for thin-wall metallic structures was developed in [176]. This work showed the capability of 1D linear phased array in detecting both broadside and offside cracks in metallic plates. However, 1D linear arrays have some limitations, such as the degradations of beamforming properties at angles close to  $0^\circ$  and  $180^\circ$  directions, and the half-plane mirror effect, that does not allow discriminate between a target placed above the array and a target placed below the array. [1]. 2D planar arrays have been adopted to overcome the limitations of 1D linear arrays because they can perform full-range (360 deg) beam steering and reduce the mirror effect, as well as provide more control and optimization parameters for improving the array performance [1, 6, 12].

Wilcox presented omnidirectional guided wave EMAT transducer arrays which contain a circular pattern of elements for the inspection of large areas of aluminum plates based on phased arrays with 2D circular configurations



[12]. The work [6], proposed by Giurgiutiu and Yu, is based on the use of piezoelectric wafer active sensors (PWAS) that can be directly mounted on the surface of plate-like structures or even embedded between layers of composite structures. This work studied the 2D phased arrays design and its implementation for damage detection in aluminum plates. There are various 2D phased array configurations, such as cross-shaped array, rectangular ring array, circular ring array, and concentric circular array.

Koduru et al. proposed a 2D phased annular array transducer that can generate mode controlled Omni-directional guided waves in isotropic plate [244]. The work by Ambrozinski et al. proposed an efficient tool for the designing of 2D phased arrays for isotropic plates [238]. Yoo et al. developed a 2-D spiral phased array by using piezoelectric-paint for isotropic panels [182]. A frequency-steerable 2D periodic array of emitters can be used to drive all the elements simultaneously with a narrowband, or tone burst, signal such that there is constructive interference in a particular angular direction [183].

The detection of defects can be further complicated by the anisotropy of the inspected materials. Phased arrays for composite materials have been investigated in [178] and by Yan and Rose in [245]. Rajagopalan et al. used weakly anisotropic wave modes [246]. They adopted an array of a single transmitter and multiple receivers (STMR) for damage localization in a composite plate.

Vishnuvardhan et al. used the STMR array to detect impact induced delamination damage in a quasi-isotropic composite plate. Leleux et al. used ultrasonic phased array probes for long range detection of defects in composite plates [242]. Purekar et al. adopted a linear PZT sensor array and a finite element modeling method to obtain frequency narrowband Lamb wave signals and the corresponding wavenumber curve respectively. Based on the wavenumber curve, a spatial-wavenumber filter was realized to be a directional filter to search the damage direction [178]. Osterc et al. studied the beam-steering of 1D linear arrays in composite laminates [247].

In composite plates, the group velocity direction is not always parallel to the phase velocity direction. Moreover, the wavenumbers, phase velocity and group velocity in an anisotropic composite plate are directionally dependent [192, 248, 249]. Therefore, they have significant influences on the

phased array beamforming.

## 3.2 Damage imaging based on wavefield analysis

As anticipated, Guided wavefield Imaging (GWI) is an inspection technique relying on the collection of large amounts of information provided by the detection of guided wavefield to identify surface and subsurface defects. The wavefield is stored in 3D arrays  $W(x, y, t)$ , taking into account measurement locations and time instants. Wavefield imaging has proven to be a valuable tool for studying guided waves in various materials and quantifying their interactions with defects [250]. For example: in [251], wavefield imaging was used to identify damage in reinforced-concrete walls by using LDVs to measure guided waves, in [252], to localize thickness variations in aluminum using sub-1 MHz waves; and in [253] to investigate characteristics of piezoceramic sensor damage and degraded performance. Additionally, efforts have been made to use LDVs and wavefield imaging for composite material inspection. In this field, several studies have shown effective identification of matrix cracking and layer delaminations [254].

### 3.2.1 Wavefield imaging basics

The term *guided ultrasonic wavefield imaging* is generally referred to as the analysis of a series of images representing the time evolution of propagating guided ultrasonic waves over large areas and, possibly, their interaction with defects. During the last decade, ultrasonic wavefield imaging technology has proven to be an effective nondestructive ultrasonic inspection tool for various engineering materials [140, 250, 255, 256].

The wavefields can be generated and received with various kinds of transducers and may allow diagnosing the health of structures by determining the location and the extent of the defects [141]. Typically a source at a fixed position generates ultrasonic waves in a structure, and a scanning receiver collects the corresponding ultrasonic wave responses across a predefined spatial sampling grid on the surface. Using the scanning measurement data

sets, wavefield images are generated, where the interaction between propagating waves and the structural features can be observed and determined. Fig. 3.1 shows some snapshots of wavefields at 60  $\mu\text{s}$ , 81  $\mu\text{s}$  and 110  $\mu\text{s}$  in the aluminum plate 5mm with cross shaped cut.

Fig. 3.2 shows a surface plot of waves propagating in an aluminum plate and interacting with a clamped mass, (in-plane and out-of-plane directions). Fig. 3.3 gives the experimental results of displacements in the z-direction at 150 kHz, 75 kHz, and 40 kHz excitation frequencies.

Another example of a guided ultrasonic wavefield image is depicted in Fig.3.4 (a) and (b), which show the experimental setup and a snapshot at 98 $\mu\text{s}$  of waves propagating in a simple aluminum plate and interacting with a clamped mass. The multiple wavefronts generated by the embedded transducer and scattered by discontinuities are clearly visible. In the selected frequency range (75 kHz), two modes (S0 and A0) are generated, but A0 mode has much greater amplitude than S0 mode.

The wavefield imaging technology usually is combined with an additional data processing method to extract damage-induced scattered wavefields, thereby visualizing possible damage in a structure [13, 141, 257].

Time slice images, waveform envelopes, accumulated kinetic energy [255, 258], and standing wave filtering [259], are useful features to highlight the characteristics of the inspected medium and the presence of defects. For example, Fig.3.4 (c) shows that the processing of wavefield acquisitions can be adopted to highlight the position of the defect [13, 54, 146].

Alternatively, the collected data can be analyzed in time and frequency domains [141] or by using multiscale representations [209], as will be further discussed in the next section.

### 3.2.2 Wavefield analysis and Damage Detection techniques

Damage detection techniques can be based on measurements from distributed sensors. However, these techniques have several limitations in-accurate damage localization and characterization [154]. These limitations can be overcome through the acquisition and analysis of full wavefields [13, 132, 153, 260–262].

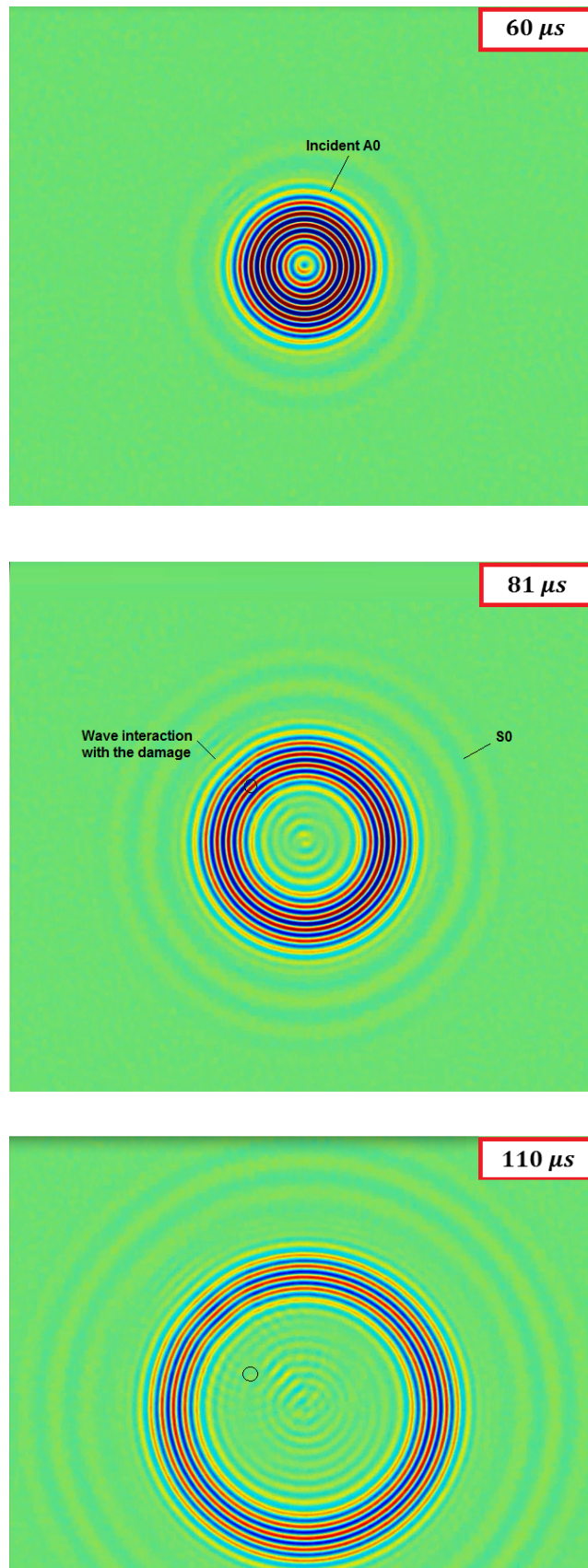


Figure 3.1: Snapshots of wavefields at 60  $\mu\text{s}$ , 81  $\mu\text{s}$ , and 110  $\mu\text{s}$  in an aluminum plate.

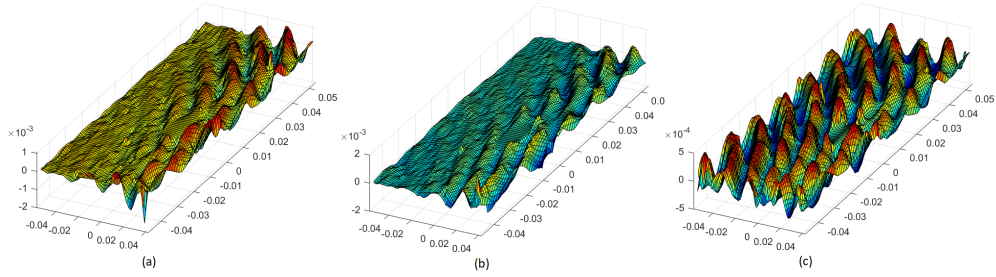


Figure 3.2: Wavefield propagation imaging plots for 75 kHz excitation: (a) in-plane X direction, (b) in-plane Y direction and (c) out-of-plane Z direction

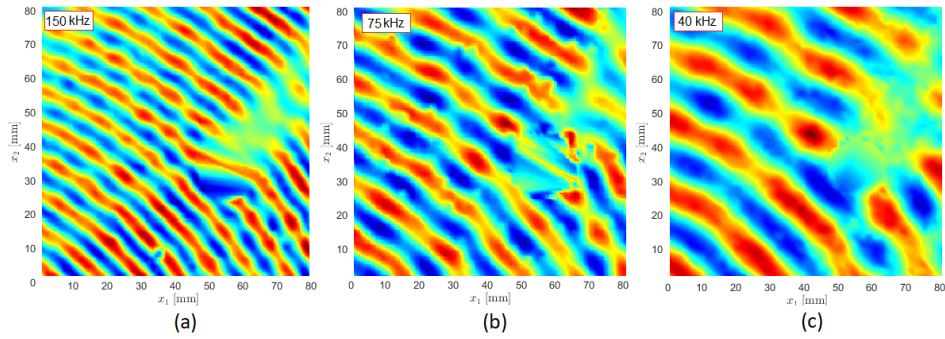


Figure 3.3: Experimental results of displacements in the z direction: (a) at 150 kHz excitation, (b) 75 kHz excitation, (c) 40 kHz excitation.

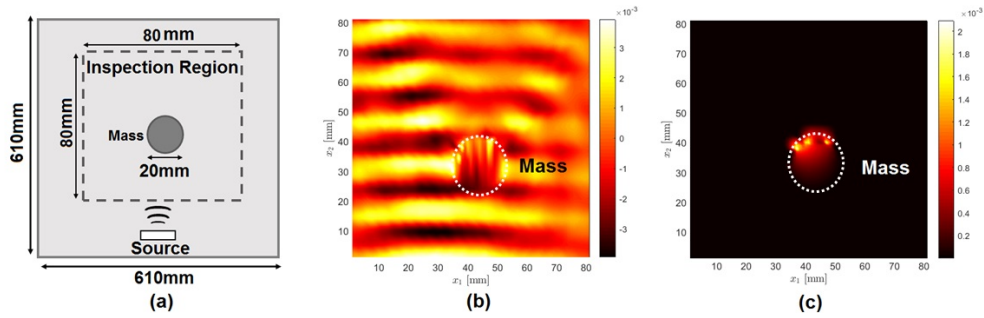


Figure 3.4: (a) Sketch of a setup constituted by a simple aluminum plate with a clamped mass, (b) Snapshot at  $t = 98 \mu s$  of the measured ultrasonic wavefield; (c) damage image generated by computing the maximum value of the wavenumber-domain filtered signal, as suggested in [13]. The white dot circle represents the actual position of the clamped mass.

## Applications

Wavefield imaging methods may contribute to the understanding of how guided waves interact and are reflected by structural features such as edges, stiffeners, bolts, rivets, and various types of defects such as cracks [185], corrosion [263], and impact damage [139]. It is worth noting that delaminations [264], and hidden delaminations [265], [152] have unique scattering patterns [266], which can be tracked with full wavefields representations.

In a recent work [267], the improved imaging method was developed to obtain accurate results of localization and sizing damages in metallic plates and composite laminates. Kudela et al. [268] studied the relation between impact energy and BVID detectability through a suitable wavenumber-adaptive image filtering.

Due to multiple reflections that may be induced by delamination in composite plates, most detection methods focus on locating the delamination, without quantifying its depth and size [139, 141, 178, 193, 258, 269–283].

However, the quantification of delamination depth can be attempted by performing a deeper characterization of the wave propagation in the defective region [272, 284–286]. In particular, Ramadas et al. studied the interaction of the antisymmetric  $A_0$  mode with symmetric [287]. In particular, the trapped

energy phenomenon of guided waves in delaminated composites has been studied experimentally through the use of wavefield images obtained from laser vibrometry tests [139,288]. It was shown that the incident wave energy is divided above and below the delamination, propagating independently through the upper and lower laminates. As waves propagate towards the edge of delamination damage, a portion of wave energy is reflected backwards from the far edge of the delamination. Then the reflected waves in the damage region pass back above the delaminated area and experience reflections at the original entrance to the delamination region. The process is repeated until the energy is dissipated. This complicated behavior has been revealed by computer simulations and visualization in [289]. In [273], a damage detection procedure of aerospace composites based on three-dimensional (3D) wave interaction was described. Glushkov et al. also observed wave energy trapping and localization in strip delamination from wavefields measured by laser vibrometry [269]. Guided wave energy trapping in delamination damage has also been quantitatively studied in [284]. The trapped waves compared to those traveling in the undamaged area have different wavenumbers. Therefore, it is expected that by analyzing the trapped waves, the delamination dimensions can be quantified [284].

### **Frequency-wavenumber representations**

Although guided wavefields in time-space domain can visually show guided wave propagation and interaction, detailed wave signatures such as wave modes, frequencies, and wavenumbers are not directly available. To achieve these detailed wave signatures guided wavefields can be converted from the representation in the time-space domain to the representation in the frequency-wavenumber domain. For example, spatial Fourier transform (FT) approaches have been proposed for scattering analysis in composite structures in [290,291].

By using multidimensional FT, time-space wavefields are transformed to frequency-wavenumber spectra, where different wave modes and wave components can be easily identified and extracted for further analysis [139,141,285,286,292,293]. FT 2D and 3D methods have been applied to wavefield data by many authors to quantify propagation and filter

wavefields to extract, for example, a single-mode or propagation directions [140, 141, 270, 294].

Alleyne and Cawley used 2D FT to transform a guide wavefield into the frequency-wavenumber domain where they obtained detailed dispersion information of multi-modal Lamb waves [295]. Wilcox et al. proposed a dispersion compensation method by transforming the frequency spectrum to the wavenumber domain through linear interpolation and then compensating the dispersion effect in the wavenumber domain [180]. Hayashi and Kawashima used a filtering technique in the frequency-wavenumber domain and successfully separated A0 and S0 modes [270]. Ruzzene presented a damage visualization technique by filtering the damage reflection waves in the frequency-wavenumber domain and demonstrated an application on crack damage visualization [140]. Michaels et al. presented source removal and wave mode separation techniques by using frequency wavenumber filtering and demonstrated applications on delamination and crack detection [141]. In [294], 3D frequency-wavenumber filtering has been applied to bulk wave propagation to separate Rayleigh, shear and longitudinal waves.

Moreover, it has been proven in [296] that the value of the wavenumber of the Lamb waves changes locally in the presence of a defect. This information was exploited in the already mentioned work by Rogge and Leckey [272], where it was demonstrated that wavenumber information can be used to determine the approximate depth and size of near-surface delamination damage.

Flynn et al. proposed a local wavenumber estimation method, using a Q-switched laser system and a fixed sensor to detect local impact delamination in a complicated composite component [53]. By using the local wavenumber estimation method (also referred to as acoustic wavenumber spectroscopy - AWS) impact damage on composites, fatigue cracks, and wall-thinning in aluminum have been detected [172, 297–300]. For these tasks, the optimum excitation frequency and mode selection strategy were proposed by Moon et al [301].

Again basing on local Fourier-domain analysis, Jeon et al. compared the performances of acoustic wavenumber spectroscopy (AWS) and local wavenumber mapping (LWM) [302], while in [303], a novel Lamb Wave Local Wavenumber Approach for Characterizing Flat Bottom Defects in an



Isotropic Thin Plate was presented. A different setup was proposed in [255], where the quantification of crack dimensions in aluminum plates by using spatial wavenumber imaging was presented. It is worth to mention the work described in [286], which demonstrated delamination depth quantification by correlating local wavenumber data for multiple excitation frequencies to dispersion curves.

### Scattering patterns investigation

Other approaches to damage imaging use scattering patterns in order to improve damage sensitivity and reduce localization errors [232, 304]. One possible method for characterizing the scattering is by computing transmission and reflection coefficients that define an amplitude or energy ratio between the incident and scattered waves. However, the description of scattering along a specific incident direction does not provide information about alternative scattering directions [305]. Such limitation has been addressed by describing all scattering directions through angular patterns for a specific incident direction. The collected information has been used for the characterization of scattering from notches, through-holes, and cracks via experimentation and simulation in isotropic media using guided waves [306, 307].

Karunasena et al. [308] showed how scattering from a crack of various lengths behaves differently for S0 and A0 modes and a work by Karim and Kundu [309] showed that scattering amplitudes from an incident A0 wave mode continually reduces as the length of a crack approaches the thickness of the plate. Chen, in [310], showed how scattering patterns could be represented by a scattering matrix through experiments with guided waves in aluminum. Bratton et al. [311] showed that a specific relations between scattering amplitude and crack depth exists but it is typically difficult to extract this information from the scattered signals. Correlation between S0 wave velocity and crack density was revealed through experiments by Toyama et al. [312] and led to a crack detection method that utilizes this changing S0 wave velocity [313].

As anticipated, delaminations can have various effects on scattering behavior based on their size, depth, and shape. However, delaminations are

more sensitive to the A0 wave mode [314], The depth of the delamination can significantly affect S0 scattering [281]. The size of delamination and the central frequency of the incident wave also play a significant role in how scattering occurs [315]. Hu et al. [204] verified that backscattering occurs more strongly at the entrance of the delamination rather than the exit one through an experimental study, and that the overlap of multiple backscattered waves in smaller delaminations can produce higher amplitude waves.

Overall, the interaction of the A0 wave mode with delamination produces backscattered waves that are smaller in magnitude than forwarding scattered waves [316]. This variation in scattering amplitude as a function of direction has been studied using finite element modeling (FEM) to analyze the angular-dependent scattering nature of delaminations and results have also been compared with some experimental studies [317]. In the work by Murat et al. [318] finite element simulations were compared with experimental data regarding angular scattering from multiple incident angles and it was shown that delamination depth and width can have a significant effect on scattering directivity.

### **Root mean square and cumulative kinetic energy methods**

One of the simplest but most efficient techniques of damage imaging is based on vibration energy distribution and utilizes the calculation of a root mean square (RMS) [153].

The general idea of this visualization method is based on evaluating the signal energy in every point on the surface of the inspected area. The RMS has been successfully used in various damage detection applications [319–325].

In particular, a damage imaging example based on the root mean square error (RMS) technique was presented in [326].

Localization of damaged rivets in a stiffened plate structure based on RMS maps was conducted by Radziński et al. [321]. This work used a five-cycle burst of different frequencies (5 kHz, 35 kHz, and 100 kHz), and the best results were obtained in the case of an excitation signal of 100 kHz, where the wavelength was shorter than the distance between two

rivets. Another work by Marks et al. [324] presented also experimental investigations on the detection of disbonds in a stiffened panel based on the RMS plots. They used Wave packets with three different frequencies (100 kHz, 250 kHz, and 300 kHz). The authors concluded that the excitation frequency is an important parameter for the inspection of disbonds. In the conducted works, only higher frequencies (250 kHz and 300 kHz) were able to detect damage. The RMS method was improved to be more effective in damage detection by defining a weighting mechanism (weighted root mean square - WRMS- method [327]). The performance of WRMS was demonstrated using aluminum, composite plates and composite elements of a helicopter, all with damage being simulated by a mass. Lee and Park [322] considered an aluminum plate with notches of various orientation based on RMS images. They showed that only tangential damage could be successfully detected without a comparison to the intact images. They also applied the WRMS to localize the notches and corrosion areas in aluminum plates.

Saravanan et al. [323] used radially weighted and factored RMS for damage localization in an aluminum plate. Detection of delamination in a composite T-joint using RMS images was studied by Geetha et al. [328]. Kudela et al. [319] studied the detection of delamination in a composite plate using WRMS They also proposed a selective WRMS that enabled the elimination of edge reflections.

Pieczonka et al. [320] performed the detection of disbond inserts in composite elements by using RMS and three-dimensional (3D) scanning. In the conducted experimental investigations, it was noticed that in-plane RMS maps provided a better indication of damage than out-of-plane RMS maps. The main problem that is connected with damage imaging using weighted RMS is in the fact that the weighting factor is set arbitrary with no clear explanation for the choice of a specific value [153].

### **Statistical and Machine Learning techniques**

Various neural architectures are used in SHM, the most popular being the multi-layer perceptron. It consists of several neurons connected in a layered feed-forward architecture. They are trained using the backpropagation

gradient descent algorithms. Su and Ye [329] presented a feed-forward ANN scheme for Lamb wave-based damage detection in a composite laminate. Neural Network (ANN)-based Crack Identification in Aluminum [330]. A similar multi-layer feed-forward ANN has been implemented for damage detection in a thick steel beam using guided waves [331].

Damage indices based on Lamb wave response of complex geometry structures are used in conjunction with ANN for damage detection in the reference [332] and aluminum skin panel [333]. Agarwal and Mitra [334] reported Lamb wave-based damage detection in the aluminum plate using ANN and SVM approaches together with matching pursuit for increasing the sparsity of data and denoising it. Anomaly detection via dictionary learning to detect damage was presented in [335]. In [336], an application of Artificial Neural Networks for damage detection using Lamb waves, in this work the wave propagation data are used to determine the location and degree of damage in metallic and composite plates. The EMI-based methods have been combined with various machine learning algorithms and used for extending the capacity of the conventional methods to classify the damage types [337]. In [338], artificially deteriorated signals of Lamb waves were used to train the novelty detection (ND) system for damage detection. In particular, auto-associative Neural Networks were trained using principal components calculated on the basis of experimentally measured signals. A deep learning interpretation of ultrasonic guided waves was proposed in [339] to achieve fast, accurate, and automated structural damaged detection. In this work, the accuracy of the damage prediction rate is 99.98%.

An online monitoring technique proposed for continuous fatigue crack quantification and remaining fatigue life estimation is developed for plate-like structures using nonlinear ultrasonic modulation and artificial neural network (ANN) [340]. [341] introduced a guide waves-based local probability-based diagnostic imaging (PDI) method for multi-damage identification, which included a path damage judgment stage, a multi-damage judgment stage, and a multi-damage imaging stage. Methods using a single baseline subtraction are not viable for long-term embedded SHM systems. It has been shown that by using a database of baselines recorded over various experimental conditions, long-term detection stability could be obtained despite temperature variations [342].

# Chapter 4

## Compressive Sensing of wavefields

### 4.1 Summary

One of the main challenges faced by the structural health monitoring community is acquiring and processing huge sets of acoustic wavefield data collected from sensors such as scanning laser Doppler vibrometers (SLDV) or air-coupled scanners. In fact, extracting information that allows the estimation of the damage condition of a structure can be a time-consuming process. This section describes the Compressive Sensing (CS) of wavefield that can lead to fast scanning and improved damage detection<sup>1</sup>.

### 4.2 Rapid and Sparse Lamb waves inspection techniques

As discussed in Chapter 2, Wavefields can be actuated and sensed with various techniques, such as those based on piezoelectric or scanning laser Doppler vibrometers. The principal limitations of wavefield-based imaging

---

<sup>1</sup>This chapter is based on the paper *Full Wavefield Analysis and Damage Imaging Through Compressive Sensing in Lamb Wave Inspections*, Keshmiri et al.

methods are i) the collection of a large amount of data, since measurements should often be repeated and then averaged to increase the signal to acquisition noise ratio, and, most importantly, ii) the associated time for the acquisition. Therefore, there is a recognized need in reducing the number of sampled waveforms to minimize the acquisition time.

The first attempts to perform rapid inspection techniques for detecting and quantifying damage in large composites were proposed in [280, 343].

More recently, the work described in [344] is based on a two-step procedure that performs at first a fast global inspection with phased array to identify damaged areas and then high-density wavefield measurements for precise damage quantification.

Other research and development efforts are addressing this issue by considering continuous-wave excitations [172, 256], and multi-point laser vibrometry [345]. The authors of [346] demonstrate the effectiveness of the dictionary learning baseline subtraction framework. In [347], Alguri demonstrates a data-driven approach for computing optimal transforms/models from data of a surrogate structure. Frequency Domain Instantaneous Wavenumber (FDIW) was introduced by Mesnil et al. in [285]. In this work, guided wavefields analysis provide an abundance of information regarding the health of the waveguide, in particular, instantaneous wavenumber estimation was used to quantify delamination damage in composites.

The wavefield acquisition process can benefit also from the recent advancements in the Sparsity-based signal processing research. One noticeable example in this field is given by the so-called *Compressive Sensing* theory.

CS [348, 349] is an efficient technique for sampling a signal with fewer samples than the number dictated by classic Shannon/Nyquist theory. The assumption underlying this approach states the possibility of reconstructing a signal without loss of information by feeding a limited number of measurements into an  $\ell_1$  norm minimization procedure. As a prerequisite, the signal must be sparse, i.e. it should be well approximated by a linear superposition of a few atoms of an appropriate basis. In addition, the second condition to be met is incoherence, which is related to the idea that the elements of the sparsifying basis should be poorly correlated with the sampling functions [350].

The CS found several applications in the SHM field: for example, a

## 4.2. RAPID AND SPARSE LAMB WAVES INSPECTION TECHNIQUES 37

damage detection study for bridges by recovering compressive-sensing data was performed in [351], while, in [352] a compressive sensing technique for detecting damage using a Gaussian random matrix of a structure was proposed.

The application of CS in wavefield acquisition was proposed for the first time in [353] (to the best of this author knowledge). In particular, sampling point distribution strategies and decomposition bases were investigated to produce the best recovery for a subsampled wave field signal obtained with a scanning laser Doppler vibrometer (SLDV).

Mensil et al. [354] proposed a method to reconstruct a guided wave signals from compressive measurements and presented the achieved performance. A subsequent paper ([355]) presented a sparse wavefield reconstruction and damage detection technique based on the analysis of guided wavefields by locating the non-pristine structural reflectors generating scattered wavefields. Many other researchers also did considerable work in Lamb wave sparse decomposition with tone-burst (or dispersive tone-burst) dictionaries [356–358]. In [359] and [360], a methodology named sparse wavenumber analysis was adopted for reconstructing the dispersion relations of a plate through sparse measurements. This technique has also been applied to pristine wavefield reconstruction [361]. The dispersion and amplitude modulation for each mode could also be experimentally tested using sparse wave number analysis [362]. The potential of Sparse wavenumber analysis (SWA) was investigated in [363] through the retrieval of the sparse representations of three different wave propagation systems, namely oscillations on a fixed string (standing waves), Lamb waves traveling in an isotropic plate, and guided waves in a unidirectional anisotropic plate. They also refer to the anisotropic model and reconstruction process as anisotropic SWA (ASWA), [363], 2D-SWA [364], and Fourier reconstruction (low-pass filtering/interpolation).

High-resolution dispersion curves extraction is proposed in [365]. In [366], the authors used sparse wavenumber analysis, sparse wavenumber synthesis, and data-fitting optimization to accurately model damage-free wavefield data. In [367], the authors localized and estimated the severity of damage through a compressive sensing technique using blind feature extraction. Possible strategies to further increase CS performance include model-based

CS [368].

The concept of sparsity which is the ground basis of CS can be used also for signal analysis purposes. Without attempting to reconstruct wavefield, a technique to locate defects relying on a sparse representation of the wavefield and dictionary learning is proposed in [335]. Krishnaswamy designed a Gabor dictionary for Lamb wave sparse decomposition and the extraction of meaningful wave components for damage localization in aluminum plates [369]. Chang designed an adaptive Gaussian dictionary to distinguish overlapping wave components of Lamb waves for pipeline crack inspection [370]. The excited tone-burst were used as dictionary atoms in sparse decomposition for characterizing pipeline defect in [371]. Similarly, in [372], dispersive tone-bursts were used to build a dictionary for location-based sparse decomposition and damage imaging.

The authors of [373] presented an accelerated laser scanning technique to localize and visualize damage by using compressive sensing and a binary search approach. To improve the reconstruction quality of the compressed sensed images, different solutions were investigated in [55, 125, 374]. In particular, [374] proposed the fast analysis of wave speed (FAWS) algorithm to process waveforms recorded by a random-spaced geophone array based on a CS platform. Compressed sensing was also adopted for mode separation in far field in the frequency-wavenumber domain [69]. Similarly, the separation of multi-mode components of Lamb wave signals through the reconstruction of pure mode basis signals calculated from phase and group velocity information was proposed in [375]. A weighted sparse reconstruction-based anomaly imaging method is proposed for plate-like structures by [376].

The authors of [377] presented a sparser representation of guided waves obtained by incorporating information of the measurements in polar coordinates (polar sparse wavenumber analysis - PSWA). [378] investigated the efficacy of guided wave reconstruction techniques, based on sparse wavenumber analysis, for predicting the behavior of guided waves in composite materials. In [379], the authors presented an ultrasonic wavefield reconstruction technique by developing the sparse characteristics of the wavefield, to realize damage localization and imaging in a metal plate and used the coherence coefficient of power spectral density to evaluate the wavefield reconstruction effect. In [380], a decomposition dictionary was established by



taking excitation waveform, dispersion, multi-mode, amplitude modulation, and environmental conditions into consideration. Finally, [381] analyzed the ultrasonic data using a tomographic and a probabilistic reconstruction algorithm based on different reconstruction techniques and several damages ultrasonic parameters analysis.

Therefore, when applicable, CS can be used to boost the acquisition of multidimensional ultrasonic data by reducing the dimensionality of processed samples and at the same time speeding up the data acquisition phase [382–385].

### 4.3 Compressive Sensing theory

The Compressive sensing (CS) theory [386] states that, under specific conditions, a signal  $s \in R^n$  can be reconstructed from a linear combination of random measurements  $y \in R^m$ .

The measurements  $y$  can be expressed as the result of a vector-matrix product:

$$y = \Phi s \quad (4.1)$$

where  $\Phi \in R^{m \times n}$  is the measurement matrix, and  $m$  is the number of measurements, which can be much smaller than the dimension of the signal ( $m \ll n$ ).

In this section,  $s$  is the wavefield signal acquired according to the Nyquist sampling theory in both the spatial and temporal domains, and called *full grid*, the grid of sampling points used to acquire  $s$ . More specifically, if  $n_1$ ,  $n_2$ , and  $n_3$  are the numbers of scan points in the  $x_1$  and  $x_2$  coordinates (i.e. the spatial grid), and the number of samples in the time axis, respectively, the dimension of the signal  $s$  sampled according to the full grid is  $n = n_1 \times n_2 \times n_3$ .

Our main goal is to implement a procedure capable to reduce the inspection time in order to minimize the offline period of the inspected structure and to use more efficiently the (typically, very expensive) wavefield acquisition equipment. To achieve this goal, it is important to reduce the number of the spatial scan points, while discarding time samples is not beneficial with this respect. For this reason, in the current work, the signal

is not subsampled in the time domain but only in space. Thus, the number of measurements  $m$  is equal to  $m_1 \times m_2 \times n_3$ , with  $m_1 < n_1$  and  $m_2 < n_2$ .

In order to reduce the number of acquisition points in space, and consequently the acquisition time,  $\Phi$  is defined as a subsampling operator, more specifically, as the Jitter subsampling operator presented in [387]. Such subsampling is based on the definition of an equispaced under-sampled grid of scan points which are subsequently perturbed. The jitter sampling scheme is illustrated in Fig. 4.1. More formally, the coordinates of the undersampled scan points are given by:

$$x_{u1} = i_k \cdot \eta \cdot \sqrt{\gamma} + \varepsilon_i, \quad i_k \in [0, 1, \dots, m_1 - 1] \quad (4.2)$$

$$x_{u2} = j_k \cdot \eta \cdot \sqrt{\gamma} + \varepsilon_j, \quad j_k \in [0, 1, \dots, m_2 - 1] \quad (4.3)$$

where  $\gamma \in [1, \infty)$  is the undersampling factor,  $\varepsilon_i$  and  $\varepsilon_j$  are random variables independent and identically distributed on the interval  $(-\frac{\eta}{2}\sqrt{\gamma}, \frac{\eta}{2}\sqrt{\gamma})$ , and  $\eta$  is the spatial spacing imposed by the Nyquist theorem. In the full grid, each scan point has coordinates  $(x_1, x_2) = (i \cdot \eta, j \cdot \eta)$  with  $i \in [0, 1, \dots, n_1 - 1]$ , and  $j \in [0, 1, \dots, n_2 - 1]$ . From Eqs. (4.2) and (4.3) it follows that, in the undersampled grid, the number of acquired data points is equal to  $N = m_1 \times m_2$  with  $m_1 = \lfloor n_1 / \sqrt{\gamma} \rfloor$ , and  $m_2 = \lfloor n_2 / \sqrt{\gamma} \rfloor$  ( $\lfloor \cdot \rfloor$  being the nearest integer function). It is worth noting that the jitter sampling intrinsically prevents the presence of large gaps between scan points (maximum gap  $\leq 2\eta\sqrt{\gamma}$ ), which may cause the improper reconstruction of standing waves localized in small regions or rapidly vanishing wave-packets.

CS performs on the assumption [386] that  $s$  has a sparse representation in some model basis  $\Psi \in R^{n \times n}$ , as following:

$$s = \Psi\alpha \quad (4.4)$$

More specifically,  $s \in R^n$  is called  $S$ -sparse if  $\alpha$  has only  $S < m < n$  non zero elements, i.e.  $S$  is the number of nonzero elements of  $\alpha$ . Furthermore, the down sampling measurement matrix  $\Phi$  has to be incoherent with the model basis  $\Psi$  [350]. This means that  $\mu \sim 1$ , being  $\mu$  the measure of the largest correlation between any two elements of  $\Phi$  and  $\Psi$ :

$$\mu(\Phi, \Psi) = \sqrt{n} \max_{1 \leq i, j \leq n} |\langle \varphi_i, \psi_j \rangle|, \quad (4.5)$$

where  $\varphi_i, \psi_j$  are the rows of  $\Phi$  and the columns of  $\Psi$ , respectively, and  $\mu \in [1, \sqrt{n}]$ .

Many algorithms have been proposed in the literature to find the sparse coefficients  $\alpha$ , ranging from convex relaxation techniques to greedy approaches such as Orthogonal Matching Pursuit (OMP) [388], to iterative thresholding schemes such as Iterative Hard Thresholding (IHT) [389], [390] and Iterative Soft Thresholding (IST) [391], [392].

In practical cases, measurements are very often corrupted by a noise term  $\delta$ :

$$y = \Phi\Psi\alpha + \delta \quad (4.6)$$

Moreover, in most cases, data are not exactly sparse. However, when the coefficients of vector  $\alpha$  decrease exponentially in absolute value, the signal is still compressible, and the approximation of  $\alpha$  which guarantees the signal recovery with a bounded error [393] can be found by solving the following  $\ell_1$ -norm minimization problem (Basis Pursuit Denoising, BPDN):

$$\min \|\tilde{\alpha}\|_{\ell_1} \text{ subject to } \|\Phi\Psi\tilde{\alpha} - y\|_{\ell_2} \leq \zeta, \quad (4.7)$$

where  $\zeta$  is a constant related to the noise level in the data. In this work, I used the spectral projection gradient algorithm (SPGL1) [394], which solves the sequence of the following sub problems:

$$\alpha^i = \arg \min_{\tilde{\alpha} \in R^n} \|\Psi\Phi\tilde{\alpha} - y\|_{\ell_2} \text{ subject to } \|\tilde{\alpha}\|_{\ell_1} \leq \tau_i \quad (4.8)$$

The algorithm starts by defining the first tentative solution  $\alpha^0$  and the initial value ( $i = 0$ ) for the parameter  $\tau_0 = \|\alpha^0\|_{\ell_1}$ . At each iteration  $i$ ,  $\tau_i$  is updated as detailed in [395]. The iterations are stopped when a given maximum number of iterations  $i_{Max}$  is met. The recovered wavefield  $s_\Psi$  is then computed as  $\Psi\alpha^{i_{Max}}$ .

## 4.4 CS Recovery results

In [353], it was shown that the CS framework can be applied to wavefield images achieving very low reconstruction errors on average.

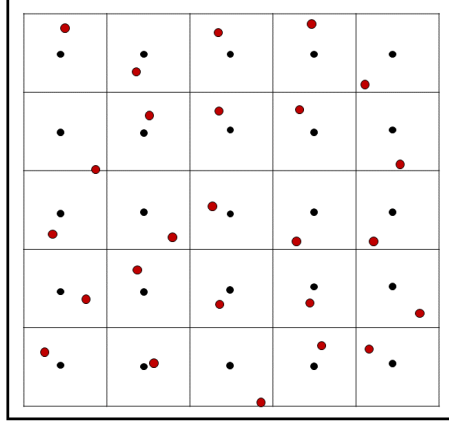


Figure 4.1: Jittered sampling of the measurement region: the black dots represent the scan points obtained by regularly subsampling the  $x_1 - x_2$  space; their position is then randomly perturbed (red circles) to define the new scan points with coordinates  $x_{u1}$  and  $x_{u2}$ .

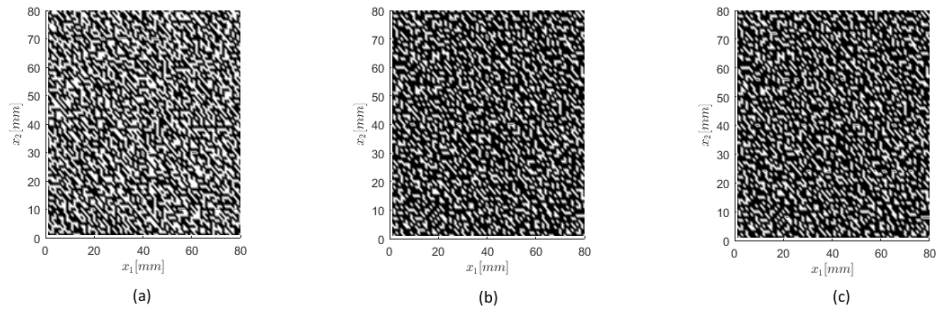


Figure 4.2: (a) Jitter masks used to undersample the acquisitions for an area of  $80 \text{ mm} \times 80 \text{ mm}$  of the aluminum plate test case: (a) 50%, (b) 33% and (c) 20% retained scan points. White dots are retained full grid scanpoints and black dots are those discarded.

To demonstrate these results, first full wavefield data were acquired according to the Nyquist sampling and used as a reference wavefield ( $s$ ) for the validation of the CS strategy. Next, as a mean to simulate the reduction of the number of acquisition points (and consequently the acquisition time), the Jitter subsampling operator  $\Phi$  described in the previous section was applied.

In particular, in the following, 3 values for the undersampling factor  $\gamma$  are considered, namely:  $\gamma = 2$ ,  $\gamma = 3$  and  $\gamma = 5$  [55]. These three values are representative of a medium (50% of retained scan points), consistent (33%) and very consistent (20%) spatial grid undersampling to show the performances of the proposed idea. An example of retained scan points by the three percentages is shown in Fig. 4.2. These percentages are referred to as the Compressive Rates (CRs) of the reconstructed wavefield which can be expressed with respect to the Nyquist sampling rate as:

$$CR(\%) = 100 \times \left(1 - \frac{N}{N_{Nyq}}\right) \quad (4.9)$$

where  $N_{Nyq}$  is the number of measurements required by Nyquist theorem. The time waveforms associated to the retained scan points provide the input wavefield data to the CS reconstruction based on the  $l_1$ -minimization. Fourier (FT), Curvelets (CT), and Wave atoms (WA) dictionaries can be used to generate multiple sparsifying model bases  $\Psi$  (a detailed analysis of these representation domains is presented again in [353]). The SPGL1 algorithm was applied with different numbers of iterations to evaluate the effect of this parameter in terms of reconstruction accuracy and damage detectability. In particular,  $i_{Max} = 30, 90$  and 150 iterations of the SPGL1 algorithm were considered as representative of a small, a medium and a large number of iterations to show the convergence of the wavefield recovery procedure. It is worth mentioning that the SPGL1 toolbox for MATLAB<sup>™</sup> [395] was used in this work, with the support of the suite Sparco [394].

For the considered CRs and number of iterations, the wavefields recovery performed by using the different sparsity promoting bases are then computed.

It is worth noting that the recovery time depends on the sparsity basis

Table 4.1: Computational time (in minutes) of the CS recovery in case of CR=50% for the aluminum plate.

Dictionary	Iteration=30	Iteration=90
2DFT	5.09	24.54
3DFT	3.45	14.00
2DCT	81.00	352
2DWA	266.00	780.00

selection as well: Table 4.1 shows the recovery times (achieved with an Intel i5/ 2.5 GHz processor, 8GB of RAM) for the case of 50% retained scan points for a  $n_1 \times n_2 \times n_3$  wavefield propagating in an aluminum plate.

The recovery of two snapshots related to the different setups are illustrated in Figs. 4.3 and 4.4. In Fig. 4.3(a), the signal acquired on a composite plate at a given time instant is shown along with the signals recovered with FFT 2D as a dictionary Fig. 4.3(b). The recovery was performed 33% measurements with respect to the original grid. Fig. 4.4 shows the signals recovered with the FFT 2D by 50%, 33% and 20% of scanpoints.

Such images can be used to qualitative evaluate the performances of the CS wavefield recovery. A quantitative assessment of this fast acquisition method was presented in [353]). In the next Chapter, it will be shown how such good recovery results can be further improved by taking advantage of a novel algorithm which post-processes the CS recovered wavefields with neural networks, while in Chapter 6 it will be shown how CS can be used for damage imaging purposes.

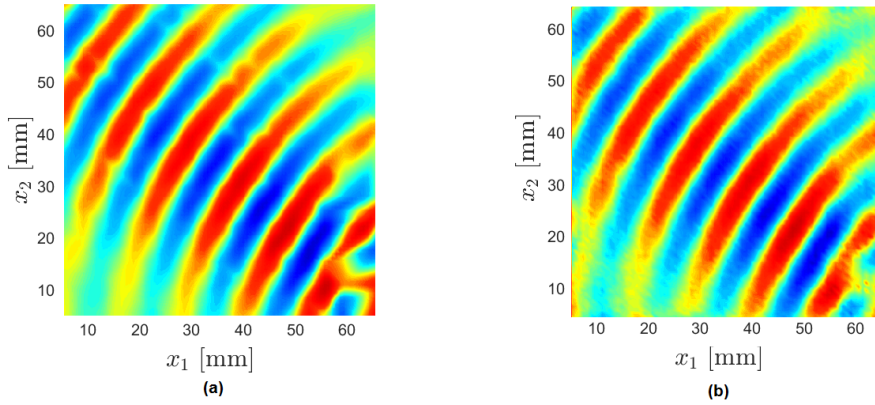


Figure 4.3: Original full wave field on simple composite plate at a given time instant (a), full wave field recovered with FFT 2-D by 33% measurements with respect to the original sampling grid (b).

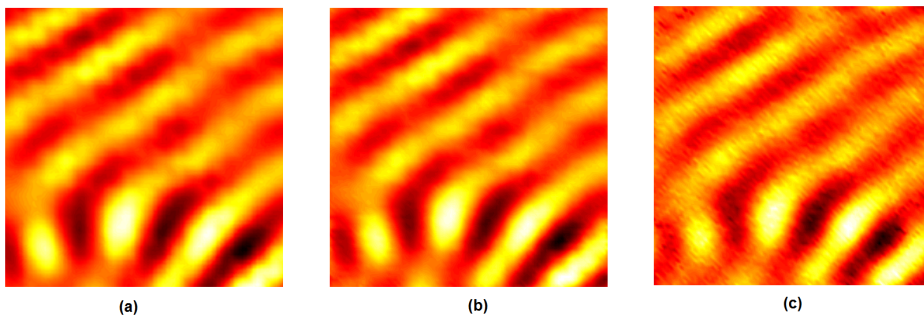


Figure 4.4: Full wave field recovered with FFT 2-D by 50% (a), 33%(b) and 20%(c) measurements with respect to the original sampling grid in the composite plate.





# Chapter 5

## CNN for Enhancing Image quality

### 5.1 Summary

As anticipated, ultrasonic wavefield imaging with a non-contact technology can provide detailed information about the health status of an inspected structure. However, high spatial resolution, often necessary for accurate damage quantification, typically demands a long scanning time. This chapter<sup>1</sup> investigates a novel methodology to acquire high resolution wavefields with a reduced number of measurement points to minimize the acquisition time. Such methodology is based on the combination of the compressive sensing methodology discussed in the previous chapter and convolutional neural networks to recover high spatial frequency information from low resolution images. A dataset was built from 652 wavefield images acquired with a laser Doppler vibrometer describing guided ultrasonic wave propagation in 8 different structures, with and without various simulated defects. Out of those 652 images, 326 cases without defect and 326 cases with defect were used as a training database for the convolutional neural network. In addition, 273 wavefield images were used as a testing database to validate

---

<sup>1</sup>This chapter is based on the paper *Deep learning for enhancing wavefield image quality in fast non-contact inspections*, Keshmiri et al.

the proposed methodology. For quantitative evaluation, two image quality metrics were calculated and compared to those achieved with different recovery methods or by training the convolutional neural network with non-wavefield images dataset. The results demonstrate the capability of the technique for enhancing image resolution and quality, as well as similarity to the wavefield acquired on the full high resolution grid of scan points, while reducing the number of measurement points down to 10% of the number of scan points for a full grid.

## 5.2 High resolution Wavefield imaging

Guided ultrasonic wavefield images quality greatly affects the subsequent image analysis and processing. In fact, structural imaging in high spatial resolution reveals accurately structural details. In other words, the amount of information that can be extracted from the wavefield is directly related to the number of points at which the wave propagation is measured, enabling accurate image diagnostic for identifying waves interaction with defects such as cracks, corrosion, and impact. In most cases, high resolution (HR) wavefield images are required to make a proper diagnosis. However, HR measuring strategies typically involve long scanning time, further increased by the adoption of extensive waveform averaging required to improve the signal to noise ratio. Therefore, there is a recognized need in reducing the number of sampled waveforms to minimize the acquisition time while increasing the signal to noise ratio without any artifacts resulting.

The Compressive Sensing (CS) method has been investigated in the previous chapter as a mean to tackle this problem by reconstructing wavefield images from a few sampling data, thus reducing the scanning time significantly [353]. To improve the reconstruction quality of the compressed sensed images, different solutions were investigated in [55]. However, the downsampling which allows meeting the quality requirements for wavefield reconstruction is still relatively modest (20-50% of scan points retained). Alternative approaches based on CS are those presented by Harley and co-workers [359, 378]. Recently, they used an autoencoder neural network to learn low-dimensional representations of wave propagation [396]. Mesnil

and Ruzzene [355] presented a sparse wavefield reconstruction and damage detection technique based on the analysis of guided wavefields by locating the nonpristine material points generating scattered wavefields. In these cases, the achieved downsampling rate is significant but the subsequent recovery is not meant to be used for HR imaging, but for the extraction of information related to wave propagation (such as dispersion curves, or anomalous reflector positions).

Therefore, high-speed and HR wavefield imaging is still an open research field. Possible strategies to further increase CS performance include model-based CS [368], or novel sparsity-based methods such as gradient-based [397], and operator splitting algorithms [398]. Although these methods are generally very efficient, it is not trivial to set their parameters to have the proper reconstruction accuracy.

Recently, Neural Networks (NN) have achieved noteworthy successes in image denoising tasks because of the strong ability to learn from data [399]. Some authors have evaluated the combined use of NNs and CS [400, 401].

The idea is to firstly recover images from compressive or low resolution (LR) samples, and then map the result into HR images by applying properly trained Super-Resolution Convolutional Neural Networks (SRCNNs) [402]. Such concepts have been used in a large number of computer vision problems, including image enhancement, such as denoising [403] and deblurring [404]. Learning based on super-resolution was shown to be capable of obtaining HR images without any over-smoothing, no ringing and jagged artifacts such as aliasing, blur, and halo around the edges [405]. The first attempt to combine CS and SRCNN in wavefield imaging was done, to the best of the authors' knowledge, in a conference paper by Park et al. [406], where some first qualitative results were presented. The approach described in Park's work was based on a training set constituted by generic heterogeneous images.

In this chapter, it is shown how crucial in the quality of the HR image recovery can be i) the creation of a large and representative training database of wavefield images and the proper tuning of CS parameters, and ii) the move from SRCNN to *Very-Deep Super Resolution* (VDSR) procedures. Deep neural network are NN with multiple layers between the input and output layers. Thanks to their complexity, they achieve superior performances with

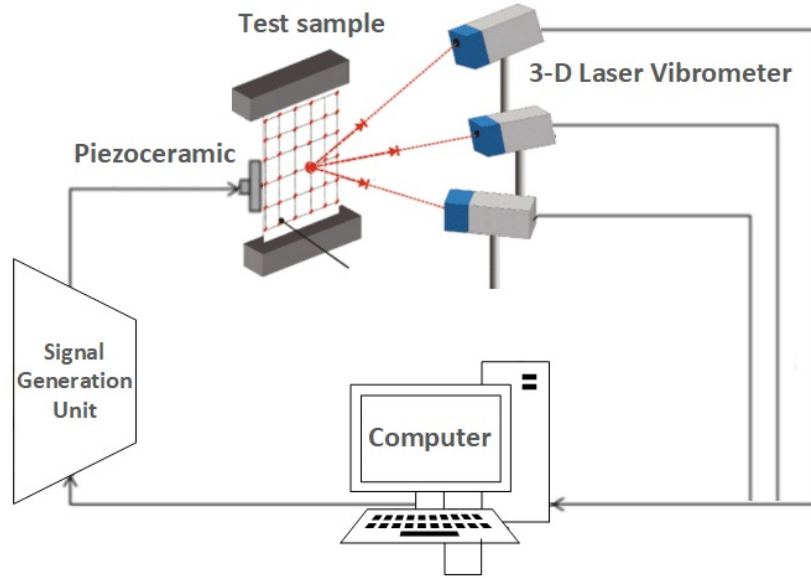


Figure 5.1: Experimental setup used to measure ultrasonic guided wavefields.

respect to conventional NN [407].

Finally, the benefit brought by the proposed approach with different performance metrics are quantified.

### 5.3 Materials and methods

This chapter focuses on guided ultrasonic wavefields generated by piezoelectric transducers attached to the inspected structures, and acquired with SLDV in the spatial and temporal domains. More specifically, non-contact measurement of the in-plane and out-of-plane velocity is performed using a 3-D Laser Doppler Vibrometer (3D-LDV) over a square grid of points to extract the required information. A sketch of the setup adopted for ultrasonic wavefield measurement is shown in Fig.5.1. Waves travel across the inspection area and are recorded at several measurement grid points.

The data is stored in 3D arrays  $W(x, y, t)$ , taking into account measure-

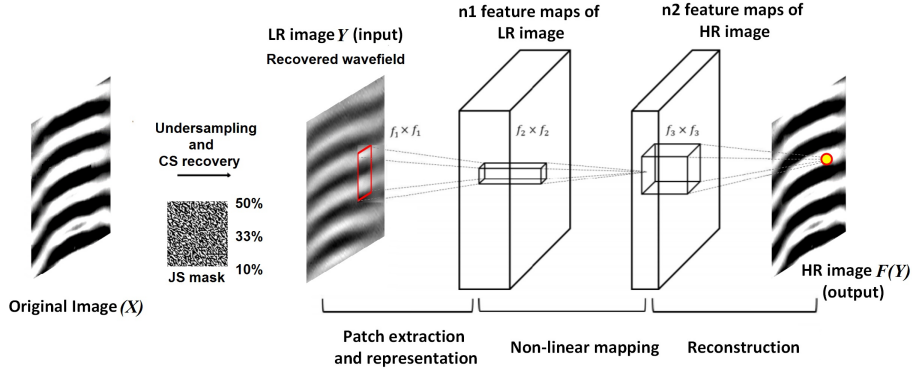


Figure 5.2: Overview of the SRCNN scheme for HR image reconstruction.

ment locations and time instants. 3D data arrays contain information that can be used for structural characterization [141].

### 5.3.1 Recovered Wavefield Images

As anticipated, low resolution wavefield data can be acquired with Compressive Sensing procedures.

In the following, the mathematical notation adopted in the Chapter 4 is used:  $s$  is the wavefield signal acquired (after averaging) in HR;  $n_1$ ,  $n_2$  and  $n_3$  are the number of scan points in the  $x_1$  and  $x_2$  coordinates (i.e. the spatial grid), and the number of samples in the time axis, respectively. Therefore, the dimension of the signal sampled according to the full grid is  $n = n_1 \times n_2 \times n_3$ .  $s$  can be reconstructed from a linear combination of random measurements  $y = \Phi s$ . In order to reduce the number of acquisition points in space, and consequently the acquisition time,  $\Phi$  acts as a subsampling operator, more specifically, the *jitter subsampling operator* [387] can be adopted.

Again, three undersampling cases were considered. These three values are representative of a medium (50% of retained scan points), consistent (33%) and very consistent (10%) spatial grid undersampling. These percentages are referred to as Compression Rates (CRs) of the reconstructed wavefield.

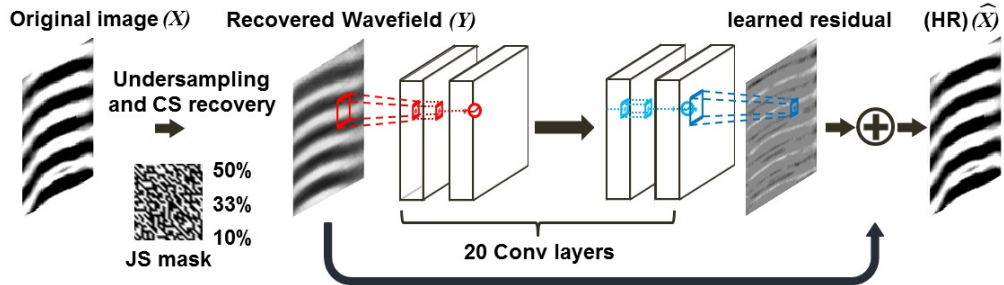


Figure 5.3: Overview of the VDSR scheme for HR image reconstruction.

Fourier (2D, 3D) exponentials have been used to generate the sparsifying model bases  $\Psi$ . The following section presents how image recovery can be improved by combining the CS recovery with conventional or deep NNs.

## 5.4 Single image super-resolution

Super-resolution (SR) [408] refers to the task of restoring HR images from LR observations, such as those resulting from compressed acquisitions. Depending on the number of input low resolution images, the SR can be divided into Single Image Super-Resolution (SISR) and Multi-Images Super Resolution (MISR) [409]. SISR has typically higher efficiency than MISR [410]. Super-resolution algorithms can be roughly divided into: i) interpolation-based methods such as bicubic interpolation [411], ii) reconstruction-based methods which are typically very efficient and fast [412–414].

### 5.4.1 Super-resolution convolutional neural network

Among learning based methods, the one based on SRCNN was the first which was applied in wavefield imaging [406]. This section has compared the results achievable with this method with the deep learning strategies which will be introduced in the following subsection. The architecture of the SRCNN is shown in Fig. 5.2. As can be seen, SRCNN is a 3-layer CNN. The tasks performed by these three layers are: patch extraction and

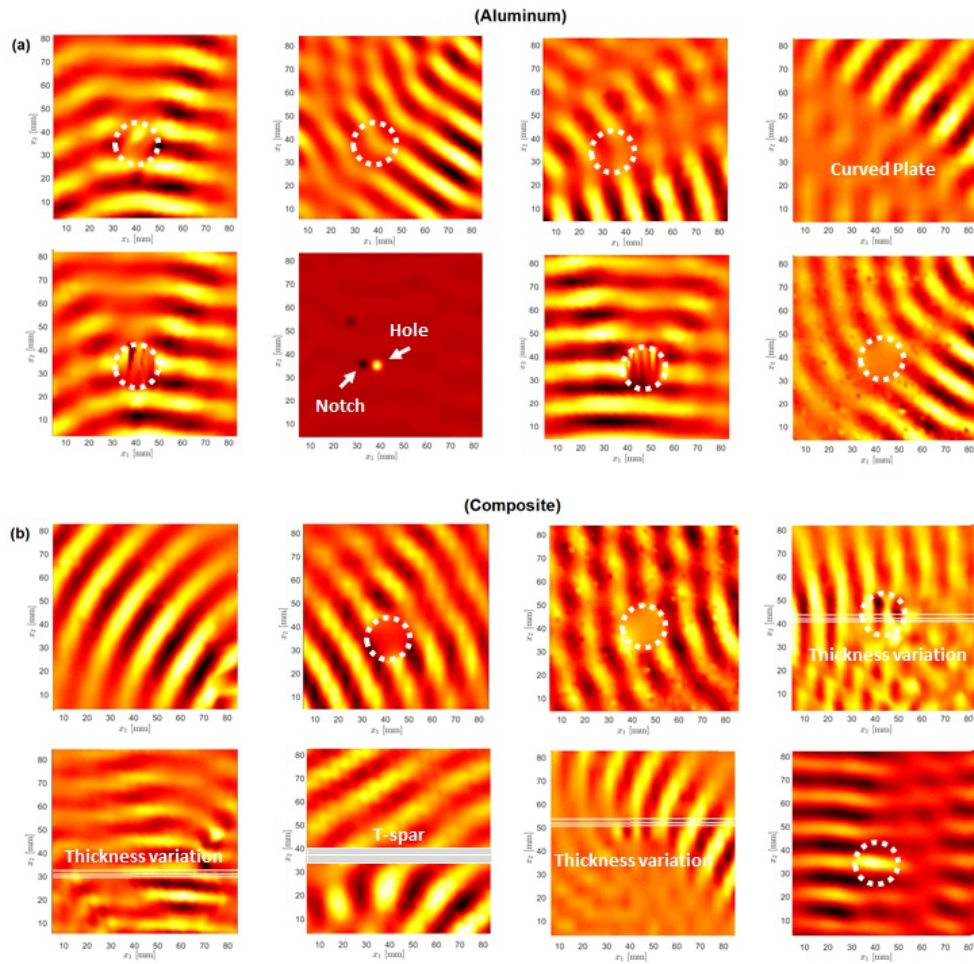

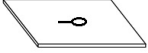
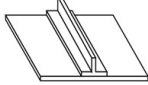
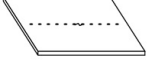






Figure 5.4: Examples of guided ultrasonic wavefield images related to Aluminum and CFRP plates setups which were used to train the SRCNN and VDSR. Plate features and mass positions (dotted circles) have been highlighted.

Table 5.1: Geometrical features of the aluminum (AL) and carbon fiber reinforced polymer (CFRP) structures

Category	Features	Thickness	Size (mm)	Illustration
AL	Simple	2 mm	610×610	
AL	Hole and defect	3 mm	620×620	
AL	T-spar	Species Change	610×610	
AL	Rivet	2 mm	620×620	
CFRP	Simple	3 mm	500×500	
CFRP	Thickness variation	Taper angle	500×500	
CFRP	T-spar	Species Change	620×620	
CFRP	Curved	3 mm	510×510	

representation, non linear mapping, and reconstruction, respectively. The *patch extraction and representation* layer extracts patch from the LR input image and compute the following mapping function  $F$ :

$$F_1(\mathbf{Y}) = \max(0, W_1 * \mathbf{Y} + B_1) \quad (5.1)$$

where  $Y$ ,  $W_1$ ,  $B_1$ ,  $f_1$  and  $n_1$  represent the LR image, the applied filters, the biases, the filter size, and the number of filters respectively. More specifically,  $W_1$  corresponds to  $n_1$  filters, whose size is  $f_1 \times f_1$ , being  $f_1$  the spatial size of a filter. Following [402]. The output is thus composed of  $n_1$  feature maps, and  $B_1$  is an  $n_1$ -dimensional vector.

As can be seen in Fig. 5.2, in this work, the input to SRCNN is made of the wavefields recovered from the CS procedure, and acquired with different



compression rates (50%, 33% and 10%). Moreover, the CS-recovered images have been cropped into a set of  $f_{sub} \times f_{sub}$ -pixel sub-images, to further expand the training set.

The middle layer involves a *non-linear mapping*, which maps the feature vectors in  $F_1$  non-linearly to another set of feature vectors ( $F_2$ ). The operation of middle layer is as follows:

$$F_2(\mathbf{Y}) = \max(0, W_2 * F_1(\mathbf{Y}) + B_2) \quad (5.2)$$

where  $W_2$  is an array of  $n_2$  filters whose size is  $n_1 \times f_2 \times f_2$ , and  $B_2$  is an  $n_2$ -dimensional vector.

Finally, the *reconstruction* layer generates the final HR image. The operation of the last layer is as follows:

$$F(\mathbf{Y}) = W_3 * F_2(\mathbf{Y}) + B_3 \quad (5.3)$$

$W_3$  has a size of  $n_2 \times f_3 \times f_3$ , and  $B_3$  is a vector. In this work,  $n_1=64$ ,  $f_1=9$ ,  $n_2=32$ ,  $f_2=5$ ,  $f_3=5$ .

The SRCNN scheme is first used in a training phase with a training dataset for estimating its parameters, and then in a validation phase, with a testing dataset. In the training phase, the network parameters  $\Theta = W_1, W_2, W_3, B_1, B_2, B_3$  are estimated. This is achieved through minimizing the error between the reconstructed images  $F(Y_i; \Theta)$  and original high resolution image  $X$ . The error function  $E$  is given by the mean squared error:

$$E(\Theta) = \frac{1}{n} \sum_{i=1}^n \|F(Y_i; \Theta) - X_i\|^2 \quad (5.4)$$

where  $n$  is the number of training images,  $X_i$  is a set of HR images, and  $Y_i$  is the set of their corresponding LR images [402].

In the testing phase, image quality metrics are used to assess the recovery performance of the HR image for LR cases not included in the training dataset.

### 5.4.2 Very-deep super resolution

To further improve the reconstruction accuracy, a VDSR architecture was evaluated in this work. Deep structured learning [415] is a branch of machine

learning algorithms based on directly learning diverse representations of data. Deep learning has shown superiority over conventional machine learning algorithms in computer vision [399] and speech recognition [416] tasks. Most modern deep learning models are based on NNs. Very deep models used in SISR tasks are usually referred to as VDSR models [417]. The residual learning for CNN was originally proposed to solve the performance degradation problem, i.e., performance gets saturated and then degrades rapidly along with the increase of network depth [418]. The main idea of residual learning lies in that instead of hoping each few stacked layers directly fit a desired underlying mapping, explicitly letting these layers fit a residual mapping would alleviate the degradation problem.

As shown in Fig. 5.3, the VDSR adopted in this work has 20 layers which is consequently much deeper compared with SRCNN which only had 3 layers. As suggested in [419], all kernel sizes are set equal to  $3 \times 3$ . In the SRCNN, the HR image is generated directly from the learned features. In the VDSR, the neural network performs a *residual-learning*, in the sense that the output of the NN is an image which should be added to the original LR image  $Y$  to produce the estimated HR one ( $\hat{X}$ ).

Defining a residual image  $R = Y - X$ , the error function becomes:

$$E(\Theta) = \frac{1}{2} \|R - F_R(Y)\|^2 \quad (5.5)$$

where  $F_R(X)$  is the network prediction of the residual. Thus, the network is learning the residual error between the output (HR image) and input (LR image). The VDSR network used in this work takes the CS recovered images as LR input. More specifically, the original full grid training images are reconstructed by using CS technique with different CRs and using Fourier exponentials as sparsifying basis.

## 5.5 Experimental validation

### 5.5.1 Training and testing of SRCNN and VDSR

It is worth nothing that, in SRCNN, the exact copy of the input has to go through all layers until it reaches the output layer. With many weight layers,

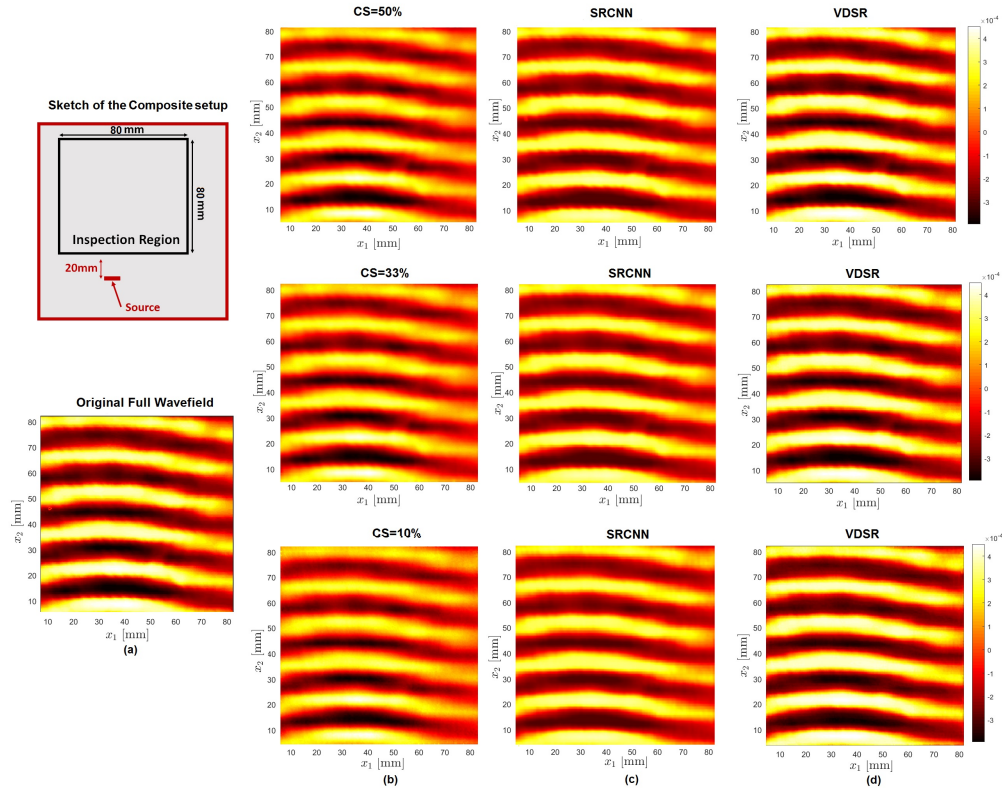


Figure 5.5: Wavefield images recovered for the simple CFRP plate using various methodologies; (a) sketch of the setup and original wavefield image; (b) images recovered uniquely with the CS procedure for CRs: 50%, 33% and 10%; (c) images recovered with the CS and SRCNN; (d) images recovered with the CS and VDSR.

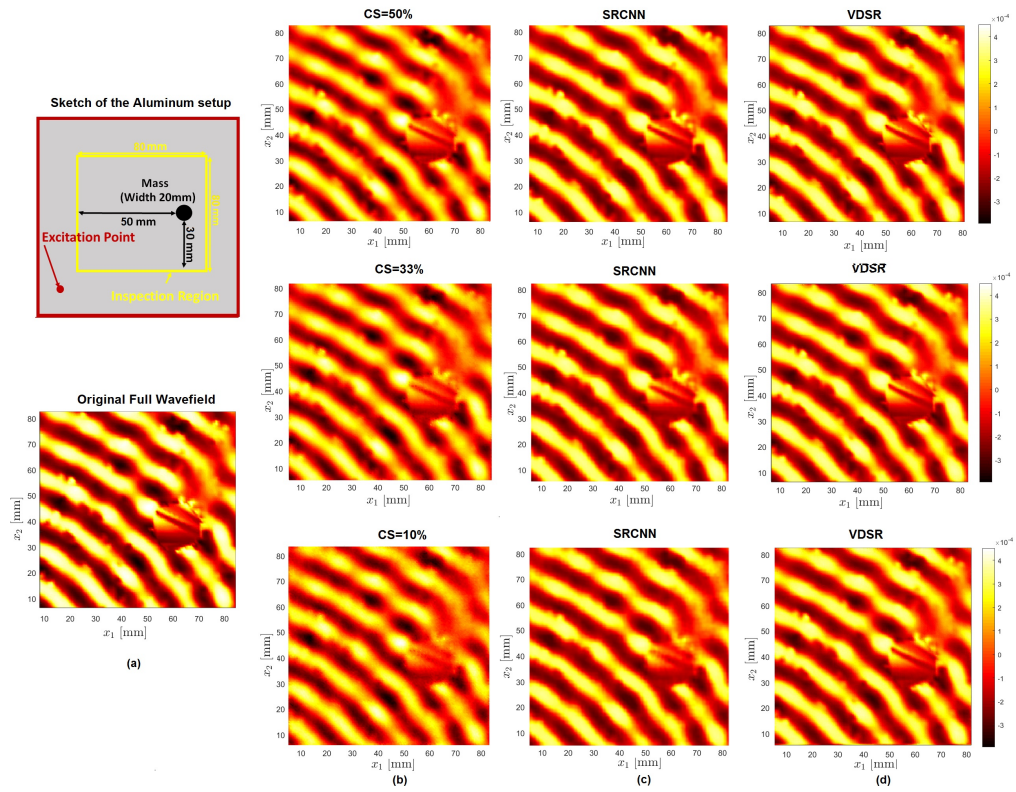


Figure 5.6: Wavefield images recovered for the simple aluminum plate with a clamped mass using various methodologies; (a) The schematic of plate and original wavefield image; (b) images recovered uniquely with the CS procedure for CRs:50%, 33% and 10%; (c) images recovered with the CS and SRCNN; (c) images recovered with the CS and VDSR.

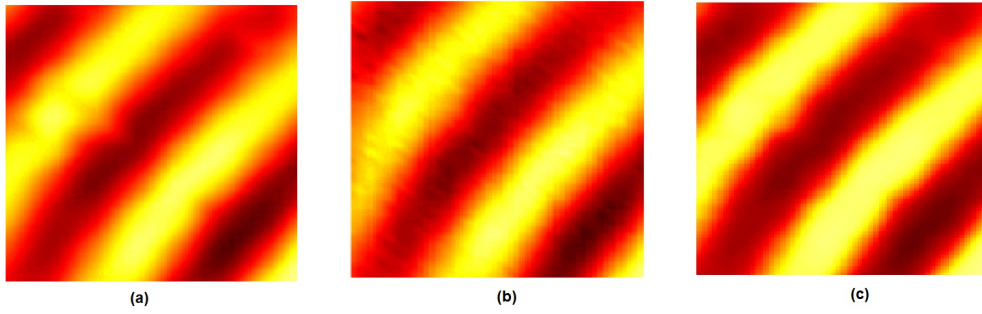


Figure 5.7: (a) HR wavefield image acquired in the simple CFRP plate; (b) CS recovery (CR= 50%); (c) recovered image achieved by combining CS and VDSR.

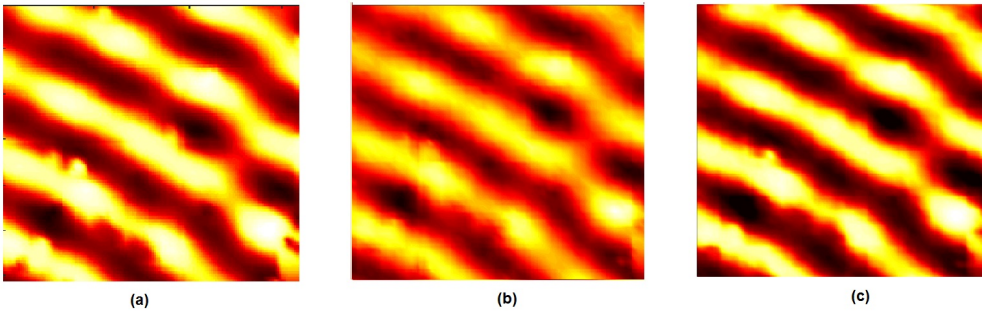


Figure 5.8: (a) HR wavefield image acquired in the simple aluminum plate with a clamped mass; (b) CS recovery (CR= 33%); (c) recovered image achieved by combining CS and VDSR.

this becomes an end-to end relation requiring very long-term memory. For this reason, the vanishing/exploding gradients problem can be critical [420]. VDSR can solve this problem simply with residual learning. In the other word, residual connections are a popular element in convolutional neural network architectures. Using residual improves gradient flow through the network and enables training of deeper networks. In this work, the training of the SRCNN was performed based on the open-source package *Caffe* [421]. Two different training datasets were considered:

- a Non-Wavefield Images or NWI dataset constituted by 652 heterogeneous images including photos of people, animals, cities and more, joining the *General-100* [422], the *91-image* [423], and the *ImageNet* datasets [424];
- and a Wavefield Images or WI dataset, having the same cardinality as the first one, but constituted of actual guided ultrasonic wavefield images (size equal to  $509 \times 509$  pixels.)

Our aim was to show how the type and number of training cases affect the performance of the HR image recovery.

The wavefield images were collected with a SLDV in a large number of different setups and on a dense grid of points to generate HR images. The excitation signal was a sinusoidal burst (central frequency equal to 75kHz) applied to a circular piezoelectric transducer (10 mm in diameter) and bonded on the surface of the plates. Averaging and post-processing procedures were employed to extract displacement images with high signal to noise ratios. Some sample training images are depicted in Fig. 5.4, while materials and geometries of the test structures are reported in Table 5.1. As can be seen, the dataset includes both aluminum (AL) and carbon-fiber reinforced polymer (CFRP) plates, with irregularities such as thickness variations, T-spars and rivets. The material properties of the aluminum plate 7075-T6 alloy are the following:

Density: 2810 kg/m<sup>3</sup> Modulus of elasticity: 71.7 GPa Poisson ratio: 0.33

For the CFRP plate, the properties of the unidirectional lamina (each layer) are listed in Table 5.3.

On the whole, the WI dataset contains 326 cases in which the presence of anomalies was simulated with magnets (20mm in diameter) and 326 cases of undamaged structures.

In the training phase of the SRCNN scheme, the original full wavefield images are subdivided in  $32 \times 32$  pixel sub-images. In total, 177687 sub-images were used in the training phase. The LR samples were generated from the HR ones by applying the CS recovery to subsampled versions of the original images. More specifically, the downsampling was achieved with the jittered method described in [353].

Finally, the wavefield data recovery with VDSR [417] trained using the same wavefield images used for the SRCNN scheme was tested. Differently from SRCNN, VDSR patch size is  $41 \times 41$  pixels, while the batch size is equal to 64. The network was then trained using the MATLAB Deep Learning Toolbox, using the same configuration parameters adopted in [417]. Moreover, gradient clipping was adopted to prevent gradient explosions and speed up the training.

Table 5.2: The results of PSNR using CS and NN methods trained by Non Wavefield Images (NWI) and Wavefield Images (WI), and the results of PSNR using bicubic method trained by Wavefield Images (WI).

HR recovery	CR=50 [%]		CR=33 [%]		CR=10 [%]	
	CFRP	AL	CFRP	AL	CFRP	AL
CS	42.65	43.05	41.40	40.61	35.22	27.88
CS+SRCNN (NWI)	42.97	43.19	41.79	40.63	36.00	29.56
CS+SRCNN (WI)	43.96	43.45	43.42	40.65	36.83	30.22
Bicubic+VDSR (WI)	43.81	42.54	42.17	40.50	36.82	34.36
CS+VDSR (WI)	44.87	45.57	43.50	41.62	37.15	34.60

### Quantitative validation

To quantitatively evaluate the reconstructed super-resolution images, two

types of image quality metrics: (Peak signal-to-noise ratio (PSNR) [425] and structural similarity index (SSIM) [426]) have been computed.

The PSNR is defined as follows:

$$PSNR(x, \hat{x}) = 10 \log \frac{Nmax}{MSE} \quad (5.6)$$

where  $Nmax$  is the maximum pixel value and (MSE) is Mean-Square-Error of the pixels between the original full wavefield image and its reconstruction from the LR observation. A high PSNR value means high quality recovery. Obviously, the maximization of PSNR implies the minimization of MSE as objective function.

The SSIM [426] was used to measure the similarity between the original wavefield and the HR recovered one:

$$SSIM(x, y) = \frac{(2\mu_x\mu_y + c_1)(2\sigma_{xy} + c_2)}{(\mu_x^2 + \mu_y^2 + c_1)(\sigma_x^2 + \sigma_y^2 + c_1)} \quad (5.7)$$

where  $\mu_x$  ,  $\mu_y$  ,  $\sigma_x$  ,  $\sigma_y$  and  $\sigma_{xy}$  are the local means, standard deviations, and cross-covariance for images  $x$  and  $y$ .  $c_1 = (k_1L)^2$  ,  $c_2 = (k_2L)^2$  , and  $L$  are the dynamic range,  $k_1 = 0.01$  , and  $k_2 = 0.03$  .

## 5.6 Results and discussion

In this section, results of the recovery of HR images by means of CS and NN are presented to assess qualitatively and quantitatively the performance of the proposed methodology as a function of CR and NN characteristics. It must be clarified that the images used in this assessment do not belong to the training dataset. In addition, the combination of the conventional Bicubic interpolation with NN was evaluated, to quantify the advantage brought by the adoption of CS schemes.

The qualitative performance of the CS recovery combined with SRCNN and VDSR can be observed in Figs. 5.5 and 5.6 for the two specific test cases of a curved CFRP plate and an aluminum plate, respectively. In particular, it can be observed how the image recovered with the combination of CS and VDSR is very similar to the original HR wavefields in both cases, even



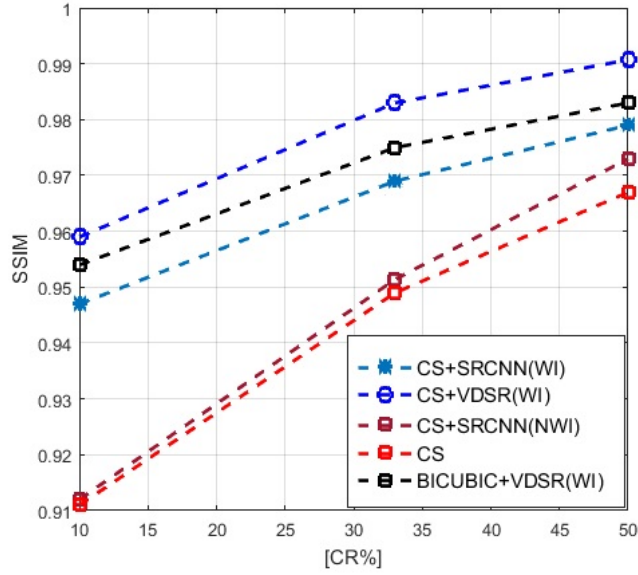


Figure 5.9: Comparison of the SSIM between the training models with WI and NWI datasets and the CS technique for an aluminum plate with CR=10%, 33% and 50%.

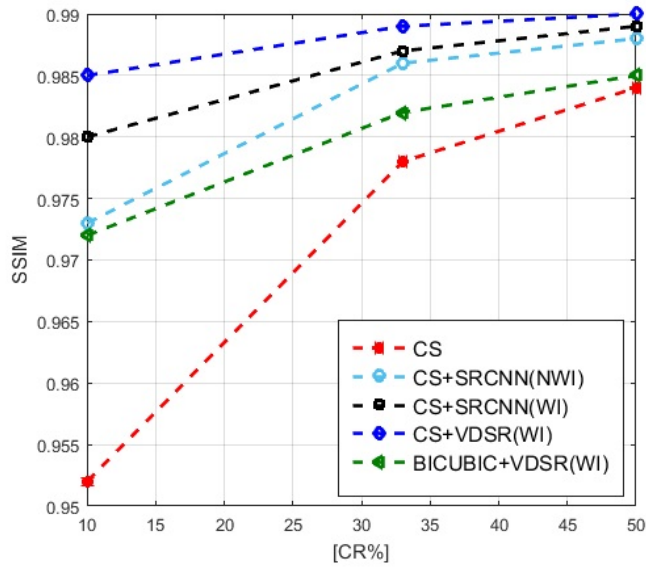


Figure 5.10: Comparison of the SSIM between the training models with WI and NWI datasets and the CS technique for a CFRP plate with CR=10%, 33% and 50%.

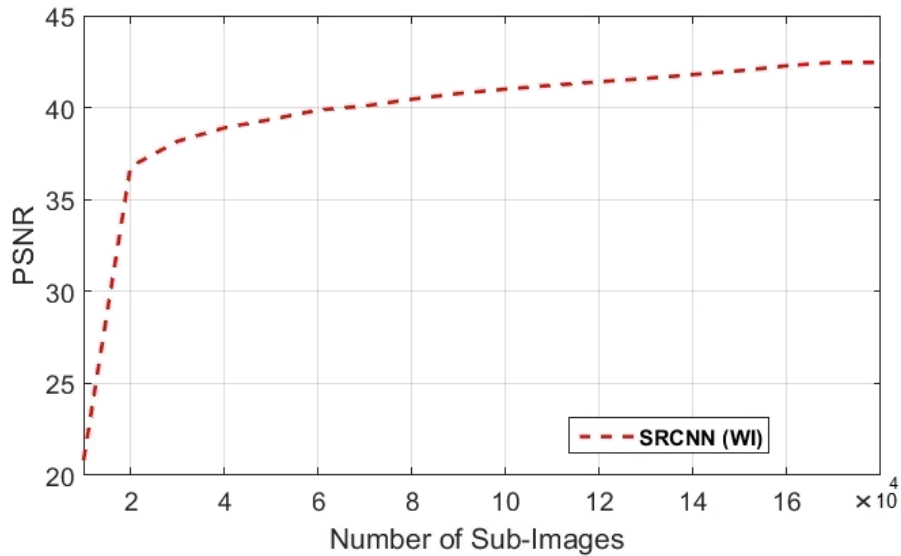


Figure 5.11: Training of SRCNN with the wavefield images (WI) dataset for a curved CFRP plate.

for very low CRs. The improvement with respect to the pure CS recovery is quite evident, especially by focusing on the details, as those shown in Figs. 5.7 and 5.8.

Figs. 5.9 and 5.10 present the comparison in terms of the SSIM achieved with the CS recovery and the training of the SRCNN and VDSR schemes with varying CRs. SSIM values are computed for the wavefield images relative to the aluminum and CFRP plates shown in Figs. 5.5 and 5.6. The results show that the value of SSIM of the recovered wavefield image trained by VDSR network is significantly higher in all the considered cases. Also clearly visible is the beneficial effect brought by the adoption of the WI dataset with respect to the results achieved by using the NWI dataset. Table 5.2 shows that similar trends are obtained by quantifying the effectiveness of the different HR image recovery methods in terms of PSNR. As shown in this Table and in Figs. 5.9 and 5.10, the combination of CS and VDSR(WI) demonstrated a performance superior with respect to all the other combinations (including the Bicubic interpolation with

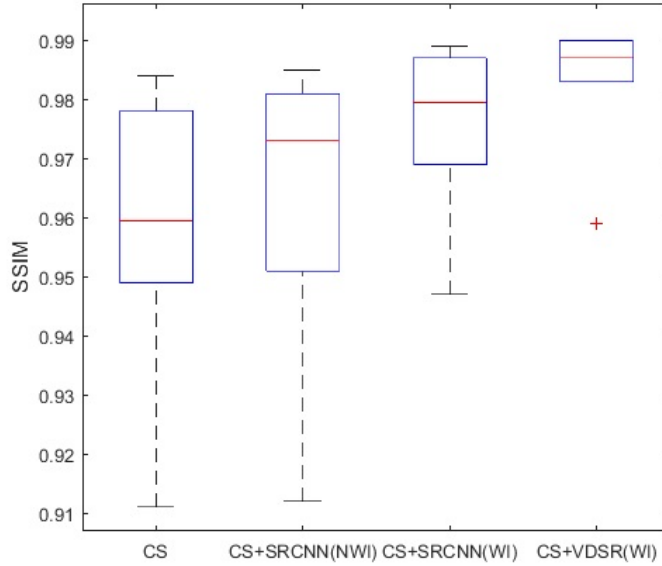


Figure 5.12: Comparison of the SSIM between the CS, the SRCNN scheme, and the VDSR scheme for all the considered cases in the testing dataset with CR=10%, 33% and 50%. In the boxplot representation, the central mark indicates the median, and the bottom and top edges of the box indicate the 25th and 75th percentiles, respectively. The whiskers extend to the most extreme data points.

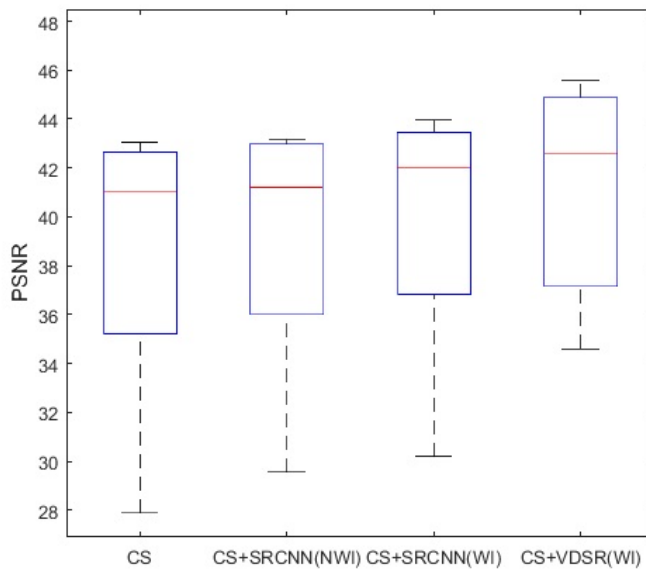


Figure 5.13: Comparison of the PSNR between the CS, the SRCNN scheme, and the VDSR scheme for all the considered cases in the testing dataset with CR=10%, 33% and 50%. In the boxplot representation, the central mark indicates the median, and the bottom and top edges of the box indicate the 25th and 75th percentiles, respectively. The whiskers extend to the most extreme data points.

VDSR(WI)) in all the considered CRs cases for both plates.

To better illustrate the importance of the size of the training dataset in the recovery performance, Fig. 5.11 has reported the PSNR as a function of the dataset cardinality. It can be observed how the cardinality of the dataset improves the performance.

The performance of the different HR image recovery schemes was then quantified on a large testing dataset. As already mentioned, the images used for the evaluation of recovery performances are different from the ones used in the NN training. More specifically, 273 wavefield images, randomly selected among those acquired on the setups shown in Table 5.1, were used for training, quantitative testing and validation. Such images were down-sampled with different CR ratios.

Figs. 5.12 and 5.13 represent the box plot of the SSIM and PSNR in all the considered dataset for: i) CS; ii) SRCNN trained using NWI; iii) SRCNN trained using WI, and VDSR trained using WI. As can be seen, the highest quality HR recovery in terms of SSIM and PSNR is achieved with the VDSR scheme. The mean and the standard error of PSNR of the CS-VDSR (WI) method is 41.21 and 1.65 dB, respectively. This performance is significantly higher than that of the CS-SRCNN (WI) scheme ( $39.75 \pm 2.00$  dB).

From these results, it can be clearly observed that VDSR outperforms SRCNN. This is achieved thanks to the deeper neural network. Besides, residual learning networks, when used in SR tasks, have been proved to possess better visual performance and PSNR performance [427], [428]. It is also worth nothing that, since deep-learning has recently prospered, many new learning-based algorithms can be used in SISR to replace VDSR, such as VGG [417], ResNet [429] and GAN [430].

## 5.7 Discussion

HR wavefield scans convey important information about the health status of the inspected structures. However, the acquisition of these images is typically a slow process. For this reason there is a growing interest in finding solutions for speeding up the measurements. One possible solution

Table 5.3: The properties of the unidirectional lamina for the CFRP plate.

	Properties	Properties	Density
Longitudinal modulus	$E_{11}$	(GPa)	148
Transverse modulus	$E_{22}$	(GPa)	9.5
Out-of-Plane modulus	$E_{33}$	(GPa)	9.5
In-plane shear modulus	$G_{12}$	(GPa)	4.5
Out-of-Plane shear modulus	$G_{13}$	(GPa)	3.17
Out-of-Plane shear modulus	$G_{23}$	(GPa)	3.17
In-plane Poisson's ratio	$V_{12}$	-	0.3
Out-of-Plane Poisson's ratio	$V_{13}$	-	0.4
Out-of-Plane Poisson's ratio	$V_{23}$	-	0.4
Longitudinal tensile strength	$X_T$	(MPa)	2000
Longitudinal compressive strength	$X_C$	(MPa)	1500
Transverse tensile strength	$Y_T$	(MPa)	50
Transverse compressive strength	$Y_C$	(MPa)	150
Out-of-Plane tensile strength	$Z_T$	(MPa)	100
Out-of-Plane compressive strength	$Z_C$	(MPa)	253
In-Plane shear strength	$S_{12}$	(MPa)	150
Out-of-Plane shear strength	$S_{13}$	(MPa)	41.5
Out-of-Plane shear strength	$S_{23}$	(MPa)	41.5

is based on the reduction of the number of scan points and on the subsequent recovery of the HR image by means of CS procedures. Unfortunately, the quality of this reconstruction method degrades rapidly as the reduction of the scan points becomes more consistent. To counteract this degradation, this dissertation, investigated the use of SR techniques based on the training of NNs. In particular, two main findings were demonstrated:

- The training should be performed based on a sufficiently large and comprehensive dataset of wavefield images rather than recurring to conventional image datasets.
- Deep networks have clearly superior performance with respect to shallow neural networks.

Experimental results demonstrate that the proposed methodology can be applied in a variety of structural components to reduce acquisition time and achieve high similarity to the HR images, even when just the 10% of the original scan points remain. It is worth noting that the definition of resolution is based on pixel values, and the aim is to reconstruct the signals so that they are very similar to the wavefield acquired on the dense grid. In addition, the resolution of the final defect identification needs further experiments.

Future work will investigate: i) The possibility to apply the CS algorithm to raw SLDV data (without averaging); ii) the possibility to exploit this imaging methodology to characterize defects; iii) alternative Deep Learning architectures; iv) the benefit brought by further increasing the number of wavefield images in the training phase with different setups or excitation frequencies. Indeed, it is a well-known fact that deep learning strongly benefits from training on big data. Moreover, the results need to be confirmed in additional cases in order to have a better assessment of the performance, given the vast number of applications which can be targeted by this inspection method.

# Chapter 6

## CS and Damage Imaging

### 6.1 Summary

Ultrasonic wavefield imaging techniques are typically applied to full acoustic wavefield data acquired over the area of the structure to be inspected. Such techniques can be very useful but present also some limitations, including slow data acquisition and lack of accuracy. This chapter investigates how the Compressive Sensing approach, which speeds up the acquisition process through a random spatial undersampling, can be used in conjunction with damage imaging methods to perform the characterization of the inspected medium. Two novel analysis tools to process recovered wavefield data are presented and compared to widely adopted damage imaging algorithms, namely the local Wavenumber Estimation technique [53] and the Cumulative Kinetic Energy [54].

The first tool<sup>1</sup> is based on the fact that, as discussed in Chapter 4, the compressive sensing recovery performances are dependent on the selection of the measurement method (i.e. the subsampling scheme) and on the sparsifying representation basis. However, the sparsity of the coefficients is influenced by the presence of defects. In fact, defects usually cause mode conversion and incoherent scattering. When the sparsity prerequisite is

---

<sup>1</sup>The first wavefield analysis tool was presented in *Full Wavefield Analysis and Damage Imaging Through Compressive Sensing in Lamb Wave Inspections*, Keshmiri et al.

lost, the wavefield recovery can be imprecise and strongly dependent on the reconstruction basis selected. It will be shown that this limitation can be turned into a mean to detect the presence of defects.

The second proposed strategy is based on the removal of the injected wave from the overall response, in order to highlight the presence of reflections associated with damage. This strategy is based on the application of the 3D discrete Fourier transform (3DFT) to the CS reconstructed wavefields to produce the frequency-wavenumber representation. The frequency-wavenumber coefficients are then thresholded, and, finally, a Laplacian filter is applied to enhance the discontinuities.

These concepts were tested over multiple experiments<sup>2</sup> related to different setups, including aluminium, composite and epoxy structures to illustrate the pros and cons of the different damage modalities. The results illustrate that the combined use of wavefield imaging and compressive sensing provides sufficient information to non-destructively evaluate the structural integrity in many situations of interest even for very low compression ratios (CRs). Moreover, the application of these processing procedures minimizes artifacts and small-scale noise without significant loss of accuracy in the damage detection.

## 6.2 Materials and methods

Three main datasets have been used for the evaluation of the damage imaging methods:

- Numerically simulated wavefields were included in the analysis. In particular, a simulation of a 1 mm-thick aluminum plate ( $400 \times 400 \text{ mm}^2$  wide) was performed. A piezoelectric excitation at the center of the plate was modeled using 3D solid spectral elements with six nodes in the  $x_1$  and  $x_2$  directions and three nodes in the  $z$ - direction per element distributed according to the Gauss-Lobatto-Legendre

---

<sup>2</sup>The experiments were conducted thanks to a collaboration between the Polish Academy of Science (M. Radzienski, P. Kudela, and Prof. W. M. Ostachowicz) and the University of Bologna in the framework of the HARMONIA project (UMO-2012/06/M/ST8/00414).



rule. A convergent mesh at the maximum frequency of interest was adopted. The excitation was in the form of a sinusoidal tone burst. One notch of 10 mm length was modeled by a 0.1 mm separation of appropriate nodes of the kissing spectral elements. The out-of-plane surface displacements on the opposite side of the plate with respect to the transducer were considered. The nodal displacements of the finite spectral element model were mapped into a regular grid of  $500 \times 500$  points by linear interpolation and further used for signal processing.

- The second dataset was obtained by using a scanning laser Doppler vibrometer Polytec PSV400M2 SLDV (Polytec GmbH, Waldbronn, Germany). Guided waves propagating in a glass fiber reinforced polymer (GFRP) plate (4 unidirectional glass fiber layers oriented along the  $x$ -axis, overall thickness equal to 3.2 mm) were recorded. A notch cut 15-mm long, 0.5 mm wide and 70% of the specimen thickness deep, was machined by a sharp tool. The excitation signal was generated by an arbitrary waveform generator, amplified to 400 Vpp by a dedicated amplifier. The excitation signal was applied to a round piezoelectric transducer (10 mm in diameter) bonded at the center of the plate. Out-of-plane displacements were registered by the SLDV on a dense grid of  $385 \times 389$  equally spaced (1 mm) points.

Moreover, the SLDV was used to acquire the guided waves propagating in a 0.5 mm thick carbon-fiber-reinforced (CFRP) plate ( $500 \times 500$  mm wide). In this case, delamination was thermally induced on the plate. A 10 mm diameter piezoelectric transducer was used to excite the guided waves field in the structure, whereas the plate response was recorded on a grid of  $277 \times 279$  equispaced points. In the experimental data, both S0 and A0 modes were excited but A0 mode had much greater amplitude than S0 mode.

- The third dataset was acquired with a measurement system which consists of the following elements: i) a piezoelectric transducer bonded to the inspected structure for the generation of guided waves; ii) an air-coupled probe mounted on a CNC machine and connected to an oscilloscope for the guided waves wavefield detection; iii) an arbitrary

function generator to drive the piezoelectric transducer (a sinusoidal burst with Gaussian modulated envelope was used), iv) a PC to control the CNC machine, and store and process the data. A sketch of the setup adopted for ultrasonic wavefield measurement is shown in Fig. 6.1.

Multiple plates were inspected with this setup. The first one was constituted by a 3 mm-thick epoxy glass ( $50 \times 50$  cm wide). The second one was a 3 mm-thick composite (CFRP) plate ( $50 \times 50$  cm wide) and the third case study considers guided waves propagating in a sandwich-type panel constitute by the top and bottom aluminium surface plates and an inner honeycomb core. The latest plate measured  $500 \times 500 \times 7$  mm. The presence of defects was simulated with a bonded mass placed in different positions, and GWs were generated by exciting the transducer with a 40 kHz frequency. Compressed wavefield data was recorded in a region surrounding the mass using the air couple probe mounted on the CNC machine.

### 6.2.1 Cumulative kinetic Energy

The simplest possible approach for analyzing the wavefield data is to compute the cumulated kinetic energy (CKED). More specifically, the local energy is calculated by computing the squared sum of each measurement over time:

$$CKED_{s_x}(x_1, x_2) = \frac{1}{2} \sum_{k=1}^K (s_x(x_1, x_2)[k])^2 \quad (6.1)$$

Indeed,  $CKED_{s_x}(x_1, x_2)$  is the energy of the signal  $s_x(x_1, x_2)$  in a point defined by the  $x_1$  and  $x_2$  coordinates and in a generic time interval defined by the time samples  $[1, K]$ . The CKED (or its squared root, the RMS value) applied to the full wavefield images has been used as a tool for damage localization and visualization by many authors [13, 54, 139, 146].

The CKED algorithm was applied to the datasets related to the plate-like components schematized in Figs. 6.2(a-c).

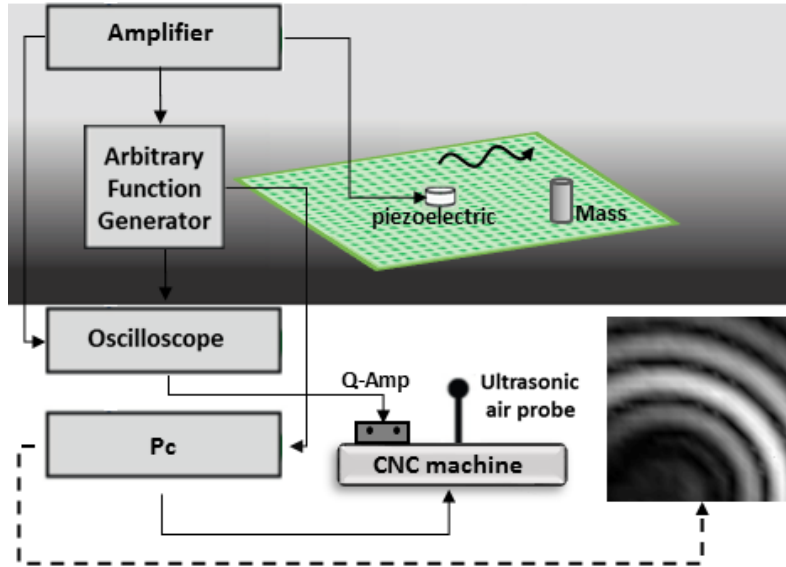


Figure 6.1: Sketch of the experimental setup using air probe and CNC machine.

For validation purposes, the sampling process is firstly done according to the Shannon-Nyquist theorem in the spatial ( $x_1 - x_2$ ) and in the temporal domain, then downsampled and finally recovered with the CS procedure. Figs. 6.2 (d-f) show some sample snapshots of the propagating waves interacting with the defects.

Fig. 6.3 depicts the CKED of three wavefield signals. It is worth noting that high energy guided wave signals are evident in correspondence to the defect locations. However, in all the considered cases, the defect is barely distinguishable from image artifacts. In particular, in the aluminum case where the defect is oriented perpendicularly to the incident wavefront, and consequently a relatively weak scattering occurs, the defect is almost invisible from the full wavefield observation.

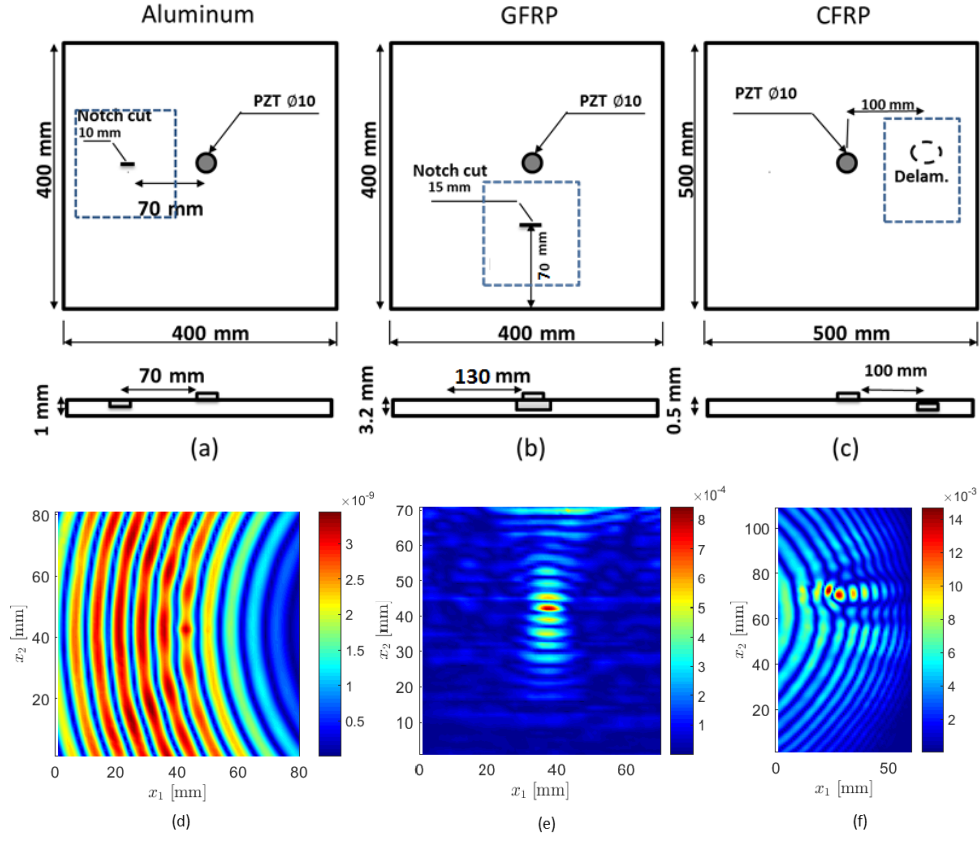


Figure 6.2: Sketch of the three (numerical and SLDV) setups (a, b, c), the dashed lines are the perimeters of the imaged areas. Snapshots of the full measured wavefield at  $t = 66 \mu s$ ,  $t = 53 \mu s$  and  $t = 89 \mu s$  for the aluminum plate with numerical data, GFRP and CFRP plates with experimental data, (d, e, and f), respectively.

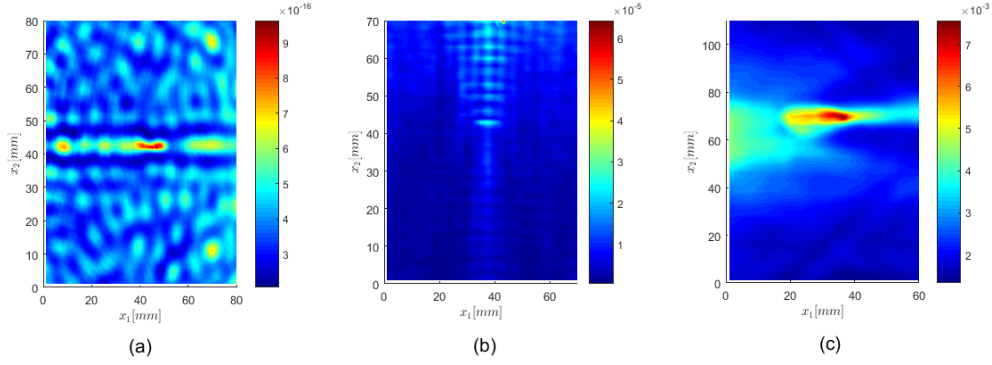


Figure 6.3: CKED computed on the full wavefield signals acquired on the aluminum (a), GFRP (b) and CFRP (c) plates, respectively. The considered time interval is equal to  $512 \mu s$  for the aluminum,  $512 \mu s$  for the GFRP plate, and  $1024 \mu s$  for the CFRP plate. The time window was selected in order to capture the most energetic portion of the wavefield after actuation. After a certain time, due to dissipation, the energy drops to a negligible level and the wavefield samples can be discarded.

### 6.2.2 Differential CS Recovery for Damage Imaging

This damage imaging method was conceived starting from the observation that, despite the good average performance, the CS recovery applied to acoustic wavefield measurements is far from being perfect in correspondence to structural defects. In fact, modal conversion and incoherent scattering occur where defects are located, and such phenomena cannot be represented sparsely in the considered decomposition bases. In this sense, the limitation in the CS recovery can be turned into a mean to detect the presence of defects. Indeed, the proposed approach is based on the computation of the CKED of the difference between the waveforms recovered with two different representation bases B1 and B2 ( $s_x(x_1, x_2)[k] = s_{B1}(x_1, x_2)[k] - s_{B2}(x_1, x_2)[k]$ ), where  $k$  is the index of a given time sample.

In the three cases analyzed in the previous Section, for an assumed CR, the Jittered subsampling strategy described in the previous Chapters was applied, then the signals on the Nyquist Shannon grid were recovered by

using the different reconstruction bases and, finally, the CKED quantity related to the difference signals was computed. The experiments were repeated multiple times, with a different number of iterations of the SPGL1 algorithm. To quantitatively evaluate the recovery and damage imaging procedure the signal to (reconstruction-) noise ratio (SRNR) was computed:

$$SRNR = \frac{\|s_{B1}(x_1, x_2)[k]\|}{\|s_{B2}(x_1, x_2)[k] - s_{B1}(x_1, x_2)[k]\|} \quad (6.2)$$

where  $s_{Bx}$  is the recovered wave field signal obtained by exploiting the sparsifying representation basis  $Bx$ . Such quantity was computed both for the whole imaged area (W) and in the subregions corresponding to the damage locations (D).

Moreover, the Contrast-to-noise ratio (CNR) was used as a metric to assess the damage image quality. CNR is defined as:

$$CNR = \frac{mean_D[CKED_{s_x}] - mean_{W-D}[CKED_{s_x}]}{std_W[CKED_{s_x}]} \quad (6.3)$$

where  $CKED_{s(x)}$  is computed as in Eq. (6.1),  $mean_X[...]$  and  $std_X[...]$  are the spatial mean and standard deviation computed in the imaged area  $X$ . More specifically, I have considered the non-damage (background, W-D) and the damage areas (D), respectively, where W are the whole imaged areas indicated by the dashed lines in Figs. 6.2(a,b,c), whereas the damaged subregions (label D) have dimensions equal to  $33 \text{ mm}^2$  for the Al and GFRP plates, and to  $266 \text{ mm}^2$  for the CFRP plate.

Tables 6.1, 6.2 and 6.3 show the SRNRs for different sparsifying basis, different subsampling ratios (50%, 33% and 20% of retained scan points) and different number of iterations for both the whole imaged areas (label W) and the damaged subregions (label D).

The implemented procedure was applied to the numerical simulation of the aluminum plate, and it can be observed from the results reported in Table 6.1, that the SRNR reaches the maximum value after about 30 iterations when using the 2DFT and 3DFT as a sparse representation basis (CR= 50%). However, a noteworthy degradation (-9 dB) occurs when I circumscribe the SRNR calculation to the defective area.

Table 6.1: SRNR for wavefields obtained in the aluminum plate (undamaged and damaged regions).

	SRNR (50%) [dB]				SRNR (33%) [dB]				SRNR (20%) [dB]			
	it=30		it=90		it=30		it=90		it=30		it=90	
B1-B2	W	D	W	D	W	D	W	D	W	D	W	D
2DF-3DF	56.8	<b>47.5</b>	56.5	<b>40.9</b>	45.0	<b>45.0</b>	43.9	<b>38.1</b>	34.5	<b>33.6</b>	33.1	<b>30.4</b>
2DF-2DW	35.2	<b>31.5</b>	53.6	<b>49.6</b>	33.7	<b>31.6</b>	43.0	<b>35.8</b>	29.5	<b>29.2</b>	32.9	<b>31.0</b>
2DF-2DC	24.8	<b>21.8</b>	41.8	<b>38.5</b>	23.1	<b>20.0</b>	34.6	<b>33.4</b>	20.2	<b>17.4</b>	27.2	<b>26.2</b>
2DC-2DW	24.5	<b>22.8</b>	42.3	<b>38.9</b>	23.9	<b>21.4</b>	35.7	<b>32.8</b>	19.5	<b>18.3</b>	27.4	<b>25.3</b>

Table 6.2: SRNR for wavefields obtained in the GFRP plate (undamaged and damaged regions).

	SRNR (50%) [dB]				SRNR (33%) [dB]				SRNR (20%) [dB]			
	it=30		it=90		it=30		it=90		it=30		it=90	
B1-B2	W	D	W	D	W	D	W	D	W	D	W	D
2DF-3DF	36.8	<b>23.0</b>	36.3	<b>28.8</b>	30.3	<b>21.9</b>	29.1	<b>18.8</b>	24.6	<b>24.3</b>	23.0	<b>22.8</b>
2DF-2DW	30.8	<b>22.5</b>	39.8	<b>27.0</b>	27.4	<b>22.0</b>	28.8	<b>20.0</b>	21.1	<b>16.8</b>	20.9	<b>16.5</b>
2DF-2DC	23.4	<b>22.3</b>	36.8	<b>28.8</b>	15.4	<b>12.7</b>	22.6	<b>16.6</b>	6.6	<b>4.5</b>	10.0	<b>6.7</b>
2DC-2DW	24.7	<b>19.4</b>	39.5	<b>28.5</b>	16.2	<b>11.9</b>	23.0	<b>15.7</b>	7.3	<b>3.8</b>	10.5	<b>6.6</b>

Table 6.3: SRNR for wavefields obtained in the CFRP plate (undamaged and damaged regions).

	SRNR (50%) [dB]				SRNR (33%) [dB]				SRNR (20%) [dB]			
	it=30		it=90		it=30		it=90		it=30		it=90	
B1-B2	W	D	W	D	W	D	W	D	W	D	W	D
2DF-3DF	53.8	<b>48.1</b>	52.0	<b>46.4</b>	40.1	<b>38.2</b>	39.4	<b>36.0</b>	23.8	<b>19.1</b>	23.8	<b>21.3</b>
2DF-2DW	33.5	<b>30.0</b>	51.0	<b>43.9</b>	32.6	<b>25.3</b>	39.0	<b>28.9</b>	23.9	<b>18.8</b>	25.2	<b>19.9</b>
2DF-2DC	35.2	<b>31.8</b>	49.9	<b>37.5</b>	31.9	<b>24.7</b>	38.4	<b>27.1</b>	22.9	<b>16.2</b>	24.7	<b>17.3</b>
2DC-2DW	32.6	<b>30.8</b>	52.0	<b>43.3</b>	31.1	<b>26.0</b>	41.3	<b>25.2</b>	25.0	<b>17.2</b>	29.0	<b>17.0</b>

Table 6.4: CNR for wavefields obtained in the aluminum plate, ( $\text{CNR}_r = 10.93\text{dB}$ ).

	CNR (50%) [dB]		CNR (33%) [dB]		CNR (20%) [dB]	
	it=30	it= 90	it=30	it=90	it=30	it=90
B1-B2						
2DFT-3DFT	17.71	23.42	11.33	16.46	6.09	14.54
2DFT-2DWA	11.15	13.54	7.89	14.62	4.27	9.10
2DFT-2DCT	7.30	7.73	6.17	6.87	3.87	5.62
2DCT-2DWA	5.66	7.53	3.71	7.07	3.43	6.70

Table 6.5: CNR for wavefields obtained in the GFRP plate, ( $\text{CNR}_r = 2.69\text{dB}$ ).

	CNR (50%) [dB]		CNR (33%) [dB]		CNR (20%) [dB]	
	it=30	it= 90	it=30	it=90	it=30	it=90
B1-B2						
2DFT-3DFT	9.24	9.44	6.14	6.98	0.05	0.10
2DFT-2DWA	9.84	12.04	3.37	4.15	0.59	1.39
2DFT-2DCT	6.05	6.21	1.63	2.41	0.16	0.19
2DCT-2DWA	4.77	7.65	1.60	2.33	0.15	0.17

Table 6.6: CNR for wavefields obtained in the CFRP plate, ( $\text{CNR}_r = 6.18\text{dB}$ ).

	CNR (50%) [dB]		CNR (33%) [dB]		CNR (20%) [dB]	
	it=30	it= 90	it=30	it=90	it=30	it=90
B1-B <sub>2</sub>						
2DFT-3DFT	9.62	10.07	5.04	7.29	4.45	4.69
2DFT-2DWA	7.98	8.61	5.00	5.24	4.22	4.44
2DFT-2DCT	9.76	10.90	5.70	5.40	4.25	6.32
2DCT-2DWA	4.38	5.15	4.69	5.14	3.58	3.31



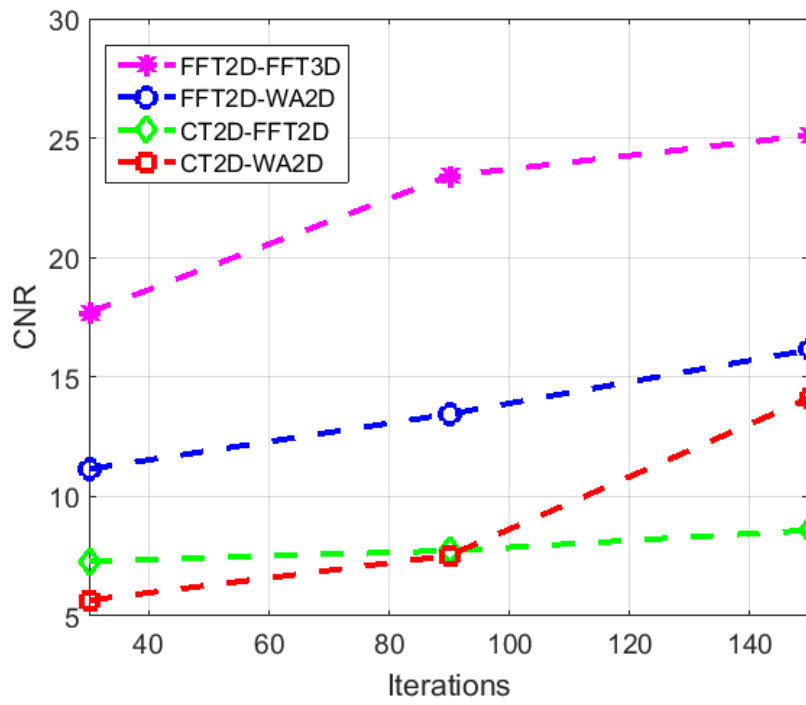


Figure 6.4: Wavefield imaging performances in terms of CNR for the aluminum plate for 50% of downsamples.

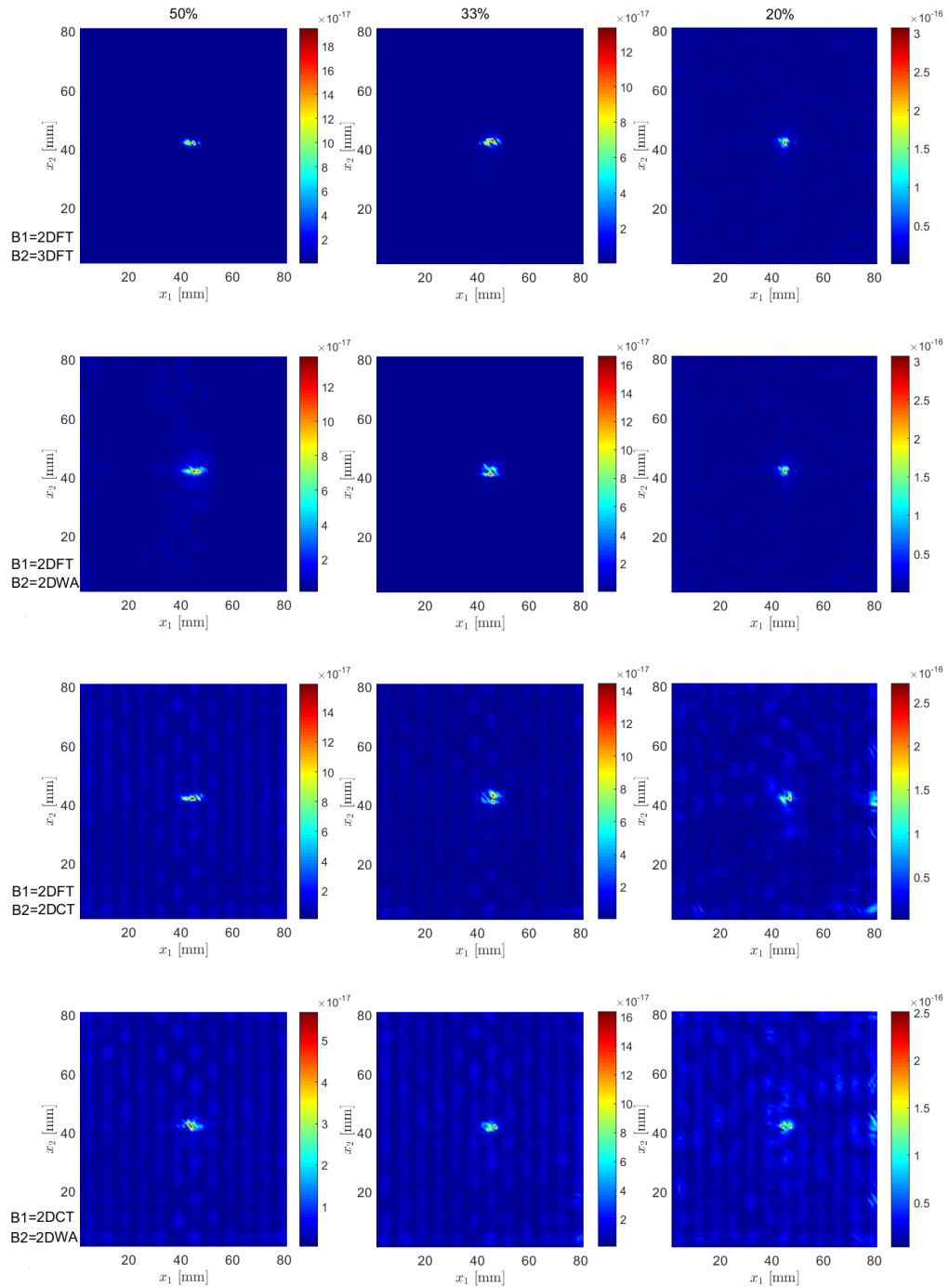


Figure 6.5: CKED damage influence maps based on the simulated wavefield signals (aluminum plate). The results related to different reconstruction bases and different subsampling factors with 90 iterations are presented. On the figures of 2DFT-2DCT and 2DCT-2DWA, artifacts might be caused by a recovery error in the CS procedure.

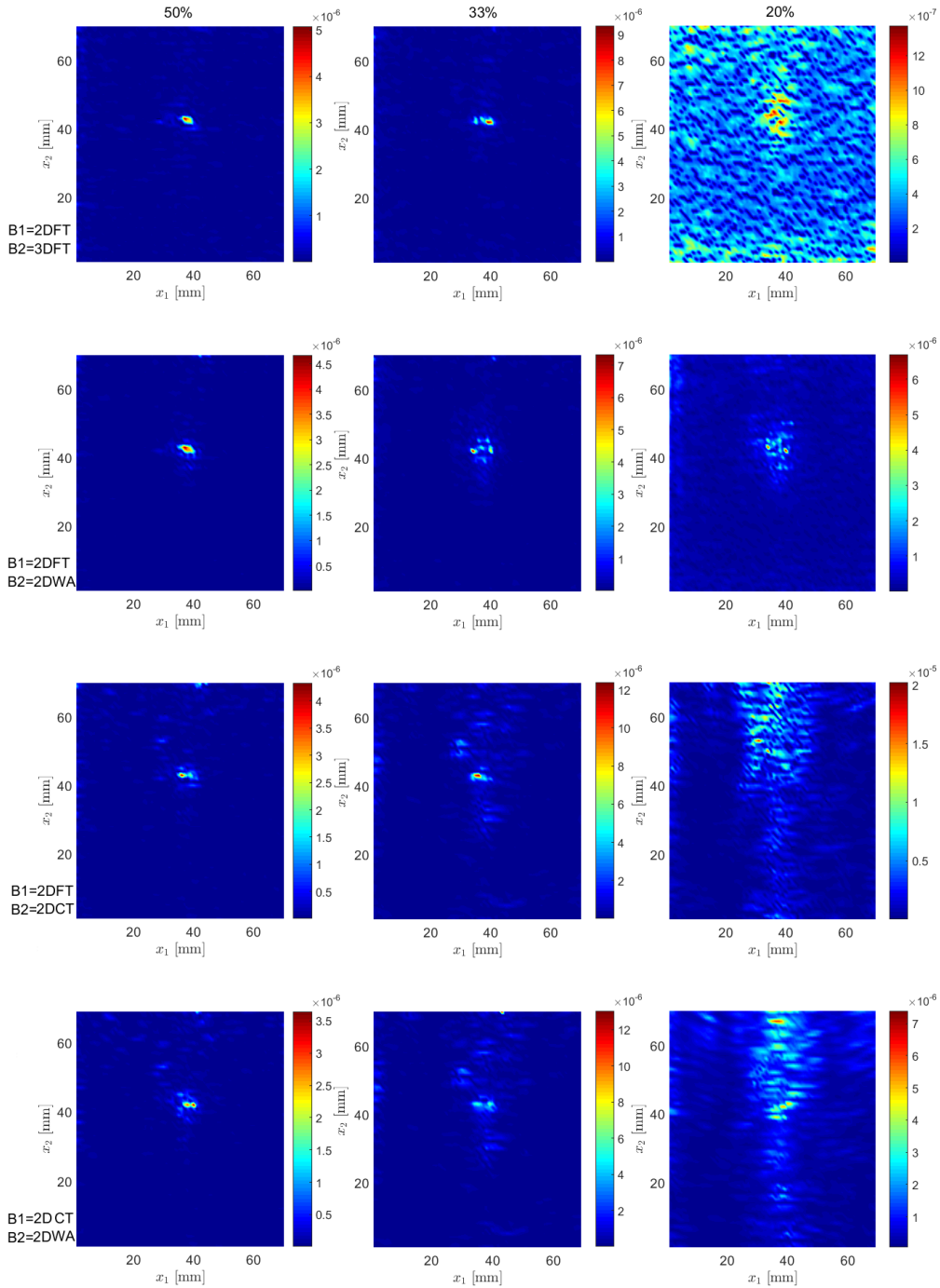


Figure 6.6: CKED damage influence maps based on the wavefield signals acquired with the SLDV on the GFRP plate. The results related to different reconstruction bases and different subsampling factors with 90 iterations are presented.

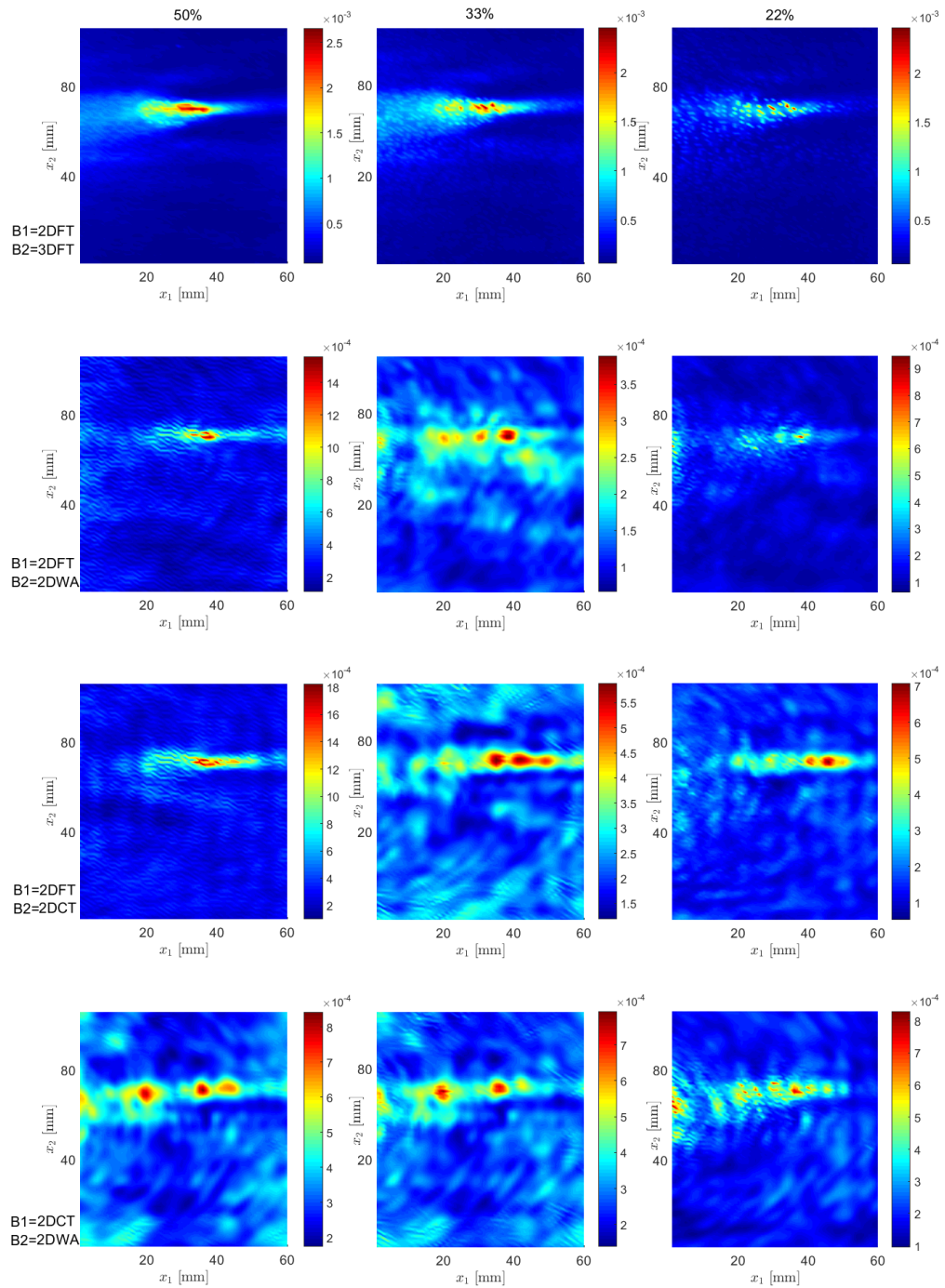


Figure 6.7: CKED damage influence maps based on the wavefield signals acquired with the SLDV on the CFRP plate. The results related to different reconstruction bases and different subsampling factors with 90 iterations are presented.

These results confirm the heuristic evaluated in this work, i.e. the defective region cannot be represented sparsely and consequently the compressive sensing procedures outputs recovered wavefields which are influenced by the adopted representation basis.

Furthermore, it can be observed that, when Curvelet and Wave-Atoms are adopted as sparse representation bases, the values of SRNR decrease and a greater number of iterations is necessary to maximize such quantities. Moreover, the experiments proved that decreasing the CR led to an increase of the error in the wavefield reconstruction for reduced numbers of iterations.

Tables 6.4, 6.5 and 6.6 show the CNRs results for the cases of 50%, 33% and 20% of retained scan points and the three different plates. Moreover, the reference CNR ( $CNR_r$ ) was computed on the original full wavefield signals to assess the damage image quality.

For example, it can be noticed that the high CNR value (17.71 dB) reported in Table 6.4 for the case of 50% retained scan points (and 30 iterations) clearly confirms that the defective area is better highlighted by the proposed procedure with respect to what can be achieved by computing the CKED on the original signal ( $CNR_r = 10.93$ ). Similar improvements are achieved for the GFRP and CFRP plates.

In Fig. 6.4, for the aluminum plate case, the results of the implemented procedure are shown in terms of CNR versus the number of iterations. In all cases, the quality of the wavefield imaging reaches its maximum value for the maximum number of iterations considered.

Taking into account the recovery times discussed in Chapter 4, it can be concluded that the best trade-off between CNR and recovery times is offered by the differential recovery performed with 2DFT and 3DFT bases which provides high CNRs, with relatively few iterations and, consequently, very fast processing.

The effect of the proposed processing can be qualitatively evaluated in Figs. 6.5, 6.6, and 6.7, where the CKED maps related to the considered setups and multiple settings of the algorithm are shown. It is worth noting that there is a substantial agreement between the CNRs values reported in Tables 6.4, 6.5, 6.6, and the quality of the damage images: higher CNRs values correspond to a better quality of the wavefield imaging in the localization of the defective region.

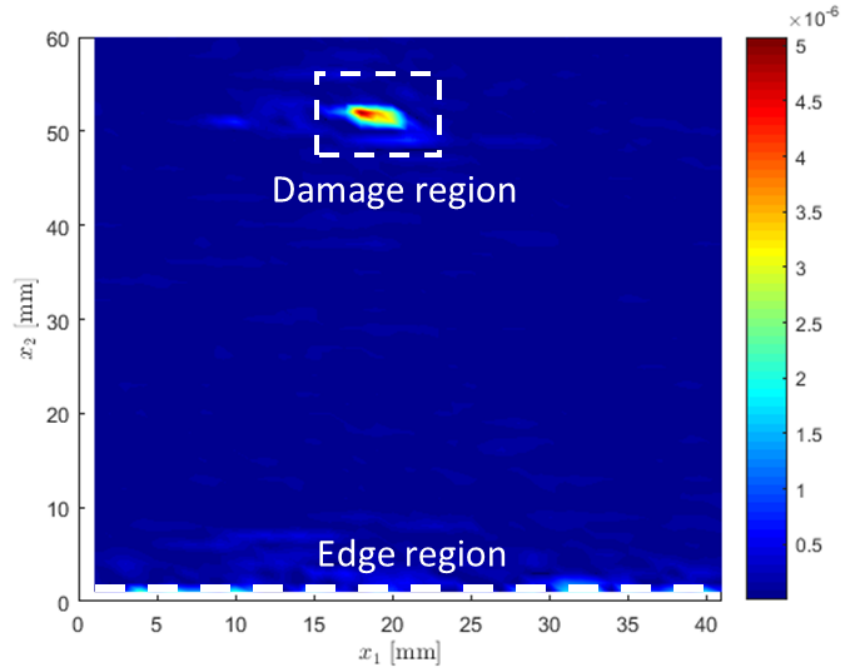


Figure 6.8: Damage map related to an area which includes edge reflections: GFRP plate (B1= FFT2D, B2=FFT3D, 50% downsampling).

Finally, the algorithm was tested also on areas close to the edge of the plates to verify that edge reflections are clearly distinguishable from the anomalous scattering induced by defects. The results supporting such assumption are shown in Fig. 6.8.

### 6.2.3 Local Wavenumber estimation

The local wavenumber estimation technique (LW) method was applied to experimental wavefield data to characterize damages in the plate like structures [53]. The local wavenumber method can be implemented by applying a three-dimensional Fourier transform (3D FFT) to convert the wavefield in the frequency wavenumber domain where multiple propagating

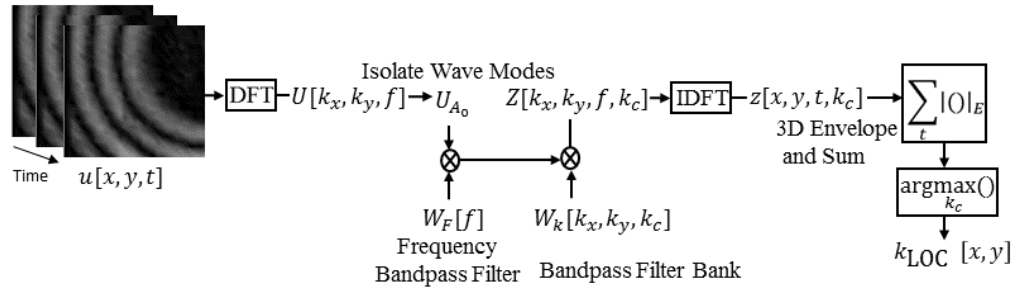


Figure 6.9: Diagram of local wavenumber estimation process.

modes can be isolated. Then, the signal is bandpass filtered using a frequency-domain Gaussian-shaped window. An additional filter bank is applied to isolate multiple narrowband wavenumber components. In the next step, each narrowband component is transformed back in the spatial and temporal domain and an envelope signal is calculated in the spatial grid. Finally, the damage is visualized by plotting the central wavenumber of the subcomponent that maximizes the amplitude of the spatial envelope, as schematically depicted in Fig. 6.9.

### 6.2.4 Laplacian filtering

In this section, a wavefield imaging method based on Laplacian filtering is presented. The application of these filters minimizes artifacts and small-scale noise without significant loss of accuracy in the damage detection. The effectiveness of the proposed approach is demonstrated through experimental results obtained from compressed wavefield data acquired with air-coupled probes. The reconstructed ultrasonic responses are subsequently processed to produce damage images. The quantitative and qualitative assessment of such images prove that the proposed method provides reliable results even for very low compression ratios (CRs).

The implemented damage imaging method is based on the 3D discrete Fourier transform (DFT) that is applied to the acquired wavefield signal to produce the frequency wavenumber representation  $w(x, y, t)$ .

$$W(K_x, K_y, \omega) = F_{3D}(w(x, y, t)), \quad (6.4)$$

where  $F_{3D}$  is the Fourier transform operator. A cosine tapered windowing with 10% taper width across the spatial and temporal dimensions was applied preliminarily to the acquired data in order to avoid truncation effects. The frequency-wavenumber representation is then thresholded <sup>3</sup>:

$$M(K_x, K_y, \omega) = \begin{cases} 0 & \text{if } W(K_x, K_y, \omega) < \textit{threshold} \\ 1 & \textit{otherwise}, \end{cases} \quad (6.5)$$

$\hat{W}(K_x, K_y, \omega)$  is the output of the masking procedure:

$$\hat{W}(K_x, K_y, \omega) = W(K_x, K_y, \omega)M(K_x, K_y, \omega), \quad (6.6)$$

In addition, a Laplacian filter is applied to enhance the discontinuities. More specifically, the following quantity is computed:

$$\nabla W = \frac{\partial^2 w}{\partial k_x^2} + \frac{\partial w^2}{\partial k_x^2} \quad (6.7)$$

Such quantity is then transformed back into the spatial and temporal domain via inverse Fourier transform:

$$\tilde{w}(x, y, t) = F_{3D}^{-1}(\nabla \hat{W}(K_x, K_y, \omega)) \quad (6.8)$$

Finally the CKED(x,y) of the processed data is computed.

The dataset collected with the air coupled probes (aluminum plate) was used to test the performance of the Laplacian filter processing. Fig. 6.10 illustrates the effectiveness of the damage imaging process for different positions of the mass and different distances from the source. In particular, Figs. 6.10 (a,b,c) show different snapshots, while different damage identification results are shown in Figs. 6.10 (d,e and f).

Fig. 6.11 (a) depicts an original wavefield (top row: CR= 33% and bottom row: CR=10%) acquired by an air-coupled probe in the aluminum

---

<sup>3</sup>The threshold is set as a given percentage of the maximum of the absolute value of the data in the wavenumber domain.



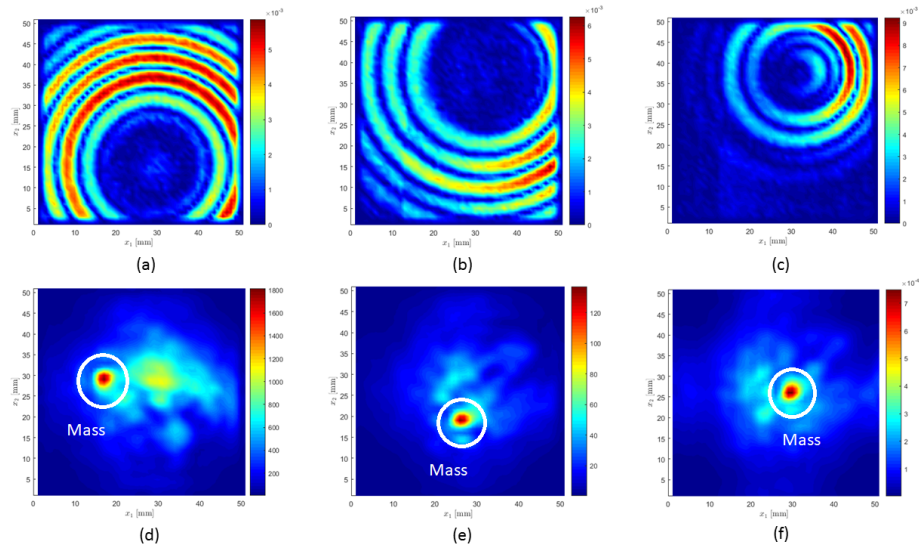


Figure 6.10: Snapshots of the reconstructed wavefields at different times and mass positions (a,b,c), and results of the Laplacian Filtering procedures (d,e and f). The damage images peak in correspondence to the actual mass positions.

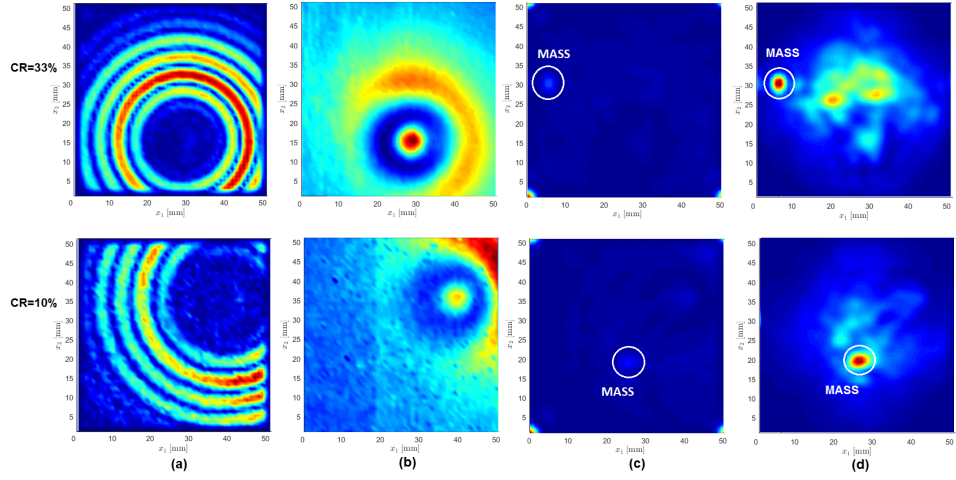


Figure 6.11: Snapshot of the wavefield acquired in the aluminum plate with air-coupled probe (a), CKED of the signal (b), CKED of the signal after wavenumber-filtering (c), damage map after Laplacian filtering (d) with CR=33% (top row) and CR=10% (bottom row).

plate. Fig. 6.11 (b) illustrates the cumulative kinetic energy of the wavefield. In this case, the defect is barely distinguishable from image artifacts. Fig. 6.11(c) illustrates the effect of thresholding the frequency-domain representation of the signals, and Fig. 6.11(d) show how the Laplacian based method reaches the highest quality and an accurate detection of the damage thanks to the lower background noise level and the energy trapping of the incident waves caused by the bonded mass.

### 6.3 Results and discussion

The presented damage imaging algorithms were applied to three different datasets acquired with air-coupled probes and related to the plate-like components sketched in Fig. 6.12(a-c) and 6.13. Figs. 6.12 (d-f) show snapshots for a mentioned sets up respectively as well as a snapshot at 78, 82 and 93  $\mu\text{s}$  in the epoxy, composite and aluminium plates. The response of the system in such areas was measured with rapid scan acquisition

by using the CNC machine to place the air-coupled probe in a subset of  $51 \times 51$  cartesian grid points and then by applying the compressive sensing technique to recover the wavefield in the full grid. The generated datasets are three dimensional matrices, of size  $N \times M \times T$ , where  $N, M, T$  represent cardinalities in the spatial x direction, in the y direction, and the number of time samples, respectively. Fig. 6.14 show the measured frequency wavenumber plot with the propagation direction for: Epoxy glass plate (a), composite plate(b), and Honeycomb plate (c).

As can be seen in Figs. 6.15, 6.16 and 6.17, the analyzed processing techniques combined with the CS acquisitions detect damage very effectively. Figs. 6.15(a), 6.16(a) and 6.17 (a) show the resulting plot for cumulative kinetic energy (CKED), epoxy glass, composite and aluminum plates respectively with the 50% of downsamples. Although the damage map in 6.15(a) has a peak in correspondence to the source transducer position, both the energy trapping and shadowing of the incident waves caused by the bonded mass are evident. The damage imaging results based on the differential compressive sensing technique are shown in Figs. 6.15(b), 6.16(b) and 6.17(b) with 50% of the sampling rate and 30 iterations. Figs. 6.15, 6.16 and 6.17(c) illustrate the damage processing produced by the local wavenumber estimation procedure and Figs. 6.15, 6.16 and 6.17(d) show the Laplacian filtering technique for the epoxy, composite and aluminium plates, respectively. In all the considered cases, the local energy associated to the mass is lower with respect to the one associated to the acoustic source. Figs. 6.15, 6.16 and 6.17(d) look qualitatively better with respect to the others, because of the lower background noise level in all the considered cases. Quantitative comparisons of the different analysis modalities' performances can be found in Table 6.7. To assess the accuracy and precision of the damage image results the SNR and CNR were calculated with the methodology described in [55]. In particular, the SNR is defined by the ratio of the average signal value to the standard deviation of the signal [431]:

$$SNR = 20 \log_{10} \left( \frac{\mu(w(x, y))}{\sigma(w(x, y))} \right), \quad (6.9)$$

where  $\sigma$  is the standard deviation of the signal and  $\mu$  is the average of the signal  $w(x, y)$ . While CNR was computed basing on eq. (6.3).

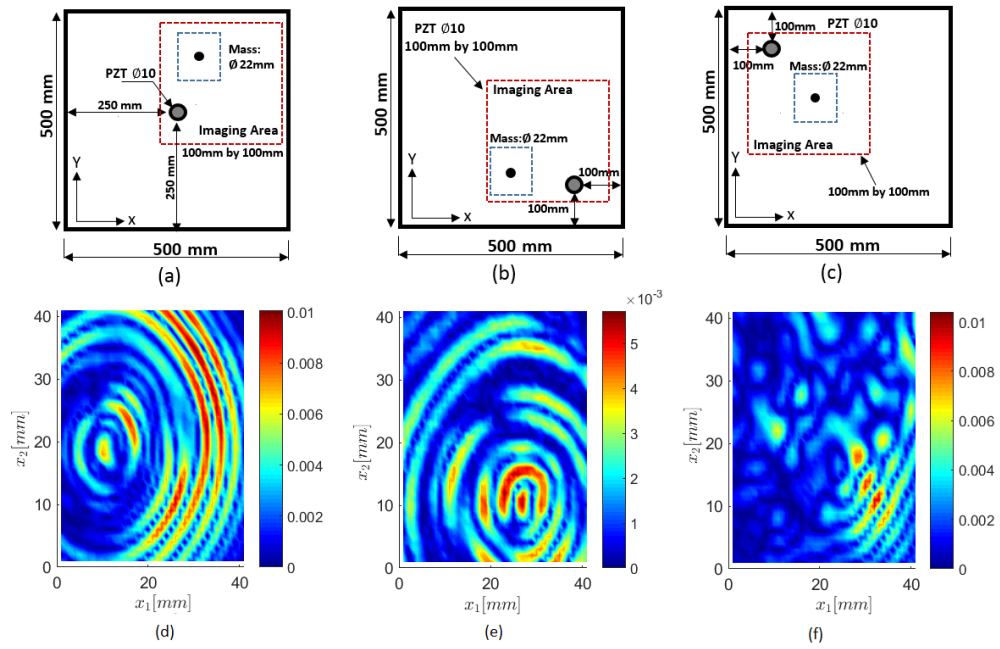


Figure 6.12: Sketch of the three setups (a, b, c), the dashed lines are the perimeters of the imaged areas. Snapshots of the measured wavefield at  $t = 78 \mu s$ ,  $t = 82 \mu s$  and  $t = 93 \mu s$  for the Epoxy glass, CFRP and Honeycomb plates, (d, e, and f), respectively.



Figure 6.13: The three plates investigated with air couple probes: Epoxy glass, CFRP and Honeycomb plates, respectively.

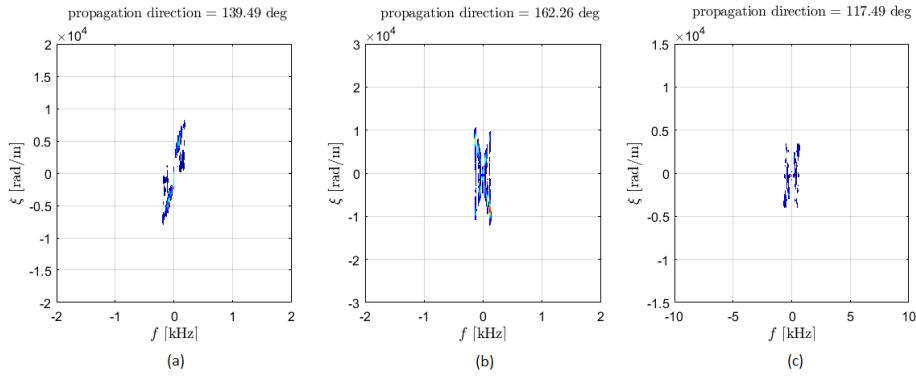


Figure 6.14: Frequency-wavenumber map with the propagation direction for the Epoxy glass (a), Composite (b) and Honeycomb (c) plates.

As demonstrated by the cases discussed in this study, all techniques resulted in a fairly accurate detection of the damage and have high SNR. However, the Laplacian filtering method reaches the highest quality in term of SNR, while the LW technique is the best as far as computational time is concerned.

Fig. 6.18 shows the SNR performance achieved with different damage imaging modalities when the air-coupled transducers were used to acquire the wavefields on the epoxy glass plate. The CS recovery was performed by setting the number of iterations equal to 30, and by preserving the 20%, 33% and 50% of the samples of the cartesian grid.

Future work will investigate: i) the possibility to exploit these imaging modalities to characterize the entity of the defect, and ii) the possibility to further decrease the number of scan points by using different subsampling strategies or different sparsifying representations.

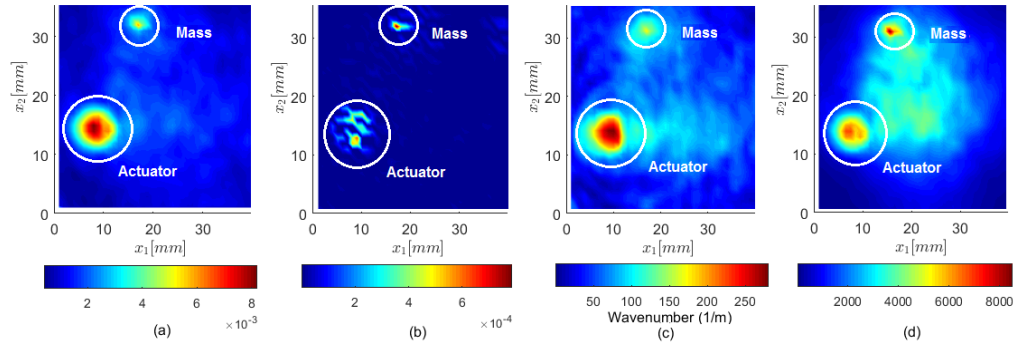


Figure 6.15: CKED (a), Differential CS with 50% of subsamples and 30 iterations by using FFT2D (b), LW (c), Laplacian filter(d) on the epoxy glass.

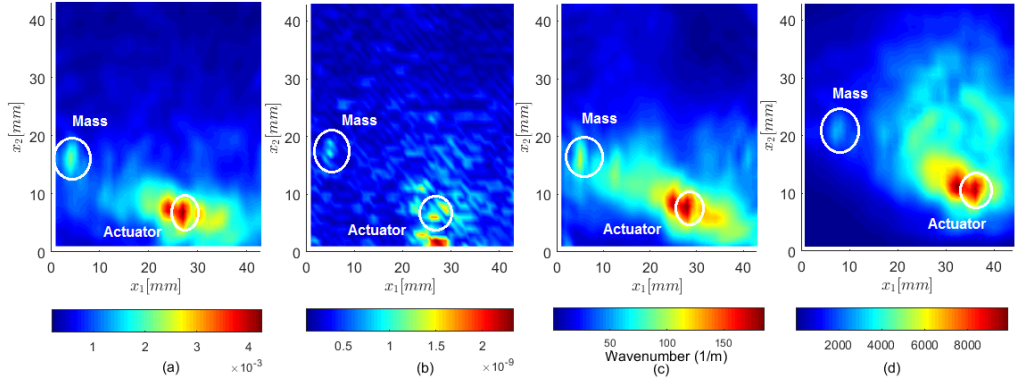


Figure 6.16: CKED (a), Differential CS with 50% of subsamples and 30 iterations by using FFT2D (b), LW (c), Laplacian filter (d) on the CFRP plate.

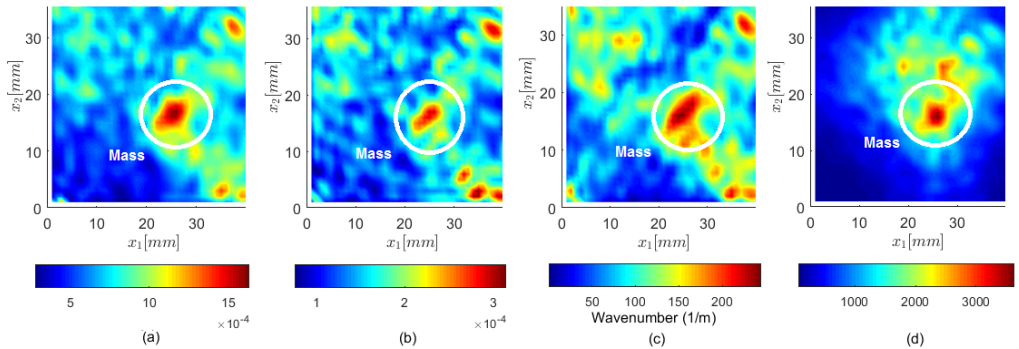


Figure 6.17: CKED (a), Differential CS with 50% of subsamples and 30 iterations by using FFT2D (b), LW (c), Laplacian filter (d) on the aluminum plate.

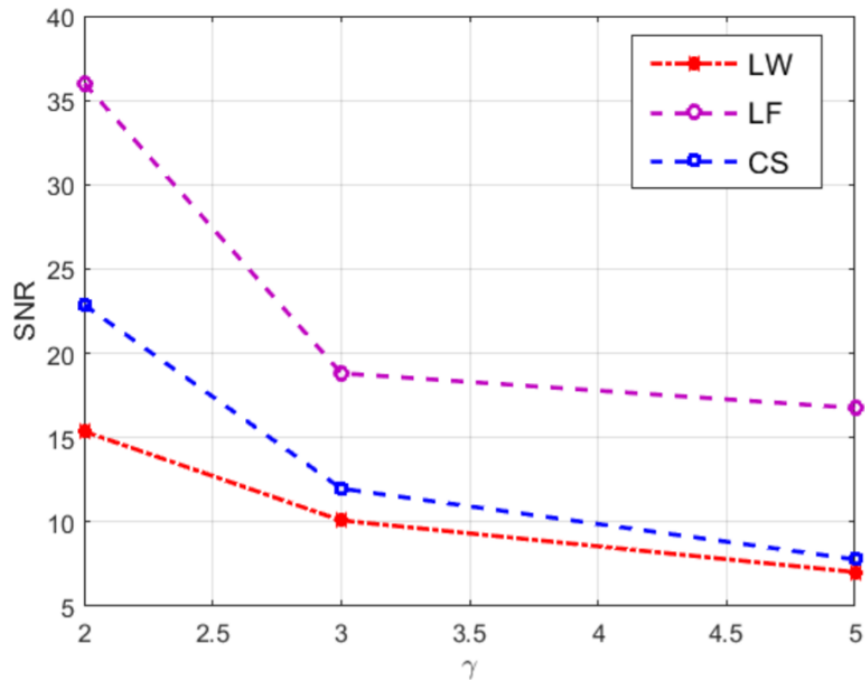


Figure 6.18: SNR performances achieved with the 30 number of iterations of the SPGL1 algorithm for 20%, 33% and 50% of the downsamples for the epoxy glass.

Table 6.7: Comparison of the techniques for wavefield obtained in the epoxy glass, CFRP and Honeycomb plates with 50% of downsamples.

Method	Data acquisition	Computational time	SNR	CNR	Plate
CS	600 S	405 S	22.88	18.18	Epoxy
LW	600 S	127 S	15.37	14.36	
LF	600 S	480 S	36.02	18.13	
CS	600 S	495 S	20.84	4.82	Composite
LW	600 S	127 S	14.46	19.01	
LF	600 S	480 S	20.82	15.96	
CS	600 S	615 S	15.05	4.54	Aluminum
LW	600 S	127 S	15.61	4.67	
LF	600 S	480 S	38.25	19.33	



# Chapter 7

## Conclusions

### 7.1 Conclusion

This dissertation describes the research conducted to develop guided wave methodologies for full-wavefield damage imaging. Non-contact-based systems have been widely studied for damage detection and localization for SHM applications. In particular, wavefields can be generated by a fixed piezoelectric transducer and measured by SLDV, or air-coupled moving transducers. However, the use of air-coupled transducers, which are low cost devices when compared with SLDV, has several disadvantages, mainly related to data quality. On the other hand, SLDV needs several hours of automatic measurements to improve SNR of ultrasonic responses via averaging procedures.

For this reason, there is an urgent need in trying to develop novel methodologies or technologies to speed up the acquisition time while preserving the informative content of full wavefield acquisitions. In this context, the contribution of this dissertation is twofold:

- First, a rapid algorithm for wavefield imaging based on the CS and CNN frameworks was proposed. The main goal was to show the effectiveness of combining CS with deep learning methods, leading to an increase in the speed of inspection, without sacrificing the quality of wavefield images. The presented CS technique was applied

to reduce acquisition time. Then, CNNs are applied to recover HR images from LR sub-sampled wavefields. The WI datasets were obtained by measuring the out-of-plane displacement field arising from the propagation and interaction of the ultrasonic guided waves with simulated defects in the structures. The structures were chosen as being representative of typical aerospace structures. The datasets were obtained at one specific frequency (75 kHz), associated to different wavelengths, depending on the structure and the propagating mode.

- Secondly, the compatibility of the CS recovery with multiple damage imaging techniques was investigated. Namely, the implemented signal processing methods were i) the cumulative Kinect energy, ii) differential compressive sensing iii) local wavenumber mapping, and iv) Laplacian filtering. It was shown that: 1) signals with high SNR could be achieved, and 2) such methods are all compatible with the CS approach which allows to minimize the acquisition time. In order to validate the proposed techniques, several experiments were conducted with aluminium, composite and epoxy plates.

The damage imaging produced by the differential Compressive sensing was particularly effective. Such imaging method is based on the analysis of the difference between the CS recovery of the downsampled wavefield that can be achieved by using different sparsity promoting dictionaries. It was shown that computing the difference between the recovery performed in the 2D and 3D Fourier domain produces the most effective results, leading to a fast and artifact-free defect imaging strategy. In particular the interactions of elastic waves with damages clearly emerge over the incident waves as well as with respect to the wave reflections from the structure edges. Experimental results demonstrate that the proposed technique can be applied in a variety of structural components to reduce acquisition time and achieve high performance in defect detection and localization.

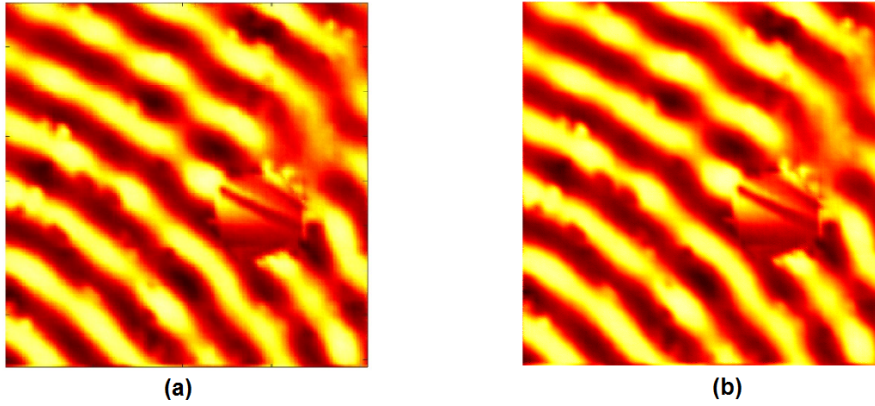


Figure 7.1: Comparison of the recovery of a 10% down-sampled image with VDSR, DCSCN and PR. The three deep learning architectures produce very similar results.

## 7.2 Future work developments

In the conducted research the CS was applied to averaged data. However, the possibility to apply the CS algorithm to raw data is very interesting and will be explored in future works.

Moreover, in this dissertation, the VDSR scheme was extensively evaluated for HR images recovery but many variants of the Deep Learning architectures are currently under investigation in the scientific community. A nice and very recent review on the topic is provided in [428].

For example, I have tested another Deep learning architecture (namely the DCSCN [432]) and found that the results are comparable to the VDSR approach (See Fig. 7.1). Additional investigations related to the usage of alternative deep learning schemes (such as the Pixel Recursive – PR – method 7.2) could possibly lead to further performance improvement.

HR reconstruction of wider band displacement fields could be performed by enriching the training set with WI datasets at other frequencies/wavelengths. This also will be the object of future works.

Finally, an important aspect which requires additional investigations is the trade-off between undersampling ratios and defect detectability. On

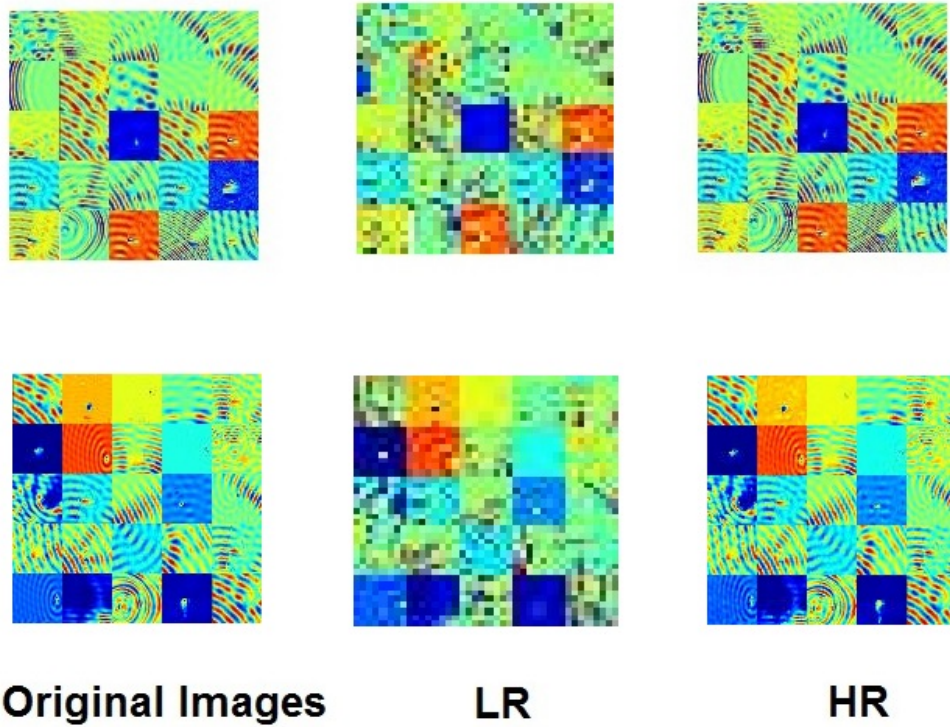


Figure 7.2: Illustration of pixel recursive super resolution model trained end-to-end on a dataset of wavefield images. The left column shows original wavefield images. The middle and last columns show  $8 \times 8$  low resolution inputs from the test set and  $32 \times 32$  high resolution images.

one hand, imaging the defect with just 1% of the scanpoints of the full grid would be a very impressive result, and the combination of CS+VDSR seems to work very well even at such high undersampling ratios. On the other hand, the wave reflections caused by defects may be very weak, since they represent a relatively small fraction of the wave energy captured by the measurements and they are rapidly vanishing far from the defect location. In this sense, moving from SSIM =0.91 (achieved with the simple CS at CR=10%) to SSIM=0.96 (achieved with the deep learning framework) is very important. This can be qualitatively judged by looking at the recovered wavefield around the (relatively large) mass location (See Fig. 5.6). So, by further lowering the number of scan points, it can be faced with the risk of having undetected defects (especially, small defects) due to the larger gaps between scan point locations.

Finally, on a broader scope, future work will investigate the capability of the presented compressed imaging modality to *characterize* the type of defect.



# Bibliography

- [1] V. Giurgiutiu, *Structural health monitoring: with piezoelectric wafer active sensors*. Elsevier, 2007.
- [2] J. L. Rose, S. Pelts, and M. Quarry, “A comb transducer for mode control in guided wave nde,” in *1997 IEEE Ultrasonics Symposium Proceedings. An International Symposium (Cat. No. 97CH36118)*, vol. 2. IEEE, 1997, pp. 1033–1036.
- [3] M. Wevers, F. Fransens, and K. Leuven, “Ultrasonic Lamb wave inspection of aircraft components using integrated optical fibre sensing technology,” in *Proceedings of the European Conference of non-destructive testing, September, 2006*, pp. 25–29.
- [4] F. Li, H. Murayama, K. Kageyama, and T. Shirai, “Guided wave and damage detection in composite laminates using different fiber optic sensors,” *Sensors*, vol. 9, no. 5, pp. 4005–4021, 2009.
- [5] M. Dupont, D. Osmont, R. Gouyon, and D. L. Balageas, “Permanent monitoring of damaging impacts by a piezoelectric sensor based integrated system,” *Structural health monitoring 2000, Lancaster, PA, Technomic Publishing Co., 1999*, pp. 561–570, 1999.
- [6] L. Yu and V. Giurgiutiu, “In situ 2-d piezoelectric wafer active sensors arrays for guided wave damage detection,” *Ultrasonics*, vol. 48, no. 2, pp. 117–134, 2008.

- [7] R. B. Williams, G. Park, D. J. Inman, and W. K. Wilkie, “An overview of composite actuators with piezoceramic fibers,” *Proceeding of IMAC XX*, vol. 47, 2002.
- [8] A. Raghavan and C. E. Cesnik, “Review of guided-wave structural health monitoring,” *Shock and Vibration Digest*, vol. 39, no. 2, pp. 91–116, 2007.
- [9] J. L. Rose, “A baseline and vision of ultrasonic guided wave inspection potential,” *Journal of pressure vessel technology*, vol. 124, no. 3, pp. 273–282, 2002.
- [10] B. Culshaw, S. Pierce, and W. Staszekski, “Condition monitoring in composite materials: an integrated systems approach,” *Proceedings of the Institution of Mechanical Engineers, Part I: Journal of Systems and Control Engineering*, vol. 212, no. 3, pp. 189–202, 1998.
- [11] N. Rajic, C. Davis, and A. Thomson, “Acoustic-wave-mode separation using a distributed bragg grating sensor,” *Smart Materials and Structures*, vol. 18, no. 12, p. 125005, 2009.
- [12] P. D. Wilcox, “Omni-directional guided wave transducer arrays for the rapid inspection of large areas of plate structures,” *IEEE transactions on ultrasonics, ferroelectrics, and frequency control*, vol. 50, no. 6, pp. 699–709, 2003.
- [13] P. Kudela, M. Radziński, and W. Ostachowicz, “Identification of cracks in thin-walled structures by means of wavenumber filtering,” *Mechanical Systems and Signal Processing*, vol. 50, pp. 456–466, 2015.
- [14] C. Boller, “Structural health monitoring—an introduction and definitions,” *Encyclopedia of Structural Health Monitoring*, 2009.
- [15] C. R. Farrar and K. Worden, “An introduction to structural health monitoring,” *Philosophical Transactions of the Royal Society A: Mathematical, Physical and Engineering Sciences*, vol. 365, no. 1851, pp. 303–315, 2006.



- [16] W. Ostachowicz and A. Güemes, *New trends in structural health monitoring*. Springer Science & Business Media, 2013, vol. 542.
- [17] H. Sohn, C. R. Farrar, F. M. Hemez, D. D. Shunk, D. W. Stinemates, B. R. Nadler, and J. J. Czarnecki, “A review of structural health monitoring literature: 1996–2001,” *Los Alamos National Laboratory, USA*, 2003.
- [18] D. J. Inman, C. R. Farrar, V. L. Junior, and V. S. Junior, *Damage prognosis: for aerospace, civil and mechanical systems*. John Wiley & Sons, 2005.
- [19] C. R. Farrar and N. A. Lieven, “Damage prognosis: the future of structural health monitoring,” *Philosophical Transactions of the Royal Society A: Mathematical, Physical and Engineering Sciences*, vol. 365, no. 1851, pp. 623–632, 2006.
- [20] R. A. Swartz, D. Jung, J. P. Lynch, Y. Wang, D. Shi, and M. P. Flynn, “Design of a wireless sensor for scalable distributed in-network computation in a structural health monitoring system,” in *Proceedings of the 5th International Workshop on Structural Health Monitoring*, 2005, pp. 12–14.
- [21] S. Gopalakrishnan, M. Ruzzene, and S. Hanagud, *Computational techniques for structural health monitoring*. Springer Science & Business Media, 2011.
- [22] E. P. Carden and P. Fanning, “Vibration based condition monitoring: a review,” *Structural health monitoring*, vol. 3, no. 4, pp. 355–377, 2004.
- [23] A. Deraemaeker and K. Worden, *New trends in vibration based structural health monitoring*. Springer Science & Business Media, 2012, vol. 520.
- [24] W. Fan and P. Qiao, “Vibration-based damage identification methods: a review and comparative study,” *Structural health monitoring*, vol. 10, no. 1, pp. 83–111, 2011.

- [25] S. W. Doebling, C. R. Farrar, M. B. Prime *et al.*, “A summary review of vibration-based damage identification methods,” *Shock and vibration digest*, vol. 30, no. 2, pp. 91–105, 1998.
- [26] O. Huth, G. Feltrin, J. Maeck, N. Kilic, and M. Motavalli, “Damage identification using modal data: Experiences on a prestressed concrete bridge,” *Journal of Structural Engineering*, vol. 131, no. 12, pp. 1898–1910, 2005.
- [27] J. M. W. Brownjohn, P. Moyo, P. Omenzetter, and Y. Lu, “Assessment of highway bridge upgrading by dynamic testing and finite-element model updating,” *Journal of Bridge Engineering*, vol. 8, no. 3, pp. 162–172, 2003.
- [28] X. Lin, L. Zhang, Q. Guo, and Y. Zhang, “Dynamic finite element model updating of prestressed concrete continuous box-girder bridge,” *Earthquake Engineering and Engineering Vibration*, vol. 8, no. 3, pp. 399–407, 2009.
- [29] K. L. Rens, T. J. Wipf, and F. W. Klaiber, “Review of nondestructive evaluation techniques of civil infrastructure,” *Journal of performance of constructed facilities*, vol. 11, no. 4, pp. 152–160, 1997.
- [30] D. McCann and M. Forde, “Review of ndt methods in the assessment of concrete and masonry structures,” *Ndt & E International*, vol. 34, no. 2, pp. 71–84, 2001.
- [31] H. Lamb, “On waves in an elastic plate,” *Proceedings of the Royal Society of London. Series A, Containing papers of a mathematical and physical character*, vol. 93, no. 648, pp. 114–128, 1917.
- [32] L. Rayleigh, “Xvii. on the maintenance of vibrations by forces of double frequency, and on the propagation of waves through a medium endowed with a periodic structure,” *The London, Edinburgh, and Dublin Philosophical Magazine and Journal of Science*, vol. 24, no. 147, pp. 145–159, 1887.

- [33] J. W. Strutt, “On waves propagated along the plane surface of an elastic solid,” *Proceedings of the London Mathematical Society*, vol. 17, no. 1, pp. 4–11, 1885.
- [34] A. Love, “Some problems of geodynamics, being an essay to which the adams’ prize in the university of cambridge was adjudged in 1911,” *Bull. Amer. Math. Soc.*, vol. 20, pp. 432–434, 1914.
- [35] A. E. H. Love, *Some problems of geodynamics*. Cambridge University Press, 2015.
- [36] R. Stoneley, “Elastic waves at the surface of separation of two solids,” *Proceedings of the Royal Society of London. Series A, Containing Papers of a Mathematical and Physical Character*, vol. 106, no. 738, pp. 416–428, 1924.
- [37] J. Scholte, “On the stoneley wave equation,” *Proceedings of the Koninklijke Nederlandse Akademie van Wetenschappen*, vol. 45, no. part 1, pp. 20–25, 1942.
- [38] R. Dalton, P. Cawley, and M. Lowe, “The potential of guided waves for monitoring large areas of metallic aircraft fuselage structure,” *Journal of Nondestructive Evaluation*, vol. 20, no. 1, pp. 29–46, 2001.
- [39] Y. Ren, L. Qiu, S. Yuan, and Z. Su, “A diagnostic imaging approach for online characterization of multi-impact in aircraft composite structures based on a scanning spatial-wavenumber filter of guided wave,” *Mechanical Systems and Signal Processing*, vol. 90, pp. 44–63, 2017.
- [40] P. B. Nagy and L. Adler, “Nondestructive evaluation of adhesive joints by guided waves,” *Journal of Applied Physics*, vol. 66, no. 10, pp. 4658–4663, 1989.
- [41] Z. Fan, M. Castaings, M. J. Lowe, C. Biateau, and P. Fromme, “Feature-guided waves for monitoring adhesive shear modulus in bonded stiffeners,” *Ndt & E International*, vol. 54, pp. 96–102, 2013.

- [42] R. Seifried, L. J. Jacobs, and J. Qu, "Propagation of guided waves in adhesive bonded components," *NDT & E International*, vol. 35, no. 5, pp. 317–328, 2002.
- [43] M. Castaings, D. Singh, and P. Viot, "Sizing of impact damages in composite materials using ultrasonic guided waves," *NDT & E International*, vol. 46, pp. 22–31, 2012.
- [44] M. Mitra and S. Gopalakrishnan, "Guided wave based structural health monitoring: A review," *Smart Materials and Structures*, vol. 25, no. 5, p. 053001, 2016.
- [45] W. Staszewski, B. Lee, L. Mallet, and F. Scarpa, "Structural health monitoring using scanning laser vibrometry: I. Lamb wave sensing," *Smart Materials and Structures*, vol. 13, no. 2, p. 251, 2004.
- [46] P. C. Chang, A. Flatau, and S. Liu, "Health monitoring of civil infrastructure," *Structural health monitoring*, vol. 2, no. 3, pp. 257–267, 2003.
- [47] J. P. Lynch, "An overview of wireless structural health monitoring for civil structures," *Philosophical Transactions of the Royal Society A: Mathematical, Physical and Engineering Sciences*, vol. 365, no. 1851, pp. 345–372, 2006.
- [48] Z. Su, L. Ye, and Y. Lu, "Guided Lamb waves for identification of damage in composite structures: A review," *Journal of sound and vibration*, vol. 295, no. 3, pp. 753–780, 2006.
- [49] A. Raghavan, "Guided-wave structural health monitoring," 2007.
- [50] C.-T. Ng and M. Veidt, "A Lamb-wave-based technique for damage detection in composite laminates," *Smart materials and structures*, vol. 18, no. 7, p. 074006, 2009.
- [51] J. L. Rose, "Successes and challenges in ultrasonic guided waves for ndt and shm," in *Proceedings of the National Seminar & Exhibition on Non-Destructive Evaluation*, 2009, pp. 10–12.

- [52] Y. Keshmiri Esfandabadi, M. Bilodeau, P. Masson, and L. De Marchi, “Deep learning for enhancing wavefield image quality in fast non-contact inspections,” *Structural Health Monitoring*, p. 1475921719873112, 2019.
- [53] E. B. Flynn, S. Y. Chong, G. J. Jarmer, and J.-R. Lee, “Structural imaging through local wavenumber estimation of guided waves,” *Ndt & E International*, vol. 59, pp. 1–10, 2013.
- [54] H. Sohn, D. Dutta, J. Yang, M. Desimio, S. Olson, and E. Swenson, “A wavefield imaging technique for delamination detection in composite structures,” DTIC Document, Tech. Rep., 2010.
- [55] Y. K. Esfandabadi, L. De Marchi, N. Testoni, A. Marzani, and G. Masetti, “Full wavefield analysis and damage imaging through compressive sensing in Lamb wave inspections,” *IEEE Transactions on Ultrasonics, Ferroelectrics, and Frequency Control*, 2017.
- [56] P. Cawley, “The rapid non-destructive inspection of large composite structures,” *Composites*, vol. 25, no. 5, pp. 351–357, 1994.
- [57] A. Raghavan and C. E. Cesnik, “Effects of elevated temperature on guided-wave structural health monitoring,” *Journal of Intelligent Material Systems and Structures*, vol. 19, no. 12, pp. 1383–1398, 2008.
- [58] J. B. Harley and J. M. Moura, “Scale transform signal processing for optimal ultrasonic temperature compensation,” *IEEE transactions on ultrasonics, ferroelectrics, and frequency control*, vol. 59, no. 10, pp. 2226–2236, 2012.
- [59] C. Liu, J. B. Harley, M. Bergés, D. W. Greve, and I. J. Oppenheim, “Robust ultrasonic damage detection under complex environmental conditions using singular value decomposition,” *Ultrasonics*, vol. 58, pp. 75–86, 2015.
- [60] A. J. Croxford, J. Moll, P. D. Wilcox, and J. E. Michaels, “Efficient temperature compensation strategies for guided wave structural health monitoring,” *Ultrasonics*, vol. 50, no. 4-5, pp. 517–528, 2010.

- [61] F. Lanza di Scalea and S. Salamone, “Temperature effects in ultrasonic Lamb wave structural health monitoring systems,” *The Journal of the Acoustical Society of America*, vol. 124, no. 1, pp. 161–174, 2008.
- [62] A. Marzani and S. Salamone, “Numerical prediction and experimental verification of temperature effect on plate waves generated and received by piezoceramic sensors,” *Mechanical Systems and Signal Processing*, vol. 30, pp. 204–217, 2012.
- [63] A. Degtyar, W. Huang, and S. Rokhlin, “Wave propagation in stressed composites,” *The Journal of the Acoustical Society of America*, vol. 104, no. 4, pp. 2192–2199, 1998.
- [64] K. Salama and C. Ling, “The effect of stress on the temperature dependence of ultrasonic velocity,” *Journal of Applied Physics*, vol. 51, no. 3, pp. 1505–1509, 1980.
- [65] J. Michaels, S. Lee, X. Chen, and T. Michaels, “Load-enhanced imaging of fatigue cracks via sparse guided wave arrays,” in *Proceedings of the 8th International Workshop on Structural Health Monitoring*. September, 2011, pp. 1150–1157.
- [66] S. J. Lee, N. Gandhi, J. E. Michaels, and T. E. Michaels, “Comparison of the effects of applied loads and temperature variations on guided wave propagation,” in *AIP Conference Proceedings*, vol. 1335, no. 1. AIP, 2011, pp. 175–182.
- [67] J. L. Rose, *Ultrasonic waves in solid media*. Cambridge university press, 2004.
- [68] P. Wilcox, M. Lowe, and P. Cawley, “The effect of dispersion on long-range inspection using ultrasonic guided waves,” *NDT & E International*, vol. 34, no. 1, pp. 1–9, 2001.
- [69] F. Gao, L. Zeng, J. Lin, and Z. Luo, “Mode separation in frequency–wavenumber domain through compressed sensing of far-field Lamb waves,” *Measurement Science and Technology*, vol. 28, no. 7, p. 075004, 2017.

- [70] F. Benmeddour, S. Grondel, J. Assaad, and E. Moulin, “Study of the fundamental lamb modes interaction with asymmetrical discontinuities,” *NDT & e International*, vol. 41, no. 5, pp. 330–340, 2008.
- [71] M. H. Sherafat, N. Quaegebeur, L. Lessard, P. Hubert, and P. Masson, “Guided wave propagation through composite bonded joints,” in *EWSHM-7th European Workshop on Structural Health Monitoring*, 2014.
- [72] C. Willberg, S. Duczek, J. Vivar-Perez, and Z. Ahmad, “Simulation methods for guided wave-based structural health monitoring: a review,” *Applied Mechanics Reviews*, vol. 67, no. 1, p. 010803, 2015.
- [73] Z. Su, C. Yang, N. Pan, L. Ye, and L.-M. Zhou, “Assessment of delamination in composite beams using shear horizontal (sh) wave mode,” *Composites science and technology*, vol. 67, no. 2, pp. 244–251, 2007.
- [74] B. Lee and W. Staszewski, “Modelling of Lamb waves for damage detection in metallic structures: Part i. wave propagation,” *Smart Materials and Structures*, vol. 12, no. 5, p. 804, 2003.
- [75] D. Balageas, C. Fritzen, and A. Guemes, “Structural health monitoring (london: Iste),” 2006.
- [76] K. Diamanti and C. Soutis, “Structural health monitoring techniques for aircraft composite structures,” *Progress in Aerospace Sciences*, vol. 46, no. 8, pp. 342–352, 2010.
- [77] J. E. Michaels and T. E. Michaels, “Ultrasonic signal processing for structural health monitoring,” in *AIP Conference Proceedings*, vol. 700, no. 1. AIP, 2004, pp. 1476–1483.
- [78] C. Truong, D.-H. Kang, J.-R. Lee, and C. Farrar, “Comparative study of laser doppler vibrometer and capacitive air-coupled transducer for ultrasonic propagation imager and the new development of an efficient ultrasonic wavenumber imaging algorithm,” *Strain*, vol. 51, no. 4, pp. 332–342, 2015.

- [79] V. Giurgiutiu, J. Bao, and W. Zhao, "Piezoelectric wafer active sensor embedded ultrasonics in beams and plates," *Experimental mechanics*, vol. 43, no. 4, pp. 428–449, 2003.
- [80] V. Giurgiutiu, "Tuned Lamb wave excitation and detection with piezoelectric wafer active sensors for structural health monitoring," *Journal of intelligent material systems and structures*, vol. 16, no. 4, pp. 291–305, 2005.
- [81] S. Pelts, D. Jiao, and J. Rose, "A comb transducer for guided wave generation and mode selection," in *1996 IEEE Ultrasonics Symposium. Proceedings*, vol. 2. IEEE, 1996, pp. 857–860.
- [82] W. Zhu, J. Rose, J. Barshinger, and V. Agarwala, "Ultrasonic guided wave ndt for hidden corrosion detection," *Journal of Research in Nondestructive Evaluation*, vol. 10, no. 4, pp. 205–225, 1998.
- [83] P. Wilcox, M. Lowe, and P. Cawley, "Mode and transducer selection for long range Lamb wave inspection," *Journal of intelligent material systems and structures*, vol. 12, no. 8, pp. 553–565, 2001.
- [84] D. N. Alleyne and P. Cawley, "The interaction of Lamb waves with defects," *IEEE transactions on ultrasonics, ferroelectrics, and frequency control*, vol. 39, no. 3, pp. 381–397, 1992.
- [85] Z. Chang and A. Mal, "Scattering of Lamb waves from a rivet hole with edge cracks," *Mechanics of materials*, vol. 31, no. 3, pp. 197–204, 1999.
- [86] M. Platte, "Pvdf ultrasonic transducers," *Ferroelectrics*, vol. 75, no. 1, pp. 327–337, 1987.
- [87] R. Monkhouse, P. Wilcox, and P. Cawley, "Flexible interdigital pvdf transducers for the generation of Lamb waves in structures," *Ultrasonics*, vol. 35, no. 7, pp. 489–498, 1997.
- [88] D. C. Betz, G. Thursby, B. Culshaw, and W. J. Staszewski, "Acousto-ultrasonic sensing using fiber bragg gratings," *Smart Materials and Structures*, vol. 12, no. 1, p. 122, 2003.



- [89] G. Alers, “Emat designs for special applications,” *Materials Evaluation*, vol. 45, no. 10, pp. 1184–1194, 1987.
- [90] A. Raghavan and C. E. Cesnik, “Finite-dimensional piezoelectric transducer modeling for guided wave based structural health monitoring,” *Smart materials and structures*, vol. 14, no. 6, p. 1448, 2005.
- [91] E. Moulin, J. Assaad, C. Delebarre, and D. Osmont, “Modeling of Lamb waves generated by integrated transducers in composite plates using a coupled finite element–normal modes expansion method,” *The Journal of the Acoustical Society of America*, vol. 107, no. 1, pp. 87–94, 2000.
- [92] A. M. Kamal, B. Lin, and V. Giurgiutiu, “Exact analytical modeling of power and energy for multimode Lamb waves excited by piezoelectric wafer active sensors,” *Journal of intelligent material systems and structures*, vol. 25, no. 4, pp. 452–471, 2014.
- [93] J. Moll, M. V. Golub, E. Glushkov, N. Glushkova, and C.-P. Fritzen, “Non-axisymmetric Lamb wave excitation by piezoelectric wafer active sensors,” *Sensors and Actuators A: Physical*, vol. 174, pp. 173–180, 2012.
- [94] L. Yu, G. Bottai-Santoni, and V. Giurgiutiu, “Shear lag solution for tuning ultrasonic piezoelectric wafer active sensors with applications to Lamb wave array imaging,” *International Journal of Engineering Science*, vol. 48, no. 10, pp. 848–861, 2010.
- [95] G. Santoni-Bottai and V. Giurgiutiu, “Exact shear-lag solution for guided waves tuning with piezoelectric-wafer active sensors,” *AIAA journal*, vol. 50, no. 11, pp. 2285–2294, 2012.
- [96] Z. Liu, C. He, B. Wu, X. Wang, and S. Yang, “Circumferential and longitudinal defect detection using  $t(0, 1)$  mode excited by thickness shear mode piezoelectric elements,” *Ultrasonics*, vol. 44, pp. e1135–e1138, 2006.

- [97] W. Zhou, H. Li, and F.-G. Yuan, “Guided wave generation, sensing and damage detection using in-plane shear piezoelectric wafers,” *Smart Materials and Structures*, vol. 23, no. 1, p. 015014, 2013.
- [98] —, “Fundamental understanding of wave generation and reception using d36 type piezoelectric transducers,” *Ultrasonics*, vol. 57, pp. 135–143, 2015.
- [99] R. Badcock and E. Birt, “The use of 0-3 piezocomposite embedded Lamb wave sensors for detection of damage in advanced fibre composites,” *Smart Materials and Structures*, vol. 9, no. 3, p. 291, 2000.
- [100] M. Mańka, M. Rosiek, A. Martowicz, T. Stepinski, and T. Uhl, “Lamb wave transducers made of piezoelectric macro-fiber composite,” *Structural Control and Health Monitoring*, vol. 20, no. 8, pp. 1138–1158, 2013.
- [101] L. Yu and V. Giurgiutiu, “Piezoelectric wafer active sensors in Lamb wave-based structural health monitoring,” *JOM*, vol. 64, no. 7, pp. 814–822, 2012.
- [102] V. Giurgiutiu, A. Zagrai, and J. Bao, “Damage identification in aging aircraft structures with piezoelectric wafer active sensors,” *Journal of Intelligent Material Systems and Structures*, vol. 15, no. 9-10, pp. 673–687, 2004.
- [103] V. Giurgiutiu, B. Xu, and W. Liu, “Development and testing of high-temperature piezoelectric wafer active sensors for extreme environments,” *Structural Health Monitoring*, vol. 9, no. 6, pp. 513–525, 2010.
- [104] G. B. Santoni, L. Yu, B. Xu, and V. Giurgiutiu, “Lamb wave-mode tuning of piezoelectric wafer active sensors for structural health monitoring,” *Journal of Vibration and Acoustics*, vol. 129, no. 6, pp. 752–762, 2007.

- [105] M. Luukkala and P. Meriläinen, “Metal plate testing using airborne ultrasound,” *Ultrasonics*, vol. 11, no. 5, pp. 218–221, 1973.
- [106] M. Castaings and P. Cawley, “The generation, propagation, and detection of Lamb waves in plates using air-coupled ultrasonic transducers,” *The Journal of the Acoustical Society of America*, vol. 100, no. 5, pp. 3070–3077, 1996.
- [107] R. Kazys, A. Demcenko, L. Mazeika, R. Sliteris, and E. Zukauskas, “Ultrasonic air-coupled non-destructive testing of aerospace components,” in *DGZfP-Proceedings BB*, 2006.
- [108] T. Yonathan Sunarsa, P. Aryan, I. Jeon, B. Park, P. Liu, and H. Sohn, “A reference-free and non-contact method for detecting and imaging damage in adhesive-bonded structures using air-coupled ultrasonic transducers,” *Materials*, vol. 10, no. 12, p. 1402, 2017.
- [109] D. Schindel, D. Hutchins, and W. Grandia, “Capacitive and piezoelectric air-coupled transducers for resonant ultrasonic inspection,” *Ultrasonics*, vol. 34, no. 6, pp. 621–627, 1996.
- [110] I. Solodov and G. Busse, “Nonlinear air-coupled emission: The signature to reveal and image microdamage in solid materials,” *Applied Physics Letters*, vol. 91, no. 25, p. 251910, 2007.
- [111] R. S. Panda, P. Rajagopal, and K. Balasubramaniam, “An approach for defect visualization and identification in composite plate structures using air-coupled guided ultrasound,” in *AIP Conference Proceedings*, vol. 1650, no. 1. AIP, 2015, pp. 1299–1306.
- [112] ———, “Characterization of delamination-type damages in composite laminates using guided wave visualization and air-coupled ultrasound,” *Structural Health Monitoring*, vol. 16, no. 2, pp. 142–152, 2017.
- [113] Z. Liu, H. Yu, C. He, and B. Wu, “Delamination detection in composite beams using pure lamb mode generated by air-coupled ultrasonic transducer,” *Journal of Intelligent Material Systems and Structures*, vol. 25, no. 5, pp. 541–550, 2014.

- [114] N. Testoni, L. De Marchi, and A. Marzani, “Detection and characterization of delaminations in composite plates via air-coupled probes and warped-domain filtering,” *Composite Structures*, vol. 153, pp. 773–781, 2016.
- [115] J. E. Michaels and T. E. Michaels, “On the measurement of guided wavefields via air-coupled ultrasonic transducers,” in *AIP Conference Proceedings*, vol. 1650, no. 1. AIP, 2015, pp. 792–798.
- [116] —, “Detection of structural damage from the local temporal coherence of diffuse ultrasonic signals,” *IEEE transactions on ultrasonics, ferroelectrics, and frequency control*, vol. 52, no. 10, pp. 1769–1782, 2005.
- [117] M. S. Harb and F.-G. Yuan, “Damage imaging using non-contact air-coupled transducer/laser doppler vibrometer system,” *Structural Health Monitoring*, vol. 15, no. 2, pp. 193–203, 2016.
- [118] D. Tuzzeo and F. L. Di Scalea, “Noncontact air-coupled guided wave ultrasonics for detection of thinning defects in aluminum plates,” *Research in Nondestructive Evaluation*, vol. 13, no. 2, pp. 61–78, 2001.
- [119] M. Castaings and B. Hosten, “Lamb and sh waves generated and detected by air-coupled ultrasonic transducers in composite material plates,” *Ndt & E International*, vol. 34, no. 4, pp. 249–258, 2001.
- [120] J.-R. Lee, N. Sunuwar, and C.-Y. Park, “Comparative analysis of laser ultrasonic propagation imaging system with capacitance and piezoelectric air-coupled transducers,” *Journal of Intelligent Material Systems and Structures*, vol. 25, no. 5, pp. 551–562, 2014.
- [121] P.-Y. Le Bas, M. Remillieux, L. Pieczonka, J. Ten Cate, B. Anderson, and T. Ulrich, “Damage imaging in a laminated composite plate using an air-coupled time reversal mirror,” *Applied Physics Letters*, vol. 107, no. 18, p. 184102, 2015.

- [122] T. E. Michaels and J. E. Michaels, "Application of acoustic wavefield imaging to non-contact ultrasonic inspection of bonded components," in *AIP Conference Proceedings*, vol. 820, no. 1. AIP, 2006, pp. 1484–1491.
- [123] Y. K. Esfandabadi, A. Marzani, N. Testoni, and L. De Marchi, "Accelerated guided waves inspection using compressive sensing and local wavenumber domain analysis," in *2017 IEEE International Ultrasonics Symposium (IUS)*. IEEE, 2017, pp. 1–4.
- [124] Y. K. ESFANDABADI, A. MARZANI, and L. DE MARCHI, "Compressive sensing and local wavenumber estimations for fast damage imaging with guided waves inspections," *Structural Health Monitoring 2017*, no. shm, 2017.
- [125] Y. K. Esfandabadi, A. Marzani, and L. De Marchi, "Computation of image features for full-wavefield characterization in fast non-contact inspections," 2018.
- [126] ———, "Fast guided waves inspection using compressive sensing and wavenumber domain analysis," in *2017 IEEE Workshop on Environmental, Energy, and Structural Monitoring Systems (EESMS)*. IEEE, 2017, pp. 1–6.
- [127] Y. Yeh and H. Cummins, "Localized fluid flow measurements with an he–ne laser spectrometer," *Applied Physics Letters*, vol. 4, no. 10, pp. 176–178, 1964.
- [128] S. Pierce, B. Culshaw, W. Philp, F. Lecuyer, and R. Farlow, "Broadband Lamb wave measurements in aluminium and carbon/glass fibre reinforced composite materials using non-contacting laser generation and detection," *Ultrasonics*, vol. 35, no. 2, pp. 105–114, 1997.
- [129] N. Halliwell, "Laser-doppler measurement of vibrating surfaces: A portable instrument," *Journal of Sound Vibration*, vol. 62, pp. 312–315, 1979.
- [130] L. Drain, "The laser doppler concepts," 1980.

- [131] Z. Tian, C. A. Leckey, and L. Yu, “3d guided wave motion analysis on laminated composites,” in *AIP Conference Proceedings*, vol. 1581, no. 1. AIP, 2014, pp. 1149–1156.
- [132] W. Staszewski, B. Lee, and R. Traynor, “Fatigue crack detection in metallic structures with Lamb waves and 3d laser vibrometry,” *Measurement Science and Technology*, vol. 18, no. 3, p. 727, 2007.
- [133] E. D. Swenson, H. Sohn, S. E. Olson, and M. P. Desimio, “A comparison of 1d and 3d laser vibrometry measurements of Lamb waves,” in *Health Monitoring of Structural and Biological Systems 2010*, vol. 7650. International Society for Optics and Photonics, 2010, p. 765003.
- [134] E. D. Swenson, C. Owens, and C. Allen, “Interaction of Lamb waves with fatigue cracks in aluminum,” AIR FORCE INST OF TECH WRIGHT-PATTERSON AFB OH SCHOOL OF ENGINEERING AND . . . , Tech. Rep., 2011.
- [135] C. B. Scruby and L. E. Drain, *Laser ultrasonics techniques and applications*. CRC press, 1990.
- [136] P. Malinowski, T. Wandowski, P. Kudela, and W. Ostachowicz, “Laser vibrometry for guided wave propagation phenomena visualisation and damage detection,” in *AIP Conference Proceedings*, vol. 1253, no. 1. AIP, 2010, pp. 140–149.
- [137] H. Duffo, B. Morvan, and J.-L. Izbicki, “Interaction of Lamb waves on bonded composite plates with defects,” *Composite structures*, vol. 79, no. 2, pp. 229–233, 2007.
- [138] W. Ostachowicz, T. Wandowski, and P. Malinowski, “Damage detection using laser vibrometry,” in *2nd international symposium on NDT in aerospace*, vol. 2010, 2010, pp. 1–8.
- [139] H. Sohn, D. Dutta, J. Yang, M. DeSimio, S. Olson, and E. Swenson, “Automated detection of delamination and disbond from wavefield images obtained using a scanning laser vibrometer,” *Smart Materials and Structures*, vol. 20, no. 4, p. 045017, 2011.

- [140] M. Ruzzene, “Frequency-wavenumber domain filtering for improved damage visualization,” in *Ultrasonic And Advanced Methods For Non-destructive Testing And Material Characterization*. World Scientific, 2007, pp. 591–611.
- [141] T. E. Michaels, J. E. Michaels, and M. Ruzzene, “Frequency-wavenumber domain analysis of guided wavefields,” *Ultrasonics*, vol. 51, no. 4, pp. 452–466, 2011.
- [142] W. Xiao and L. Yu, “Nondestructive evaluation with fully non-contact air-coupled transducer-scanning laser doppler vibrometer Lamb wave system,” in *Nondestructive Characterization and Monitoring of Advanced Materials, Aerospace, Civil Infrastructure, and Transportation XIII*, vol. 10971. International Society for Optics and Photonics, 2019, p. 109711G.
- [143] L. Mallet, B. Lee, W. Staszewski, and F. Scarpa, “Structural health monitoring using scanning laser vibrometry: Ii. Lamb waves for damage detection,” *Smart Materials and Structures*, vol. 13, no. 2, p. 261, 2004.
- [144] W. Leong, W. Staszewski, B. Lee, and F. Scarpa, “Structural health monitoring using scanning laser vibrometry: Iii. Lamb waves for fatigue crack detection,” *Smart Materials and Structures*, vol. 14, no. 6, p. 1387, 2005.
- [145] J.-H. Lee and S.-J. Lee, “Application of laser-generated guided wave for evaluation of corrosion in carbon steel pipe,” *Ndt & E International*, vol. 42, no. 3, pp. 222–227, 2009.
- [146] C. Owens, E. Swenson, and C. Allen, “Visualization of Lamb wave interaction with a 5 mm fatigue crack using 1d ultra high frequency laser doppler vibrometry,” DTIC Document, Tech. Rep., 2011.
- [147] R. Longo, S. Vanlanduit, J. Vanherzeele, and P. Guillaume, “A method for crack sizing using laser doppler vibrometer measurements of surface acoustic waves,” *Ultrasonics*, vol. 50, no. 1, pp. 76–80, 2010.

- [148] C. Allen, C. Owens, and E. Swenson, “Lamb wave interaction with a t-joint,” *Structural Health Monitoring, Trans Tech Publications, Stanford*, pp. 2231–2236, 2011.
- [149] P. K. Rastogi, “Digital speckle pattern interferometry and related techniques,” *Digital Speckle Pattern Interferometry and Related Techniques*, by PK Rastogi (Editor), pp. 384. ISBN 0-471-49052-0. Wiley-VCH, December 2000., p. 384, 2000.
- [150] L. P. Scudder, D. Hutchins, and N. Guo, “Laser-generated ultrasonic guided waves in fiber-reinforced plates-theory and experiment,” *IEEE transactions on ultrasonics, ferroelectrics, and frequency control*, vol. 43, no. 5, pp. 870–880, 1996.
- [151] M. Harb and F. Yuan, “Non-contact ultrasonic technique for Lamb wave characterization in composite plates,” *Ultrasonics*, vol. 64, pp. 162–169, 2016.
- [152] W. Staszewski, S. Mahzan, and R. Traynor, “Health monitoring of aerospace composite structures—active and passive approach,” *composites Science and Technology*, vol. 69, no. 11-12, pp. 1678–1685, 2009.
- [153] W. Ostachowicz, M. Radziński, and P. Kudela, “50th anniversary article: comparison studies of full wavefield signal processing for crack detection,” *Strain*, vol. 50, no. 4, pp. 275–291, 2014.
- [154] L. Yu and Z. Tian, “Lamb wave structural health monitoring using a hybrid pzt-laser vibrometer approach,” *Structural Health Monitoring*, vol. 12, no. 5-6, pp. 469–483, 2013.
- [155] T. E. Michaels and J. E. Michaels, “Integrating monitoring and inspection with attached ultrasonic transducers,” in *Health Monitoring and Smart Nondestructive Evaluation of Structural and Biological Systems V*, vol. 6177. International Society for Optics and Photonics, 2006, p. 61770E.



- [156] A. Gannon, E. Wheeler, K. Brown, E. Flynn, and W. Warren, “A high-speed dual-stage ultrasonic guided wave system for localization and characterization of defects,” in *Structural Health Monitoring and Damage Detection, Volume 7*. Springer, 2015, pp. 123–136.
- [157] K. Holeczek, E. Starke, A. Winkler, M. Dannemann, and N. Modler, “Numerical and experimental characterization of fiber-reinforced thermoplastic composite structures with embedded piezoelectric sensor-actuator arrays for ultrasonic applications,” *Applied Sciences*, vol. 6, no. 3, p. 55, 2016.
- [158] T. E. Michaels, M. Ruzzene, and J. E. Michaels, “Incident wave removal through frequency-wavenumber filtering of full wavefield data,” in *AIP Conference Proceedings*, vol. 1096, no. 1. AIP, 2009, pp. 604–611.
- [159] S. E. Olson, M. P. DeSimio, M. J. Davies, E. D. Swenson, and H. Sohn, “Computational Lamb wave model validation using 1d and 3d laser vibrometer measurements,” in *Health Monitoring of Structural and Biological Systems 2010*, vol. 7650. International Society for Optics and Photonics, 2010, p. 76500M.
- [160] P. Fromme and M. B. Sayir, “Detection of cracks at rivet holes using guided waves,” *Ultrasonics*, vol. 40, no. 1-8, pp. 199–203, 2002.
- [161] J.-R. Lee, H.-J. Shin, C. C. Chia, D. Dhital, D.-J. Yoon, and Y.-H. Huh, “Long distance laser ultrasonic propagation imaging system for damage visualization,” *Optics and Lasers in Engineering*, vol. 49, no. 12, pp. 1361–1371, 2011.
- [162] J.-R. Lee, C. C. Chia, C.-Y. Park, and H. Jeong, “Laser ultrasonic anomalous wave propagation imaging method with adjacent wave subtraction: algorithm,” *Optics & Laser Technology*, vol. 44, no. 5, pp. 1507–1515, 2012.
- [163] D. Algernon, B. Gräfe, F. Mielentz, B. Köhler, and F. Schubert, “Imaging of the elastic wave propagation in concrete using scanning

- techniques: application for impact-echo and ultrasonic echo methods,” *Journal of Nondestructive Evaluation*, vol. 27, no. 1-3, pp. 83–97, 2008.
- [164] P. Castellini, M. Martarelli, and E. Tomasini, “Laser doppler vibrometry: Development of advanced solutions answering to technology’s needs,” *Mechanical systems and signal processing*, vol. 20, no. 6, pp. 1265–1285, 2006.
- [165] D. Dhital, J. R. Lee, C. Y. Park, and E. Flynn, “Laser excitation and fully non-contact sensing ultrasonic propagation imaging system for damage evaluation,” in *Industrial and Commercial Applications of Smart Structures Technologies 2012*, vol. 8343. International Society for Optics and Photonics, 2012, p. 83430D.
- [166] R. E. Green Jr, “Non-contact ultrasonic techniques,” *Ultrasonics*, vol. 42, no. 1-9, pp. 9–16, 2004.
- [167] J.-R. Lee, J. Takatsubo, and N. Toyama, “Disbond monitoring at wing stringer tip based on built-in ultrasonic transducers and a pulsed laser,” *Smart materials and structures*, vol. 16, no. 4, p. 1025, 2007.
- [168] J.-R. Lee, C. C. Chia, H. J. Shin, C.-Y. Park, and D. J. Yoon, “Laser ultrasonic propagation imaging method in the frequency domain based on wavelet transformation,” *Optics and Lasers in Engineering*, vol. 49, no. 1, pp. 167–175, 2011.
- [169] J.-R. Lee, S. Y. Chong, H. Jeong, and C.-W. Kong, “A time-of-flight mapping method for laser ultrasound guided in a pipe and its application to wall thinning visualization,” *NDT & E International*, vol. 44, no. 8, pp. 680–691, 2011.
- [170] J.-R. Lee, H. Jeong, C. C. Ciang, D.-J. Yoon, and S.-S. Lee, “Application of ultrasonic wave propagation imaging method to automatic damage visualization of nuclear power plant pipeline,” *Nuclear engineering and design*, vol. 240, no. 10, pp. 3513–3520, 2010.

- [171] J.-R. Lee, S. Y. Chong, N. Sunuwar, and C. Y. Park, “Repeat scanning technology for laser ultrasonic propagation imaging,” *Measurement Science and Technology*, vol. 24, no. 8, p. 085201, 2013.
- [172] E. B. Flynn, “Embedded multi-tone ultrasonic excitation and continuous-scanning laser doppler vibrometry for rapid and remote imaging of structural defects,” in *EWSHM-7th European workshop on structural health monitoring*, 2014.
- [173] S. Yashiro, J. Takatsubo, and N. Toyama, “An ndt technique for composite structures using visualized Lamb-wave propagation,” *Composites Science and Technology*, vol. 67, no. 15-16, pp. 3202–3208, 2007.
- [174] S. Yashiro, J. Takatsubo, H. Miyauchi, and N. Toyama, “A novel technique for visualizing ultrasonic waves in general solid media by pulsed laser scan,” *NDT & E International*, vol. 41, no. 2, pp. 137–144, 2008.
- [175] J.-R. Lee, J. Takatsubo, N. Toyama, and D.-H. Kang, “Health monitoring of complex curved structures using an ultrasonic wavefield propagation imaging system,” *Measurement science and technology*, vol. 18, no. 12, p. 3816, 2007.
- [176] V. Giurgiutiu and J. Bao, “Embedded-ultrasonics structural radar for in situ structural health monitoring of thin-wall structures,” *Structural Health Monitoring*, vol. 3, no. 2, pp. 121–140, 2004.
- [177] D. Kim and M. Philen, “Guided wave beamsteering using mfc phased arrays for structural health monitoring: analysis and experiment,” *Journal of Intelligent Material Systems and Structures*, vol. 21, no. 10, pp. 1011–1024, 2010.
- [178] A. Purekar and D. Pines, “Damage detection in thin composite laminates using piezoelectric phased sensor arrays and guided Lamb wave interrogation,” *Journal of Intelligent Material Systems and Structures*, vol. 21, no. 10, pp. 995–1010, 2010.

- [179] M. Ruzzene, B. Xu, S. J. Lee, T. E. Michaels, and J. E. Michaels, “Damage visualization via beamforming of frequency-wavenumber filtered wavefield data,” in *Health Monitoring of Structural and Biological Systems 2010*, vol. 7650. International Society for Optics and Photonics, 2010, p. 76500L.
- [180] P. D. Wilcox, “A rapid signal processing technique to remove the effect of dispersion from guided wave signals,” *IEEE transactions on ultrasonics, ferroelectrics, and frequency control*, vol. 50, no. 4, pp. 419–427, 2003.
- [181] M. Romanoni, S. Gonella, N. Apetre, and M. Ruzzene, “Two-dimensional periodic actuators for frequency-based beam steering,” *Smart materials and structures*, vol. 18, no. 12, p. 125023, 2009.
- [182] B. Yoo, A. Purekar, Y. Zhang, and D. Pines, “Piezoelectric-paint-based two-dimensional phased sensor arrays for structural health monitoring of thin panels,” *Smart Materials and Structures*, vol. 19, no. 7, p. 075017, 2010.
- [183] M. Senesi, B. Xu, and M. Ruzzene, “Experimental characterization of periodic frequency-steerable arrays for structural health monitoring,” *Smart Materials and Structures*, vol. 19, no. 5, p. 055026, 2010.
- [184] S. J. Lee, N. Gandhi, J. S. Hall, J. E. Michaels, B. Xu, T. E. Michaels, and M. Ruzzene, “Baseline-free guided wave imaging via adaptive source removal,” *Structural Health Monitoring*, vol. 11, no. 4, pp. 472–481, 2012.
- [185] J. E. Michaels, “Detection, localization and characterization of damage in plates with an in situ array of spatially distributed ultrasonic sensors,” *Smart Materials and Structures*, vol. 17, no. 3, p. 035035, 2008.
- [186] T. Clarke, P. Cawley, P. D. Wilcox, and A. J. Croxford, “Evaluation of the damage detection capability of a sparse-array guided-wave shm system applied to a complex structure under varying thermal

- conditions,” *IEEE transactions on ultrasonics, ferroelectrics, and frequency control*, vol. 56, no. 12, 2009.
- [187] R. Zhu, G. Huang, and F. Yuan, “Fast damage imaging using the time-reversal technique in the frequency–wavenumber domain,” *Smart Materials and Structures*, vol. 22, no. 7, p. 075028, 2013.
- [188] H. W. Park, S. B. Kim, and H. Sohn, “Understanding a time reversal process in Lamb wave propagation,” *Wave Motion*, vol. 46, no. 7, pp. 451–467, 2009.
- [189] H. Sohn, H. W. Park, K. H. Law, and C. R. Farrar, “Damage detection in composite plates by using an enhanced time reversal method,” *Journal of Aerospace Engineering*, vol. 20, no. 3, pp. 141–151, 2007.
- [190] T. Hay, R. Royer, H. Gao, X. Zhao, and J. Rose, “A comparison of embedded sensor Lamb wave ultrasonic tomography approaches for material loss detection,” *Smart materials and structures*, vol. 15, no. 4, p. 946, 2006.
- [191] K. R. Leonard and M. K. Hinders, “Lamb wave tomography of pipe-like structures,” *Ultrasonics*, vol. 43, no. 7, pp. 574–583, 2005.
- [192] C. H. Wang, J. T. Rose, and F.-K. Chang, “A synthetic time-reversal imaging method for structural health monitoring,” *Smart materials and structures*, vol. 13, no. 2, p. 415, 2004.
- [193] Z. Su, L. Cheng, X. Wang, L. Yu, and C. Zhou, “Predicting delamination of composite laminates using an imaging approach,” *Smart Materials and Structures*, vol. 18, no. 7, p. 074002, 2009.
- [194] C. Holmes, B. W. Drinkwater, and P. D. Wilcox, “Advanced post-processing for scanned ultrasonic arrays: Application to defect detection and classification in non-destructive evaluation,” *Ultrasonics*, vol. 48, no. 6-7, pp. 636–642, 2008.
- [195] X. P. Qing, S. Beard, S. B. Shen, S. Banerjee, I. Bradley, M. M. Salama, and F.-K. Chang, “Development of a real-time active pipeline integrity

- detection system,” *Smart Materials and Structures*, vol. 18, no. 11, p. 115010, 2009.
- [196] J. S. Hall and J. E. Michaels, “Computational efficiency of ultrasonic guided wave imaging algorithms,” *IEEE transactions on ultrasonics, ferroelectrics, and frequency control*, vol. 58, no. 1, pp. 244–248, 2011.
- [197] T. Wandowski, P. Malinowski, and W. Ostachowicz, “Damage detection with concentrated configurations of piezoelectric transducers,” *Smart Materials and Structures*, vol. 20, no. 2, p. 025002, 2011.
- [198] L. Qiu, M. Liu, X. Qing, and S. Yuan, “A quantitative multidamage monitoring method for large-scale complex composite,” *Structural Health Monitoring*, vol. 12, no. 3, pp. 183–196, 2013.
- [199] J. Chen, Z. Su, and L. Cheng, “Identification of corrosion damage in submerged structures using fundamental anti-symmetric Lamb waves,” *Smart Materials and Structures*, vol. 19, no. 1, p. 015004, 2009.
- [200] R. Sicard, A. Chahbaz, and J. Goyette, “Guided Lamb waves and l-saft processing technique for enhanced detection and imaging of corrosion defects in plates with small depth-to wavelength ratio,” *IEEE transactions on ultrasonics, ferroelectrics, and frequency control*, vol. 51, no. 10, pp. 1287–1297, 2004.
- [201] N. Hu, T. Shimomukai, C. Yan, and H. Fukunaga, “Identification of delamination position in cross-ply laminated composite beams using s0 lamb mode,” *Composites Science and Technology*, vol. 68, no. 6, pp. 1548–1554, 2008.
- [202] Y. Lu, L. Ye, Z. Su, and N. Huang, “Quantitative evaluation of crack orientation in aluminium plates based on Lamb waves,” *Smart Materials and Structures*, vol. 16, no. 5, p. 1907, 2007.
- [203] B. Hosten, L. Moreau, and M. Castaings, “Reflection and transmission coefficients for guided waves reflected by defects in viscoelastic material plates,” *The Journal of the Acoustical Society of America*, vol. 121, no. 6, pp. 3409–3417, 2007.

- [204] N. Hu, J. Li, Y. Cai, C. Yan, Y. Zhang, J. Qiu, K. Sakai, Y. Liu, X. Peng, and B. Yan, “Locating delamination in composite laminated beams using the A0 lamb mode,” *Mechanics of Advanced Materials and Structures*, vol. 19, no. 6, pp. 431–440, 2012.
- [205] N. Hu, T. Shimomukai, H. Fukunaga, and Z. Su, “Damage identification of metallic structures using A0 mode of Lamb waves,” *Structural Health Monitoring*, vol. 7, no. 3, pp. 271–285, 2008.
- [206] L. De Marchi, A. Marzani, N. Speciale, and E. Viola, “A passive monitoring technique based on dispersion compensation to locate impacts in plate-like structures,” *Smart Materials and Structures*, vol. 20, no. 3, p. 035021, 2011.
- [207] K. Xu, D. Ta, P. Moilanen, and W. Wang, “Mode separation of Lamb waves based on dispersion compensation method,” *The Journal of the Acoustical Society of America*, vol. 131, no. 4, pp. 2714–2722, 2012.
- [208] L. Ying, L. Demanet, and E. Candes, “3d discrete curvelet transform,” in *Wavelets XI*, vol. 5914. International Society for Optics and Photonics, 2005, p. 591413.
- [209] L. Demanet and L. Ying, “Curvelets and wave atoms for mirror-extended images,” in *Wavelets XII*, vol. 6701. International Society for Optics and Photonics, 2007, p. 67010J.
- [210] J. S. Hall and J. E. Michaels, “Adaptive dispersion compensation for guided wave imaging,” in *AIP Conference Proceedings*, vol. 1430, no. 1. AIP, 2012, pp. 623–630.
- [211] F. Schöpfer, F. Binder, A. Wöstehoff, T. Schuster, S. von Ende, S. Föll, and R. Lammering, “Accurate determination of dispersion curves of guided waves in plates by applying the matrix pencil method to laser vibrometer measurement data,” *CEAS Aeronautical Journal*, vol. 4, no. 1, pp. 61–68, 2013.
- [212] K. Xu, D. Ta, and W. Wang, “Multiridge-based analysis for separating individual modes from multimodal guided wave signals in long bones,”

- IEEE transactions on ultrasonics, ferroelectrics, and frequency control*, vol. 57, no. 11, pp. 2480–2490, 2010.
- [213] K. Xu, P. Laugier, and J.-G. Minonzio, “Dispersive radon transform,” *The Journal of the Acoustical Society of America*, vol. 143, no. 5, pp. 2729–2743, 2018.
- [214] A. Leger and M. Deschamps, *Ultrasonic wave propagation in non homogeneous media*. Springer Science & Business Media, 2009, vol. 128.
- [215] J.-C. Hong, K. H. Sun, and Y. Y. Kim, “Dispersion-based short-time fourier transform applied to dispersive wave analysis,” *The Journal of the Acoustical Society of America*, vol. 117, no. 5, pp. 2949–2960, 2005.
- [216] L. Ambrozinski, T. Stepinski, P. Packo, and T. Uhl, “Self-focusing Lamb waves based on the decomposition of the time-reversal operator using time–frequency representation,” *Mechanical Systems and Signal Processing*, vol. 27, pp. 337–349, 2012.
- [217] D.-a. Ta, K. Huang, W.-q. Wang, Y.-y. Wang, and L. H. Le, “Identification and analysis of multimode guided waves in tibia cortical bone,” *Ultrasonics*, vol. 44, pp. e279–e284, 2006.
- [218] M. Niethammer, L. J. Jacobs, J. Qu, and J. Jarzynski, “Time-frequency representations of Lamb waves,” *The Journal of the Acoustical Society of America*, vol. 109, no. 5, pp. 1841–1847, 2001.
- [219] L. De Marchi, A. Marzani, S. Caporale, and N. Speciale, “Ultrasonic guided-waves characterization with warped frequency transforms,” *IEEE transactions on ultrasonics, ferroelectrics, and frequency control*, vol. 56, no. 10, pp. 2232–2240, 2009.
- [220] L. Zeng, M. Zhao, J. Lin, and W. Wu, “Waveform separation and image fusion for Lamb waves inspection resolution improvement,” *NDT & E International*, vol. 79, pp. 17–29, 2016.



- [221] M. Meo, G. Zumpano, M. Piggott, and G. Marengo, "Impact identification on a sandwich plate from wave propagation responses," *Composite structures*, vol. 71, no. 3-4, pp. 302–306, 2005.
- [222] T. Kundu, H. Nakatani, and N. Takeda, "Acoustic source localization in anisotropic plates," *Ultrasonics*, vol. 52, no. 6, pp. 740–746, 2012.
- [223] M. Tracy and F.-K. Chang, "Identifying impacts in composite plates with piezoelectric strain sensors, part i: Theory," *Journal of Intelligent Material Systems and Structures*, vol. 9, no. 11, pp. 920–928, 1998.
- [224] Z. Sharif-Khodaie, M. Ghajari, and M. Aliabadi, "Determination of impact location on composite stiffened panels," *Smart Materials and Structures*, vol. 21, no. 10, p. 105026, 2012.
- [225] C. Chen and F.-G. Yuan, "Impact source identification in finite isotropic plates using a time-reversal method: theoretical study," *Smart Materials and Structures*, vol. 19, no. 10, p. 105028, 2010.
- [226] W. J. Staszewski, K. Worden, R. Wardle, and G. R. Tomlinson, "Fail-safe sensor distributions for impact detection in composite materials," *Smart Materials and Structures*, vol. 9, no. 3, p. 298, 2000.
- [227] D. Akopian, A. Melkonyan, and C. P. Chen, "Validation of hdop measure for impact detection in sensor network-based structural health monitoring," *IEEE Sensors Journal*, vol. 9, no. 9, pp. 1098–1102, 2009.
- [228] J. F. Markmiller and F.-K. Chang, "Sensor network optimization for a passive sensing impact detection technique," *Structural Health Monitoring*, vol. 9, no. 1, pp. 25–39, 2010.
- [229] E. B. Flynn and M. D. Todd, "A bayesian approach to optimal sensor placement for structural health monitoring with application to active sensing," *Mechanical Systems and Signal Processing*, vol. 24, no. 4, pp. 891–903, 2010.

- [230] O. Diligent, M. Lowe, E. Le Clézio, M. Castaings, and B. Hosten, “Prediction and measurement of nonpropagating lamb modes at the free end of a plate when the fundamental antisymmetric mode  $a_0$  is incident,” *The Journal of the Acoustical Society of America*, vol. 113, no. 6, pp. 3032–3042, 2003.
- [231] J. E. Michaels and T. E. Michaels, “Guided wave signal processing and image fusion for in situ damage localization in plates,” *Wave motion*, vol. 44, no. 6, pp. 482–492, 2007.
- [232] J. S. Hall and J. E. Michaels, “Minimum variance ultrasonic imaging applied to an in situ sparse guided wave array,” *IEEE Transactions on Ultrasonics, Ferroelectrics, and Frequency Control*, vol. 57, no. 10, pp. 2311–2323, 2010.
- [233] V. Memmolo, N. Boffa, L. Maio, E. Monaco, and F. Ricci, “Damage localization in composite structures using a guided waves based multi-parameter approach,” *Aerospace*, vol. 5, no. 4, p. 111, 2018.
- [234] H. Cho and C. J. Lissenden, “Structural health monitoring of fatigue crack growth in plate structures with ultrasonic guided waves,” *Structural Health Monitoring*, vol. 11, no. 4, pp. 393–404, 2012.
- [235] X. Chen, J. E. Michaels, S. J. Lee, and T. E. Michaels, “Load-differential imaging for detection and localization of fatigue cracks using Lamb waves,” *Ndt & E International*, vol. 51, pp. 142–149, 2012.
- [236] A. Purekar, D. Pines, S. Sundararaman, and D. Adams, “Directional piezoelectric phased array filters for detecting damage in isotropic plates,” *Smart Materials and Structures*, vol. 13, no. 4, p. 838, 2004.
- [237] L. Ambrozinski, B. Piwakowski, T. Stepinski, L. Pieczonka, and T. Uhl, “Pitch-catch air-coupled ultrasonic technique for detection of barely visible impact damages in composite laminates,” in *EWSHM-7th European workshop on structural Health monitoring*, 2014.

- [238] L. Ambrozinski, T. Stepinski, and T. Uhl, “2d aperture synthesis for Lamb wave imaging using co-arrays,” in *Health Monitoring of Structural and Biological Systems 2014*, vol. 9064. International Society for Optics and Photonics, 2014, p. 90642A.
- [239] L. De Marchi, J. Moll, and A. Marzani, “A sparsity promoting algorithm for time of flight estimation in guided waves-based shm,” in *EWSHM-7th European Workshop on Structural Health Monitoring*, 2014.
- [240] M. Engholm, T. Stepinski, and T. Olofsson, “Imaging and suppression of lamb modes using adaptive beamforming,” *Smart Materials and Structures*, vol. 20, no. 8, p. 085024, 2011.
- [241] P. Fromme, P. D. Wilcox, M. J. Lowe, and P. Cawley, “On the development and testing of a guided ultrasonic wave array for structural integrity monitoring,” *ieee transactions on ultrasonics, ferroelectrics, and frequency control*, vol. 53, no. 4, pp. 777–785, 2006.
- [242] A. Leleux, P. Micheau, and M. Castaings, “Long range detection of defects in composite plates using Lamb waves generated and detected by ultrasonic phased array probes,” *Journal of Nondestructive Evaluation*, vol. 32, no. 2, pp. 200–214, 2013.
- [243] P. Malinowski, T. Wandowski, I. Trendafilova, and W. Ostachowicz, “A phased array-based method for damage detection and localization in thin plates,” *Structural Health Monitoring*, vol. 8, no. 1, pp. 5–15, 2009.
- [244] J. P. Koduru, S. Momeni, and J. L. Rose, “Phased annular array transducers for omnidirectional guided wave mode control in isotropic plate like structures,” *Smart Materials and Structures*, vol. 22, no. 12, p. 125022, 2013.
- [245] F. Yan and J. L. Rose, “Guided wave phased array beam steering in composite plates,” in *Health Monitoring of Structural and Biological Systems 2007*, vol. 6532. International Society for Optics and Photonics, 2007, p. 65320G.

- [246] J. Rajagopalan, K. Balasubramaniam, and C. Krishnamurthy, “A phase reconstruction algorithm for Lamb wave based structural health monitoring of anisotropic multilayered composite plates,” *The Journal of the Acoustical Society of America*, vol. 119, no. 2, pp. 872–878, 2006.
- [247] P. Osterc, “Phased array beamsteering in composite laminates for guided wave structural health monitoring,” 2015.
- [248] A. H. Nayfeh, *Wave propagation in layered anisotropic media: With application to composites*. Elsevier, 1995, vol. 39.
- [249] E. Glushkov, N. Glushkova, A. Eremin, and R. Lammering, “Group velocity of cylindrical guided waves in anisotropic laminate composites,” *The Journal of the Acoustical Society of America*, vol. 135, no. 1, pp. 148–154, 2014.
- [250] J. E. Michaels, “Ultrasonic wavefield imaging: Research tool or emerging nde method?” in *AIP Conference Proceedings*, vol. 1806, no. 1. AIP Publishing, 2017, p. 020001.
- [251] T.-Y. Yu and R. Haupt, “Damage inspection of fiber reinforced polymer-concrete systems using a distant acoustic-laser nde technique,” in *Nondestructive Characterization for Composite Materials, Aerospace Engineering, Civil Infrastructure, and Homeland Security 2010*, vol. 7649. International Society for Optics and Photonics, 2010, p. 76491J.
- [252] S.-C. Hong, A.-D. Abetew, J.-R. Lee, and J.-B. Ihn, “Three dimensional evaluation of aluminum plates with wall-thinning by full-field pulse-echo laser ultrasound,” *Optics and Lasers in Engineering*, vol. 99, pp. 58–65, 2017.
- [253] I. Mueller and C.-P. Fritzen, “Inspection of piezoceramic transducers used for structural health monitoring,” *Materials*, vol. 10, no. 1, p. 71, 2017.

- [254] J. L. Blackshire, “Enhanced damage characterization using wavefield imaging methods,” in *AIP Conference Proceedings*, vol. 1806, no. 1. AIP Publishing, 2017, p. 090008.
- [255] L. Yu, Z. Tian, and C. A. Leckey, “Crack imaging and quantification in aluminum plates with guided wave wavenumber analysis methods,” *Ultrasonics*, vol. 62, pp. 203–212, 2015.
- [256] O. Mesnil, H. Yan, M. Ruzzene, K. Paynabar, and J. Shi, “Fast wavenumber measurement for accurate and automatic location and quantification of defect in composite,” *Structural Health Monitoring*, vol. 15, no. 2, pp. 223–234, 2016.
- [257] L. Yu, Z. Tian, X. Li, R. Zhu, and G. Huang, “Core–skin debonding detection in honeycomb sandwich structures through guided wave wavefield analysis,” *Journal of Intelligent Material Systems and Structures*, vol. 30, no. 9, pp. 1306–1317, 2019.
- [258] H. Sohn, E. D. Swenson, S. E. Olson, M. P. DeSimio, and D. Dutta, “Delamination detection in composite structures using laser vibrometer measurement of Lamb waves,” in *Health Monitoring of Structural and Biological Systems 2010*, vol. 7650. International Society for Optics and Photonics, 2010, p. 76500P.
- [259] B. Park, Y.-K. An, and H. Sohn, “Visualization of hidden delamination and debonding in composites through noncontact laser ultrasonic scanning,” *Composites science and technology*, vol. 100, pp. 10–18, 2014.
- [260] J. E. Michaels, A. J. Dawson, T. E. Michaels, and M. Ruzzene, “Approaches to hybrid shm and nde of composite aerospace structures,” in *Health Monitoring of Structural and Biological Systems 2014*, vol. 9064. International Society for Optics and Photonics, 2014, p. 906427.
- [261] Y.-K. An, B. Park, and H. Sohn, “Complete noncontact laser ultrasonic imaging for automated crack visualization in a plate,” *Smart Materials and Structures*, vol. 22, no. 2, p. 025022, 2013.

- [262] Y.-K. An, J. M. Kim, and H. Sohn, “Laser lock-in thermography for detection of surface-breaking fatigue cracks on uncoated steel structures,” *Ndt & E International*, vol. 65, pp. 54–63, 2014.
- [263] T. E. Michaels and J. E. Michaels, “Monitoring and characterizing corrosion in aluminum using Lamb waves and attached sensors,” in *Health Monitoring of Structural and Biological Systems 2007*, vol. 6532. International Society for Optics and Photonics, 2007, p. 65321G.
- [264] D. Dutta, H. Sohn, and J. Y. Yang, “A non-contact structural health monitoring system through laser based excitation and sensing of ultrasonic guided waves,” in *The 16th US National Congress of Theoretical and Applied Mechanics*. Theoretical and Applied Mechanics, 2010.
- [265] A. Katunin, K. Dragan, and M. Dziendzikowski, “Damage identification in aircraft composite structures: A case study using various non-destructive testing techniques,” *Composite structures*, vol. 127, pp. 1–9, 2015.
- [266] F. Ricci, A. K. Mal, E. Monaco, L. Maio, N. D. Boffa, M. Di Palma, and L. Lecce, “Guided waves in layered plate with delaminations,” in *EWSHM-7th European Workshop on Structural Health Monitoring*, 2014.
- [267] A. Migot, Y. Bhuiyan, and V. Giurgiutiu, “Numerical and experimental investigation of damage severity estimation using Lamb wave-based imaging methods,” *Journal of Intelligent Material Systems and Structures*, vol. 30, no. 4, pp. 618–635, 2019.
- [268] P. Kudela, M. Radzienski, and W. Ostachowicz, “Impact induced damage assessment by means of Lamb wave image processing,” *Mechanical Systems and Signal Processing*, vol. 102, pp. 23–36, 2018.
- [269] E. Glushkov, N. Glushkova, M. V. Golub, J. Moll, and C.-P. Fritzen, “Wave energy trapping and localization in a plate with a delamination,” *Smart Materials and Structures*, vol. 21, no. 12, p. 125001, 2012.

- [270] T. Hayashi and K. Kawashima, "Single mode extraction from multiple modes of Lamb wave and its application to defect detection," *JSME International Journal Series A Solid Mechanics and Material Engineering*, vol. 46, no. 4, pp. 620–626, 2003.
- [271] C. Ramadas, K. Balasubramaniam, M. Joshi, and C. Krishnamurthy, "Interaction of lamb mode (ao) with structural discontinuity and generation of "turning modes" in a t-joint," *Ultrasonics*, vol. 51, no. 5, pp. 586–595, 2011.
- [272] M. D. Rogge and C. A. Leckey, "Characterization of impact damage in composite laminates using guided wavefield imaging and local wavenumber domain analysis," *Ultrasonics*, vol. 53, no. 7, pp. 1217–1226, 2013.
- [273] C. A. Leckey, M. D. Rogge, and F. R. Parker, "Guided waves in anisotropic and quasi-isotropic aerospace composites: Three-dimensional simulation and experiment," *Ultrasonics*, vol. 54, no. 1, pp. 385–394, 2014.
- [274] L. Wang and F. Yuan, "Group velocity and characteristic wave curves of Lamb waves in composites: Modeling and experiments," *Composites science and technology*, vol. 67, no. 7-8, pp. 1370–1384, 2007.
- [275] M. Castaings and B. Hosten, "Ultrasonic guided waves for health monitoring of high-pressure composite tanks," *Ndt & E International*, vol. 41, no. 8, pp. 648–655, 2008.
- [276] S. Salamone, I. Bartoli, F. Lanza Di Scalea, and S. Coccia, "Guided-wave health monitoring of aircraft composite panels under changing temperature," *Journal of Intelligent Material Systems and Structures*, vol. 20, no. 9, pp. 1079–1090, 2009.
- [277] T. Kundu, S. Das, S. A. Martin, and K. V. Jata, "Locating point of impact in anisotropic fiber reinforced composite plates," *Ultrasonics*, vol. 48, no. 3, pp. 193–201, 2008.

- [278] K. Salas and C. Cesnik, “Guided wave structural health monitoring using clover transducers in composite materials,” *Smart Materials and Structures*, vol. 19, no. 1, p. 015014, 2009.
- [279] F. Song, G. Huang, and G. Hu, “Online guided wave-based debonding detection in honeycomb sandwich structures,” *Aiaa Journal*, vol. 50, no. 2, pp. 284–293, 2012.
- [280] V. Giurgiutiu and C. Soutis, “Enhanced composites integrity through structural health monitoring,” *Applied Composite Materials*, vol. 19, no. 5, pp. 813–829, 2012.
- [281] N. Guo and P. Cawley, “The interaction of Lamb waves with delaminations in composite laminates,” *The Journal of the Acoustical Society of America*, vol. 94, no. 4, pp. 2240–2246, 1993.
- [282] G. Petculescu, S. Krishnaswamy, and J. D. Achenbach, “Group delay measurements using modally selective Lamb wave transducers for detection and sizing of delaminations in composites,” *Smart Materials and Structures*, vol. 17, no. 1, p. 015007, 2007.
- [283] C. M. Yeum, H. Sohn, J. B. Ihn, and H. J. Lim, “Instantaneous delamination detection in a composite plate using a dual piezoelectric transducer network,” *Composite Structures*, vol. 94, no. 12, pp. 3490–3499, 2012.
- [284] Z. Tian, L. Yu, and C. Leckey, “Delamination detection and quantification on laminated composite structures with Lamb waves and wavenumber analysis,” *Journal of Intelligent Material Systems and Structures*, vol. 26, no. 13, pp. 1723–1738, 2015.
- [285] O. Mesnil, C. A. Leckey, and M. Ruzzene, “Instantaneous and local wavenumber estimations for damage quantification in composites,” *Structural Health Monitoring*, vol. 14, no. 3, pp. 193–204, 2015.
- [286] P. D. Juarez and C. A. Leckey, “Multi-frequency local wavenumber analysis and ply correlation of delamination damage,” *Ultrasonics*, vol. 62, pp. 56–65, 2015.



- [287] C. Ramadas, K. Balasubramaniam, M. Joshi, and C. Krishnamurthy, “Interaction of guided Lamb waves with an asymmetrically located delamination in a laminated composite plate,” *Smart Materials and Structures*, vol. 19, no. 6, p. 065009, 2010.
- [288] H. Sohn, D. Dutta, J.-Y. Yang, H.-J. Park, M. DeSimio, S. Olson, and E. Swenson, “Delamination detection in composites through guided wave field image processing,” *Composites science and technology*, vol. 71, no. 9, pp. 1250–1256, 2011.
- [289] T. Hayashi and K. Kawashima, “Multiple reflections of Lamb waves at a delamination,” *Ultrasonics*, vol. 40, no. 1-8, pp. 193–197, 2002.
- [290] M. H. Sherafat, R. Guitel, N. Quaegebeur, L. Lessard, P. Hubert, and P. Masson, “Guided wave scattering behavior in composite bonded assemblies,” *Composite Structures*, vol. 136, pp. 696–705, 2016.
- [291] M. H. Sherafat, R. Guitel, N. Quaegebeur, P. Hubert, L. Lessard, and P. Masson, “Structural health monitoring of a composite skin-stringer assembly using within-the-bond strategy of guided wave propagation,” *Materials & Design*, vol. 90, pp. 787–794, 2016.
- [292] M. D. Rogge and C. Leckey, “Local guided wavefield analysis for characterization of delaminations in composites,” in *AIP Conference Proceedings*, vol. 1511, no. 1. AIP, 2013, pp. 963–970.
- [293] Z. Tian, L. Yu, C. Leckey, and J. Seebo, “Guided wave imaging for detection and evaluation of impact-induced delamination in composites,” *Smart Materials and Structures*, vol. 24, no. 10, p. 105019, 2015.
- [294] A. J. Dawson, J. E. Michaels, J. W. Kummer, and T. E. Michaels, “Quantification of shear wave scattering from far-surface defects via ultrasonic wavefield measurements,” *IEEE transactions on ultrasonics, ferroelectrics, and frequency control*, vol. 64, no. 3, pp. 590–601, 2017.
- [295] D. Alleyne and P. Cawley, “A two-dimensional fourier transform method for the measurement of propagating multimode signals,” *The*

- Journal of the Acoustical Society of America*, vol. 89, no. 3, pp. 1159–1168, 1991.
- [296] L. H. Tenek, E. G. Henneke II, and M. D. Gunzburger, “Vibration of delaminated composite plates and some applications to non-destructive testing,” *Composite Structures*, vol. 23, no. 3, pp. 253–262, 1993.
- [297] E. Flynn, A. Haugh, and S. Lopez, “Small defect detection through local analysis of acoustic spatial wavenumber,” *Structural Health Monitoring 2015*, 2015.
- [298] S. H. Kang, J. Y. Jeon, D. H. Kim, G. Park, T. Kang, and S. W. Han, “Damage detection on thin-walled structures utilizing laser scanning and standing waves,” *Transactions of the Korean Society of Mechanical Engineers A*, vol. 41, no. 5, pp. 401–407, 2017.
- [299] T. KANG, S. I. MOON, J. H. LEE, S. W. HAN, J. H. PARK, G. PARK, and J. Y. JEON, “Measurement of thickness of wall-thinned plate using acoustic wavenumber spectroscopy and spatial local wavenumber filtering,” *Structural Health Monitoring 2017*, no. shm, 2017.
- [300] T. Kang, S. Moon, S. Han, J. Y. Jeon, and G. Park, “Measurement of shallow defects in metal plates using inter-digital transducer-based laser-scanning vibrometer,” *NDT & E International*, vol. 102, pp. 26–34, 2019.
- [301] S. Moon, T. Kang, S.-W. Han, J.-Y. Jeon, and G. Park, “Optimization of excitation frequency and guided wave mode in acoustic wavenumber spectroscopy for shallow wall-thinning defect detection,” *Journal of Mechanical Science and Technology*, vol. 32, no. 11, pp. 5213–5221, 2018.
- [302] J. Y. Jeon, S. Gang, G. Park, E. Flynn, T. Kang, and S. Woo Han, “Damage detection on composite structures with standing wave excitation and wavenumber analysis,” *Advanced Composite Materials*, vol. 26, no. sup1, pp. 53–65, 2017.

- [303] G. Fan, H. Zhang, H. Zhang, W. Zhu, and X. Chai, “Lamb wave local wavenumber approach for characterizing flat bottom defects in an isotropic thin plate,” *Applied Sciences*, vol. 8, no. 9, p. 1600, 2018.
- [304] J. S. Hall, P. McKeon, L. Satyanarayan, J. E. Michaels, N. F. Declercq, and Y. H. Berthelot, “Minimum variance guided wave imaging in a quasi-isotropic composite plate,” *Smart Materials and Structures*, vol. 20, no. 2, p. 025013, 2011.
- [305] J. L. Rose, *Ultrasonic guided waves in solid media*. Cambridge University Press, 2014.
- [306] P. Fromme and C. Rouge, “Directivity of guided ultrasonic wave scattering at notches and cracks,” in *Journal of Physics: Conference Series*, vol. 269, no. 1. IOP Publishing, 2011, p. 012018.
- [307] J. McKeon and M. Hinders, “Lamb wave scattering from a through hole,” *Journal of Sound and Vibration*, vol. 224, no. 5, pp. 843–862, 1999.
- [308] W. Karunasena, A. Shah, and S. Datta, “Plane-strain-wave scattering by cracks in laminated composite plates,” *Journal of Engineering Mechanics*, vol. 117, no. 8, pp. 1738–1754, 1991.
- [309] M. Karim and T. Kundu, “Transient surface response of layered isotropic and anisotropic half-spaces with interface cracks: Sh case,” *International journal of fracture*, vol. 37, no. 4, pp. 245–262, 1988.
- [310] X. Chen, J. E. Michaels, and T. E. Michaels, “A methodology for estimating guided wave scattering patterns from sparse transducer array measurements,” *IEEE transactions on ultrasonics, ferroelectrics, and frequency control*, vol. 62, no. 1, pp. 208–219, 2015.
- [311] R. Bratton, S. Datta, and A. Shah, “Scattering of Lamb waves in a composite plate,” *NDT and E International*, vol. 4, no. 29, p. 250, 1996.

- [312] N. Toyama, J. Noda, and T. Okabe, “Quantitative damage detection in cross-ply laminates using Lamb wave method,” *Composites science and technology*, vol. 63, no. 10, pp. 1473–1479, 2003.
- [313] N. Toyama and J. Takatsubo, “Lamb wave method for quick inspection of impact-induced delamination in composite laminates,” *Composites science and technology*, vol. 64, no. 9, pp. 1293–1300, 2004.
- [314] P. Guy, Y. Jayet, and L. Goujon, “Guided-wave interaction with complex delaminations: application to damage detection in composite structures,” in *Smart Nondestructive Evaluation and Health Monitoring of Structural and Biological Systems II*, vol. 5047. International Society for Optics and Photonics, 2003, pp. 25–34.
- [315] C. Wang and L. Rose, “Wave reflection and transmission in beams containing delamination and inhomogeneity,” *Journal of Sound and Vibration*, vol. 264, no. 4, pp. 851–872, 2003.
- [316] S. Ishak, G. Liu, S. Lim, and H. Shang, “Characterization of delamination in beams using flexural wave scattering analysis,” *Journal of vibration and acoustics*, vol. 123, no. 4, pp. 421–427, 2001.
- [317] K.-T. Kang, H.-J. Chun, J.-H. Son, J.-A. Lee, J.-H. Byun, M.-K. Um, S.-K. Lee, and J.-W. Jang, “Quantitative accessibility of delamination in composite using Lamb wave by experiments and fea,” *Advanced Composite Materials*, vol. 20, no. 4, pp. 361–373, 2011.
- [318] B. I. Murat, P. Khalili, and P. Fromme, “Scattering of guided waves at delaminations in composite plates,” *The Journal of the Acoustical Society of America*, vol. 139, no. 6, pp. 3044–3052, 2016.
- [319] P. Kudela, T. Wandowski, P. Malinowski, and W. Ostachowicz, “Application of scanning laser doppler vibrometry for delamination detection in composite structures,” *Optics and Lasers in Engineering*, vol. 99, pp. 46–57, 2017.

- [320] L. Pieczonka, L. Ambroziński, W. J. Staszewski, D. Barnoncel, and P. Pérès, “Damage detection in composite panels based on mode-converted Lamb waves sensed using 3d laser scanning vibrometer,” *Optics and Lasers in Engineering*, vol. 99, pp. 80–87, 2017.
- [321] M. Radziński, L. Doliński, M. Krawczuk, and M. Palacz, “Damage localisation in a stiffened plate structure using a propagating wave,” *Mechanical Systems and Signal Processing*, vol. 39, no. 1-2, pp. 388–395, 2013.
- [322] C. Lee and S. Park, “Flaw imaging technique for plate-like structures using scanning laser source actuation,” *Shock and Vibration*, vol. 2014, 2014.
- [323] T. J. Saravanan, N. Gopalakrishnan, and N. P. Rao, “Damage detection in structural element through propagating waves using radially weighted and factored rms,” *Measurement*, vol. 73, pp. 520–538, 2015.
- [324] R. Marks, A. Clarke, C. Featherston, C. Paget, and R. Pullin, “Lamb wave interaction with adhesively bonded stiffeners and disbonds using 3d vibrometry,” *Applied Sciences*, vol. 6, no. 1, p. 12, 2016.
- [325] C. Lee, A. Zhang, B. Yu, and S. Park, “Comparison study between rms and edge detection image processing algorithms for a pulsed laser uwpi (ultrasonic wave propagation imaging)-based ndt technique,” *Sensors*, vol. 17, no. 6, p. 1224, 2017.
- [326] M. Ruzzene, S. Jeong, T. Michaels, J. Michaels, and B. Mi, “Simulation and measurement of ultrasonic waves in elastic plates using laser vibrometry,” in *AIP Conference Proceedings*, vol. 760, no. 1. AIP, 2005, pp. 172–179.
- [327] A. Żak, M. Radziński, M. Krawczuk, and W. Ostachowicz, “Damage detection strategies based on propagation of guided elastic waves,” *Smart Materials and Structures*, vol. 21, no. 3, p. 035024, 2012.
- [328] G. K. Geetha, D. R. Mahapatra, S. Gopalakrishnan, and S. Hanagud, “Laser doppler imaging of delamination in a composite t-joint with

- remotely located ultrasonic actuators,” *Composite Structures*, vol. 147, pp. 197–210, 2016.
- [329] Z. Su and L. Ye, “Lamb wave-based quantitative identification of delamination in cf/ep composite structures using artificial neural algorithm,” *Composite Structures*, vol. 66, no. 1-4, pp. 627–637, 2004.
- [330] Y. Lu, L. Ye, Z. Su, L. Zhou, and L. Cheng, “Artificial neural network (ann)-based crack identification in aluminum plates with Lamb wave signals,” *Journal of Intelligent Material Systems and Structures*, vol. 20, no. 1, pp. 39–49, 2009.
- [331] S. A. Atashipour, H. R. Mirdamadi, M. H. Hemasian-Etefagh, R. Amirfattahi, and S. Ziaei-Rad, “An effective damage identification approach in thick steel beams based on guided ultrasonic waves for structural health monitoring applications,” *Journal of Intelligent Material Systems and Structures*, vol. 24, no. 5, pp. 584–597, 2013.
- [332] Z. Dworakowski, L. Ambrozinski, P. Packo, K. Dragan, and T. Stepinski, “Application of artificial neural networks for compounding multiple damage indices in Lamb-wave-based damage detection,” *Structural Control and Health Monitoring*, vol. 22, no. 1, pp. 50–61, 2015.
- [333] C. Sbarufatti, G. Manson, and K. Worden, “A numerically-enhanced machine learning approach to damage diagnosis using a Lamb wave sensing network,” *Journal of Sound and Vibration*, vol. 333, no. 19, pp. 4499–4525, 2014.
- [334] S. Agarwal and M. Mitra, “Lamb wave based automatic damage detection using matching pursuit and machine learning,” *Smart Materials and Structures*, vol. 23, no. 8, p. 085012, 2014.
- [335] J. M. Druce, J. D. Haupt, and S. Gonella, “Anomaly-sensitive dictionary learning for structural diagnostics from ultrasonic wavefields,” *IEEE transactions on ultrasonics, ferroelectrics, and frequency control*, vol. 62, no. 7, pp. 1384–1396, 2015.

- [336] A. De Fenza, A. Sorrentino, and P. Vitiello, “Application of artificial neural networks and probability ellipse methods for damage detection using Lamb waves,” *Composite Structures*, vol. 133, pp. 390–403, 2015.
- [337] H. Fekrmandi, M. Unal, S. R. Neva, I. N. Tansel, and D. McDaniel, “A novel approach for classification of loads on plate structures using artificial neural networks,” *Measurement*, vol. 82, pp. 37–45, 2016.
- [338] P. Nazarko and L. Ziemianski, “Damage detection in aluminum and composite elements using neural networks for Lamb waves signal processing,” *Engineering Failure Analysis*, vol. 69, pp. 97–107, 2016.
- [339] J. Melville, K. S. Alguri, C. Deemer, and J. B. Harley, “Structural damage detection using deep learning of ultrasonic guided waves,” in *AIP Conference Proceedings*, vol. 1949, no. 1. AIP Publishing, 2018, p. 230004.
- [340] H. J. Lim and H. Sohn, “Online fatigue crack quantification and prognosis using nonlinear ultrasonic modulation and artificial neural network,” in *Sensors and Smart Structures Technologies for Civil, Mechanical, and Aerospace Systems 2018*, vol. 10598. International Society for Optics and Photonics, 2018, p. 105981L.
- [341] D. Gao, Z. Wu, L. Yang, and Y. Zheng, “Guide waves-based multi-damage identification using a local probability-based diagnostic imaging method,” *Smart Materials and Structures*, vol. 25, no. 4, p. 045009, 2016.
- [342] G. Konstantinidis, B. Drinkwater, and P. Wilcox, “The temperature stability of guided wave structural health monitoring systems,” *Smart Materials and Structures*, vol. 15, no. 4, p. 967, 2006.
- [343] W. Staszewski, C. Boller, and G. R. Tomlinson, *Health monitoring of aerospace structures: smart sensor technologies and signal processing*. John Wiley & Sons, 2004.

- [344] Z. Tian, L. Yu, and C. Leckey, “Rapid guided wave delamination detection and quantification in composites using global-local sensing,” *Smart Materials and Structures*, vol. 25, no. 8, p. 085042, 2016.
- [345] J. M. Kilpatrick and V. B. Markov, “Full-field laser vibrometer for instantaneous vibration measurement and non-destructive inspection,” in *Key Engineering Materials*, vol. 437. Trans Tech Publ, 2010, pp. 407–411.
- [346] K. S. Alguri, J. E. Michaels, and J. B. Harley, “Robust baseline subtraction for ultrasonic full wavefield analysis,” in *AIP Conference Proceedings*, vol. 1806, no. 1. AIP Publishing, 2017, p. 020005.
- [347] K. S. Alguri, J. Melville, and J. B. Harley, “Baseline-free guided wave damage detection with surrogate data and dictionary learning,” *The Journal of the Acoustical Society of America*, vol. 143, no. 6, pp. 3807–3818, 2018.
- [348] E. J. Candès *et al.*, “Compressive sampling,” in *Proceedings of the international congress of mathematicians*, vol. 3, 2006, pp. 1433–1452.
- [349] D. L. Donoho, “Compressed sensing,” *IEEE Transactions on information theory*, vol. 52, no. 4, pp. 1289–1306, 2006.
- [350] E. Candes and J. Romberg, “Sparsity and incoherence in compressive sampling,” *Inverse problems*, vol. 23, no. 3, p. 969, 2007.
- [351] J. Höglund, T. Voigt, B. Wei, W. Hu, and R. Karoumi, “Compressive sensing for bridge damage detection,” *Proc. 5th Nordic Wksp. on System and Network Optimization for Wireless*, 2014.
- [352] D. Mascareñas, A. Cattaneo, J. Theiler, and C. Farrar, “Compressed sensing techniques for detecting damage in structures,” *Structural Health Monitoring*, vol. 12, no. 4, pp. 325–338, 2013.
- [353] T. Di Ianni, L. De Marchi, A. Perelli, and A. Marzani, “Compressive sensing of full wave field data for structural health monitoring



- applications,” *IEEE transactions on ultrasonics, ferroelectrics, and frequency control*, vol. 62, no. 7, pp. 1373–1383, 2015.
- [354] O. Mesnil, H. Yan, M. Ruzzene, K. Paynabar, and J. Shi, “Guided wavefield reconstruction from sparse measurements using compressed sensing,” *Structural Health Monitoring 2015*, 2015.
- [355] O. Mesnil and M. Ruzzene, “Sparse wavefield reconstruction and source detection using compressed sensing,” *Ultrasonics*, vol. 67, pp. 94–104, 2016.
- [356] M. Eybpoosh, M. Berges, and H. Y. Noh, “Sparse representation of ultrasonic guided-waves for robust damage detection in pipelines under varying environmental and operational conditions,” *Structural Control and Health Monitoring*, vol. 23, no. 2, pp. 369–391, 2016.
- [357] S. Hamidi and S. ShahbazPanahi, “Sparse signal recovery based imaging in the presence of mode conversion with application to non-destructive testing,” *IEEE Transactions on Signal Processing*, vol. 64, no. 5, pp. 1352–1364, 2016.
- [358] X. Li and W. Guo, “Simultaneous multi-mode and disperse ultrasonic guided waves signal analysing using morphological componenet analysis (mca) method,” in *2017 IEEE International Conference on Mechatronics and Automation (ICMA)*. IEEE, 2017, pp. 1279–1284.
- [359] J. B. Harley and J. M. Moura, “Sparse recovery of the multimodal and dispersive characteristics of Lamb waves,” *The Journal of the Acoustical Society of America*, vol. 133, no. 5, pp. 2732–2745, 2013.
- [360] ———, “Data-driven matched field processing for Lamb wave structural health monitoring,” *The Journal of the Acoustical Society of America*, vol. 135, no. 3, pp. 1231–1244, 2014.
- [361] J. B. Harley, “Characterizing and predicting guided wave eigenmode behavior through sparse representations,” 2015.

- [362] J. B. Harley and J. M. Moura, “Decomposition of multipath Lamb waves with sparse wavenumber analysis for structural health monitoring,” in *2013 IEEE International Ultrasonics Symposium (IUS)*. IEEE, 2013, pp. 675–678.
- [363] J. B. Harley, “Predictive guided wave models through sparse modal representations,” *Proceedings of the IEEE*, vol. 104, no. 8, pp. 1604–1619, 2015.
- [364] S. Sabeti and J. B. Harley, “Two-dimensional sparse wavenumber recovery for guided wavefields,” in *AIP Conference Proceedings*, vol. 1949, no. 1. AIP Publishing, 2018, p. 230003.
- [365] K. Xu, J.-G. Minonzio, D. Ta, B. Hu, W. Wang, and P. Laugier, “Sparse svd method for high-resolution extraction of the dispersion curves of ultrasonic guided waves,” *IEEE transactions on ultrasonics, ferroelectrics, and frequency control*, vol. 63, no. 10, pp. 1514–1524, 2016.
- [366] J. B. Harley and C. C. Chia, “Statistical partial wavefield imaging using Lamb wave signals,” *Structural Health Monitoring*, vol. 17, no. 4, pp. 919–935, 2018.
- [367] Y. Yang and S. Nagarajaiah, “Time-frequency blind source separation using independent component analysis for output-only modal identification of highly damped structures,” *Journal of Structural Engineering*, vol. 139, no. 10, pp. 1780–1793, 2012.
- [368] A. Perelli, T. Di Ianni, A. Marzani, L. De Marchi, and G. Masetti, “Model-based compressive sensing for damage localization in Lamb wave inspection,” *IEEE transactions on ultrasonics, ferroelectrics, and frequency control*, vol. 60, no. 10, pp. 2089–2097, 2013.
- [369] B. Wu, Y. Huang, X. Chen, S. Krishnaswamy, and H. Li, “Guided-wave signal processing by the sparse bayesian learning approach employing gabor pulse model,” *Structural Health Monitoring*, vol. 16, no. 3, pp. 347–362, 2017.

- [370] Y. Chang, Y. Zi, J. Zhao, Z. Yang, W. He, and H. Sun, “An adaptive sparse deconvolution method for distinguishing the overlapping echoes of ultrasonic guided waves for pipeline crack inspection,” *Measurement Science and Technology*, vol. 28, no. 3, p. 035002, 2017.
- [371] W. T. Peter and X. Wang, “Characterization of pipeline defect in guided-waves based inspection through matching pursuit with the optimized dictionary,” *NDT & E International*, vol. 54, pp. 171–182, 2013.
- [372] R. M. Levine and J. E. Michaels, “Model-based imaging of damage with Lamb waves via sparse reconstruction,” *The Journal of the Acoustical Society of America*, vol. 133, no. 3, pp. 1525–1534, 2013.
- [373] B. Park, H. Sohn, and P. Liu, “Accelerated noncontact laser ultrasonic scanning for damage detection using combined binary search and compressed sensing,” *Mechanical Systems and Signal Processing*, vol. 92, pp. 315–333, 2017.
- [374] Z. Chen, B. Jiang, J. Song, and W. Wang, “Accurate sparse recovery of rayleigh wave characteristics using fast analysis of wave speed (faws) algorithm for soft soil layers,” *Applied Sciences*, vol. 8, no. 7, p. 1204, 2018.
- [375] K. Zhou, Y. Zheng, J. Zhang, X. Xu, S. Ma, and Z. Wu, “A reconstruction-based mode separation method of Lamb wave for damage detection in plate structures,” *Smart Materials and Structures*, vol. 28, no. 3, p. 035033, 2019.
- [376] C.-b. Xu, Z.-b. Yang, Z. Zhai, B.-j. Qiao, S.-h. Tian, and X.-f. Chen, “A weighted sparse reconstruction-based ultrasonic guided wave anomaly imaging method for composite laminates,” *Composite Structures*, vol. 209, pp. 233–241, 2019.
- [377] S. Sabeti and J. B. Harley, “Polar sparse wavenumber analysis for guided wave reconstruction,” in *AIP Conference Proceedings*, vol. 2102, no. 1. AIP Publishing, 2019, p. 050012.

- [378] S. Sabeti, C. A. Leckey, L. De Marchi, and J. B. Harley, “Sparse wavenumber recovery and prediction of anisotropic guided waves in composites: A comparative study,” *IEEE transactions on ultrasonics, ferroelectrics, and frequency control*, 2019.
- [379] P.-f. Li, Y. Luo, Y. Zhou, S. Sun, T. Fei, and L. Qian, “Application of compressed sensing in damage imaging by guided wavefield in metal plate,” in *2019 Symposium on Piezoelectricity, Acoustic Waves and Device Applications (SPAWDA)*. IEEE, 2019, pp. 1–5.
- [380] J. Hua, L. Zeng, F. Gao, and J. Lin, “Dictionary design for Lamb wave sparse decomposition,” *NDT & E International*, vol. 103, pp. 98–110, 2019.
- [381] E. Monaco, A. Nasrollahi, N. D. Boffa, V. Memmolo, P. Rizzo, and F. Ricci, “Ultrasonic-gw tomographic analysis and probabilistic reconstruction approach for shm applications,” *Aerotecnica Missili & Spazio*, pp. 1–7, 2019.
- [382] H. Liebgott, R. Prost, and D. Friboulet, “Pre-beamformed RF signal reconstruction in medical ultrasound using compressive sensing,” *Ultrasonics*, vol. 53, no. 2, pp. 525–533, 2013.
- [383] M. F. Schiffner and G. Schmitz, “Fast pulse-echo ultrasound imaging employing compressive sensing,” in *2011 IEEE International Ultrasonics Symposium*. IEEE, 2011, pp. 688–691.
- [384] C. Quinsac, A. Basarab, and D. Kouamé, “Frequency domain compressive sampling for ultrasound imaging,” *Advances in Acoustics and Vibration*, vol. 2012, 2012.
- [385] N. Wagner, Y. C. Eldar, and Z. Friedman, “Compressed beamforming in ultrasound imaging,” *IEEE Transactions on Signal Processing*, vol. 60, no. 9, pp. 4643–4657, 2012.
- [386] E. J. Candès, J. Romberg, and T. Tao, “Robust uncertainty principles: Exact signal reconstruction from highly incomplete frequency infor-

- mation,” *IEEE Transactions on information theory*, vol. 52, no. 2, pp. 489–509, 2006.
- [387] G. Hennenfent and F. J. Herrmann, “Simply denoise: Wavefield reconstruction via jittered undersampling,” *Geophysics*, vol. 73, no. 3, pp. V19–V28, 2008.
- [388] J. Tropp and A. C. Gilbert, “Signal recovery from random measurements via orthogonal matching pursuit,” *IEEE Transactions on Information Theory*, vol. 53, 2005.
- [389] T. Blumensath and M. E. Davies, “Iterative thresholding for sparse approximations,” *Journal of Fourier Analysis and Applications*, vol. 14, no. 5-6, pp. 629–654, 2008.
- [390] M. Fornasier and H. Rauhut, “Iterative thresholding algorithms,” *Applied and Computational Harmonic Analysis*, vol. 25, no. 2, pp. 187–208, 2008.
- [391] I. Daubechies, M. Defrise, and C. De Mol, “An iterative thresholding algorithm for linear inverse problems with a sparsity constraint,” *Communications on pure and applied mathematics*, vol. 57, no. 11, pp. 1413–1457, 2004.
- [392] E. T. Hale, W. Yin, and Y. Zhang, “Fixed-point continuation for  $l_1$ -minimization: Methodology and convergence,” *SIAM Journal on Optimization*, vol. 19, no. 3, pp. 1107–1130, 2008.
- [393] E. J. Candès and M. B. Wakin, “An introduction to compressive sampling,” *IEEE signal processing magazine*, vol. 25, no. 2, pp. 21–30, 2008.
- [394] E. van den Berg, M. Friedlander, G. Hennenfent, F. Herrmann, R. Saab, and O. Yilmaz, “Sparco: A testing framework for sparse reconstruction,” *Tech. Rep. TR-2007-20*, 2007.
- [395] K. Fountoulakis, J. Gondzio, and P. Zhlobich, “Matrix-free interior point method for compressed sensing problems,” *Mathematical programming computation*, vol. 6, no. 1, pp. 1–31, 2014.

- [396] K. S. Alguri and J. B. Harley, “Transfer learning of ultrasonic guided waves using autoencoders: A preliminary study,” in *AIP Conference Proceedings*, vol. 2102, no. 1. AIP Publishing, 2019, p. 050013.
- [397] M. A. Figueiredo, R. D. Nowak, and S. J. Wright, “Gradient projection for sparse reconstruction: Application to compressed sensing and other inverse problems,” *IEEE Journal of selected topics in signal processing*, vol. 1, no. 4, pp. 586–597, 2007.
- [398] S. Ma, W. Yin, Y. Zhang, and A. Chakraborty, “An efficient algorithm for compressed mr imaging using total variation and wavelets,” in *Computer Vision and Pattern Recognition, 2008. CVPR 2008. IEEE Conference on*. IEEE, 2008, pp. 1–8.
- [399] A. Krizhevsky, I. Sutskever, and G. E. Hinton, “Imagenet classification with deep convolutional neural networks,” in *Advances in neural information processing systems*, 2012, pp. 1097–1105.
- [400] G. Duan, W. Hu, and J. Wang, “Research on the natural image super-resolution reconstruction algorithm based on compressive perception theory and deep learning model,” *Neurocomputing*, vol. 208, pp. 117–126, 2016.
- [401] A. Bora, A. Jalal, E. Price, and A. G. Dimakis, “Compressed sensing using generative models,” in *Proceedings of the 34th International Conference on Machine Learning-Volume 70*. JMLR. org, 2017, pp. 537–546.
- [402] C. Dong, C. C. Loy, K. He, and X. Tang, “Image super-resolution using deep convolutional networks,” *IEEE transactions on pattern analysis and machine intelligence*, vol. 38, no. 2, pp. 295–307, 2016.
- [403] J. Xie, L. Xu, and E. Chen, “Image denoising and inpainting with deep neural networks,” in *Advances in neural information processing systems*, 2012, pp. 341–349.

- [404] L. Xu, J. S. Ren, C. Liu, and J. Jia, “Deep convolutional neural network for image deconvolution,” in *Advances in Neural Information Processing Systems*, 2014, pp. 1790–1798.
- [405] W.-C. Siu and K.-W. Hung, “Review of image interpolation and super-resolution,” in *Signal & Information Processing Association Annual Summit and Conference (APSIPA ASC), 2012 Asia-Pacific*. IEEE, 2012, pp. 1–10.
- [406] B. Park and H. Sohn, “Reconstruction of laser ultrasonic wavefield images from reduced sparse measurements using compressed sensing aided super-resolution,” in *AIP Conference Proceedings*, vol. 1806, no. 1. AIP Publishing, 2017, p. 030003.
- [407] J. Schmidhuber, “Deep learning in neural networks: An overview,” *Neural networks*, vol. 61, pp. 85–117, 2015.
- [408] S. C. Park, M. K. Park, and M. G. Kang, “Super-resolution image reconstruction: a technical overview,” *IEEE signal processing magazine*, vol. 20, no. 3, pp. 21–36, 2003.
- [409] D. Glasner, S. Bagon, and M. Irani, “Super-resolution from a single image,” in *Computer Vision, 2009 IEEE 12th International Conference on*. IEEE, 2009, pp. 349–356.
- [410] X. Li, Y. Hu, X. Gao, D. Tao, and B. Ning, “A multi-frame image super-resolution method,” *Signal Processing*, vol. 90, no. 2, pp. 405–414, 2010.
- [411] R. Keys, “Cubic convolution interpolation for digital image processing,” *IEEE transactions on acoustics, speech, and signal processing*, vol. 29, no. 6, pp. 1153–1160, 1981.
- [412] W. T. Freeman, T. R. Jones, and E. C. Pasztor, “Example-based super-resolution,” *IEEE Computer graphics and Applications*, vol. 22, no. 2, pp. 56–65, 2002.

- [413] H. Chang, D.-Y. Yeung, and Y. Xiong, "Super-resolution through neighbor embedding," in *Computer Vision and Pattern Recognition, 2004. CVPR 2004. Proceedings of the 2004 IEEE Computer Society Conference on*, vol. 1. IEEE, 2004, pp. I-I.
- [414] M. Aharon, M. Elad, A. Bruckstein *et al.*, "K-svd: An algorithm for designing overcomplete dictionaries for sparse representation," *IEEE Transactions on signal processing*, vol. 54, no. 11, p. 4311, 2006.
- [415] Y. LeCun, Y. Bengio, and G. Hinton, "Deep learning," *nature*, vol. 521, no. 7553, p. 436, 2015.
- [416] G. Hinton, L. Deng, D. Yu, G. E. Dahl, A.-r. Mohamed, N. Jaitly, A. Senior, V. Vanhoucke, P. Nguyen, T. N. Sainath *et al.*, "Deep neural networks for acoustic modeling in speech recognition: The shared views of four research groups," *IEEE Signal processing magazine*, vol. 29, no. 6, pp. 82-97, 2012.
- [417] J. Kim, J. Kwon Lee, and K. Mu Lee, "Accurate image super-resolution using very deep convolutional networks," in *Proceedings of the IEEE conference on computer vision and pattern recognition*, 2016, pp. 1646-1654.
- [418] K. He, X. Zhang, S. Ren, and J. Sun, "Deep residual learning for image recognition," in *Proceedings of the IEEE conference on computer vision and pattern recognition*, 2016, pp. 770-778.
- [419] K. Simonyan and A. Zisserman, "Very deep convolutional networks for large-scale image recognition," *arXiv preprint arXiv:1409.1556*, 2014.
- [420] Y. Bengio, P. Simard, P. Frasconi *et al.*, "Learning long-term dependencies with gradient descent is difficult," *IEEE transactions on neural networks*, vol. 5, no. 2, pp. 157-166, 1994.
- [421] Y. Jia, E. Shelhamer, J. Donahue, S. Karayev, J. Long, R. Girshick, S. Guadarrama, and T. Darrell, "Caffe: Convolutional architecture for



- fast feature embedding,” in *Proceedings of the 22nd ACM international conference on Multimedia*. ACM, 2014, pp. 675–678.
- [422] C. Dong, C. C. Loy, and X. Tang, “Accelerating the super-resolution convolutional neural network,” in *European Conference on Computer Vision*. Springer, 2016, pp. 391–407.
- [423] J. Yang, J. Wright, T. S. Huang, and Y. Ma, “Image super-resolution via sparse representation,” *IEEE transactions on image processing*, vol. 19, no. 11, pp. 2861–2873, 2010.
- [424] J. Deng, W. Dong, R. Socher, L.-J. Li, K. Li, and L. Fei-Fei, “Imagenet: A large-scale hierarchical image database,” in *Computer Vision and Pattern Recognition, 2009. CVPR 2009. IEEE Conference on*. Ieee, 2009, pp. 248–255.
- [425] Q. Huynh-Thu and M. Ghanbari, “Scope of validity of psnr in image/video quality assessment,” *Electronics letters*, vol. 44, no. 13, pp. 800–801, 2008.
- [426] Z. Wang, A. C. Bovik, H. R. Sheikh, and E. P. Simoncelli, “Image quality assessment: from error visibility to structural similarity,” *IEEE transactions on image processing*, vol. 13, no. 4, pp. 600–612, 2004.
- [427] Z. Wang, J. Chen, and S. C. Hoi, “Deep learning for image super-resolution: A survey,” *arXiv preprint*, pp. 1–23, 2019.
- [428] W. Yang, X. Zhang, Y. Tian, W. Wang, J.-H. Xue, and Q. Liao, “Deep learning for single image super-resolution: A brief review,” *IEEE Transactions on Multimedia*, pp. 1–16, 2019.
- [429] D. Li and Z. Wang, “Video superresolution via motion compensation and deep residual learning,” *IEEE Transactions on Computational Imaging*, vol. 3, no. 4, pp. 749–762, 2017.
- [430] C. Ledig, L. Theis, F. Huszár, J. Caballero, A. Cunningham, A. Acosta, A. Aitken, A. Tejani, J. Totz, Z. Wang *et al.*, “Photo-realistic single image super-resolution using a generative adversarial network,” in

*Proceedings of the IEEE conference on computer vision and pattern recognition*, 2017, pp. 4681–4690.

- [431] I. ISO, “12232: Photography-electronic still picture cameras: Determination of iso speed,” *International Organization for Standardization, Geneva, Switzerland*, 1997.
- [432] J. Yamanaka, S. Kuwashima, and T. Kurita, “Fast and accurate image super resolution by deep cnn with skip connection and network in network,” in *International Conference on Neural Information Processing*. Springer, 2017, pp. 217–225.